

**MODELING AND ANALYSIS OF LEAD-FREE
PEROVSKITE PHOTOCONDUCTORS FOR
DIRECT CONVERSION X-RAY IMAGING
DETECTORS**

by

Naznin Sultana

1017062247

MASTER OF SCIENCE
IN
ELECTRICAL AND ELECTRONIC ENGINEERING



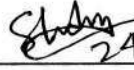
Electrical and Electronic Engineering
Bangladesh University of Engineering and Technology

Dhaka, Bangladesh

July, 2023

This thesis titled, **MODELING AND ANALYSIS OF LEAD-FREE PEROVSKITE PHOTOCONDUCTORS FOR DIRECT CONVERSION X-RAY IMAGING DETECTORS**, submitted by Naznin Sultana, Roll No.: 1017062247, Session: October 2017, has been accepted as satisfactory in partial fulfillment of the requirements for the degree of MASTER OF SCIENCE IN ELECTRICAL AND ELECTRONIC ENGINEERING on 24th July, 2023.

BOARD OF EXAMINERS


24.07.23

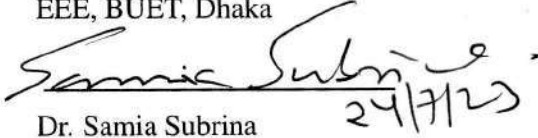
Dr. Shaikh Asif Mahmood
Associate Professor
EEE, BUET, Dhaka

Chairman
(Supervisor)



Dr. Md. Aynal Haque
Head and Professor
EEE, BUET, Dhaka

Member
(Ex-Officio)


24/7/23

Dr. Samia Subrina
Professor
EEE, BUET, Dhaka

Member


24/07/23

Dr. Mahbub Alam
Associate Professor
EEE, BUET, Dhaka

Member


24/7/23

Dr. M. Mofazzal Hossain
Professor
Department of Electrical and Electronic Engineering,
University of Liberal Arts Bangladesh, Dhaka

Member
(External)

Candidate's Declaration

This is to certify that the work presented in this thesis entitled, "MODELING AND ANALYSIS OF LEAD-FREE PEROVSKITE PHOTOCONDUCTORS FOR DIRECT CONVERSION X-RAY IMAGING DETECTORS", is the outcome of the research carried out by Naznin Sultana under the supervision of Dr. Shaikh Asif Mahmood, Associate Professor, Electrical and Electronic Engineering (EEE), Bangladesh University of Engineering and Technology (BUET), Dhaka-1205, Bangladesh.

It is also declared that neither this thesis nor any part thereof has been submitted anywhere else for the award of any degree, diploma, or other qualifications.

Signature of the Candidate

Naznin Sultana

Naznin Sultana

1017062247

Dedication

I dedicate this thesis to my parents and siblings, who supported me no matter what, even during the most difficult of times.

Contents

Certification	ii
Candidate's Declaration	iii
Dedication	iv
List of Figures	viii
List of Tables	xii
Acknowledgement	xiii
Abstract	xiv
1 Introduction	1
1.1 X-ray Imaging	1
1.2 Digital X-ray Detection	2
1.2.1 Flat-panel Detector	3
1.2.2 Indirect Conversion X-ray detector	5
1.2.3 Direct Conversion X-ray detector	6
1.2.4 Digital Readout Systems	9
1.3 Characteristics of Ideal X-ray Photoconductors	10
1.3.1 Parameters for Digital X-ray Imaging Systems	11
1.4 Motivation	12
1.5 Research Objectives	16
1.6 Thesis Outline	16
2 Background Theory of X-ray Detector	18
2.1 Attenuation of X-rays in the Material	18
2.2 Interaction Mechanisms of X-rays with Material	20
2.2.1 Photoelectric Absorption	20
2.2.2 Rayleigh Scattering	21
2.2.3 Compton Scattering	21

2.3	Ionization Energy	22
2.4	Carrier Transport Phenomena	22
2.4.1	Carrier Drift	23
2.4.2	Carrier Diffusion	24
2.5	Carrier Trapping and Recombination	25
2.6	X-ray Sensitivity of a Photoconductor	28
2.6.1	Normalized Sensitivity	29
2.7	Summary	29
3	Photoconductors in X-ray Image Detection	30
3.1	Introduction	30
3.2	Classification of Solids	31
3.2.1	Crystalline Solids	31
3.2.2	Polycrystalline Solids	31
3.2.3	Amorphous Solids	32
3.3	Amorphous Selenium (a-Se)	33
3.4	Polycrystalline HgI ₂	36
3.5	Polycrystalline PbI ₂	36
3.6	Polycrystalline CdZnTe	37
3.7	Perovskites in Radiation Detection	37
3.7.1	Organic-Inorganic 3D Perovskites	38
3.7.2	All Inorganic Lead Perovskites	39
3.8	3D Double Perovskite : Cs ₂ AgBiBr ₆	41
3.8.1	Structure and Chemical Bonds	42
3.8.2	Defects in Cs ₂ AgBiBr ₆	44
3.8.3	Linear Attenuation Coefficient	45
3.9	Summary	46
4	Photocurrent in X-ray Detector	47
4.1	Introduction	47
4.2	Analytical Model of Photocurrent	48
4.3	Dark Current	50
4.3.1	Origin of Dark Current	51
4.4	Initial Field Distribution in the Presence of Trapped Charge in the Bulk and Accumulated Ion near the Metal/Photoconductor Interface	57
4.5	Electric Field Distribution in Cs ₂ AgBiBr ₆	61
4.6	Photocurrent in Cs ₂ AgBiBr ₆	65

4.7	Summary	70
5	Modeling of Sensitivity in X-ray Detector	71
5.1	Introduction	71
5.2	Numerical Model of Sensitivity	72
5.3	Expression of Sensitivity in Normalized Coordinates	75
5.4	Summary	77
6	Results and Discussions	78
6.1	Introduction	78
6.2	Charge Carrier Distribution and Electric Field Distribution	79
6.3	Effect of Applied Electric Field on Sensitivity	82
6.4	Effect of Charge Carrier Lifetime on Sensitivity	86
6.5	Effect of Device Thickness on Sensitivity	91
6.6	Effect of X-ray Dose on Sensitivity	92
6.7	$\text{Cs}_2\text{AgBiBr}_6$ in Medical Diagnostics	95
6.8	Summary	97
7	Conclusions and Future Works	99
7.1	Conclusion	99
7.2	Suggestions for Future Works	101
A	Terms Related to Radiation Detection	102
B	X-ray Photon Fluence	104
C	Finite Difference Method	106
	References	110

List of Figures

1.1	Schematic illustration of diagnostic imaging with a flat-panel X-ray image detector.	3
1.2	Schematic illustration of a direct (left) and indirect (right) X-ray detector.	4
1.3	Cross-section of a single pixel for an indirect conversion AMFPI.	5
1.4	A simplified, schematic diagram of the cross-sectional structure of two pixels of a direct conversion X-ray image detector.	6
1.5	Simplified physical cross-section of a single pixel with a TFT switch.	7
1.6	Anrad's mammographic FPXI AXS-2430 used in the USA and European mammography markets	8
1.7	Schematic diagram that shows few pixels of active matrix array (AMA) for use in X-ray image detectors with self-scanned electronic readout.	9
1.8	Illustration of the configuration of a complete flat-panel X-ray imaging system.	10
2.1	Attenuation of incident X-rays in photoconductive material.	19
2.2	Interaction of X-rays with matter.	20
2.3	Deep and shallow traps in the bandgap of a semiconductor with defects.	26
2.4	The four basic deep trapping and emission processes for the case of an acceptor-like trap	27
3.1	Two-dimensional representation of atomic structure for (a) a crystalline solid, (b) a polycrystalline solid, and (c) an amorphous solid.	31
3.2	a) The grain structure of polycrystalline solids. (b) The grain boundaries with impurity atoms, vacancies, misplaced atoms, and broken bonds.	32
3.3	The bonding arrangement of Selenium.	34
3.4	A single crystalline $\text{Cs}_2\text{AgBiBr}_6$ double perovskite unit cell. Small black spheres represent Br^- , large magenta spheres represent Cs^+ , and light green and blue octahedrons represent $[\text{AgBr}_6]^{5-}$ and $[\text{BiBr}_6]^{3-}$, respectively.	43
3.5	Linear attenuation coefficients of $\text{Cs}_2\text{AgBiBr}_6$, MAPbI_3 and a-Se at different X-ray energies.	45

4.1	Basic structure of an X-ray image detector.	48
4.2	Electric field distribution across the photoconductor in the presence of accumulated ions near the photoconductor/metal interfaces.	52
4.3	Schottky contact between metal and p-type semiconductor.	53
4.4	Ohmic contact between metal and p-type semiconductor.	54
4.5	The energy level diagram of the $\text{Cs}_2\text{AgBiBr}_6$ single crystal and different electrodes (Au, Ag, and Al).	55
4.6	Steady-state initial distribution of trapped holes and electrons across the $\text{Cs}_2\text{AgBiBr}_6$ photoconductor and accumulation of ions near the electrode/photoconductor interfaces.	58
4.7	Steady-state initial distribution of normalized electric field across the $\text{Cs}_2\text{AgBiBr}_6$ photoconductor in the presence of different initial trapped charges.	62
4.8	Steady-state initial distribution of normalized electric field across the $\text{Cs}_2\text{AgBiBr}_6$ photoconductor in the presence of initial trapped charges for different θ	63
4.9	Steady-state initial distribution of normalized electric field across the $\text{Cs}_2\text{AgBiBr}_6$ photoconductor in the presence of accumulated ions near the metal/semiconductor interface without any initial trapped charges.	64
4.10	Steady-state initial distribution of normalized electric field across the $\text{Cs}_2\text{AgBiBr}_6$ photoconductor in the presence of accumulated ions near the metal/semiconductor interface along with initial trapped charges.	65
4.11	Photocurrent density as a function of dose rate for a pristine sample of $\text{Cs}_2\text{AgBiBr}_6$ based direct X-ray detector. Symbols and the dash-dotted line represent experimental results and photocurrent calculated from the analytical model added with the dark current, respectively. The dotted line represents the photocurrent obtained from the analytical model.	66
4.12	Photocurrent density as a function of dose rate for an annealed sample of $\text{Cs}_2\text{AgBiBr}_6$ based direct X-ray detector. Symbols and the dash-dotted line represent experimental results and photocurrent calculated from the analytical model added with the dark current, respectively. The dotted line represents the photocurrent obtained from the analytical model.	68
4.13	Dark current density as a function of dose rate for an annealed and pristine sample of $\text{Cs}_2\text{AgBiBr}_6$ based direct X-ray detector.	69
4.14	Photocurrent as a function of voltage for various dose rates for a $\text{Cs}_2\text{AgBiBr}_6$ based direct X-ray detector. The symbols and the solid line represent experimental results and theoretical model added with dark current, respectively.	70

5.1	A simplified schematic diagram of the structure of an X-ray image detector.	72
6.1	Steady-state drift charge distribution along the photoconductor thickness for different applied electric fields.	80
6.2	Steady-state trapped charge distribution along the photoconductor thickness for different applied electric fields.	81
6.3	The steady-state normalized electric field distribution across the $\text{Cs}_2\text{AgBiBr}_6$ photoconductor in the presence of accumulated ions near the metal/semiconductor interfaces along with drift and trapped charges in the bulk for different applied electric fields.	82
6.4	Sensitivity dependence on charge diffusion and recombination for different applied electric field for an annealed sample of $\text{Cs}_2\text{AgBiBr}_6$	83
6.5	Sensitivity for $\text{Cs}_2\text{AgBiBr}_6$ detector for various applied electric fields considering charge injection from the electrodes ($X=0.2\mu\text{Gy}$).	84
6.6	Sensitivity for $\text{Cs}_2\text{AgBiBr}_6$ detector for different applied electric fields considering and ignoring charge injection from the electrodes (a) Applied electric field variation 0.03 to 0.04 $\text{V}/\mu\text{m}$ with dose $5\mu\text{Gy}$ and (b) Applied electric field variation 0.08 to 0.1 $\text{V}/\mu\text{m}$ with dose $5\mu\text{Gy}$	85
6.7	Steady-state drift hole distribution in the photoconductor for different hole lifetimes.	86
6.8	Steady-state trapped hole distribution in the photoconductor for different hole lifetimes.	87
6.9	Sensitivity as a function of applied electric field for different hole lifetimes.	88
6.10	Steady-state drift electron distribution in the photoconductor for different electron lifetimes.	89
6.11	Steady-state trapped electron distribution in the photoconductor for different electron lifetimes.	89
6.12	Sensitivity as a function of applied electric field for different electron lifetimes.	90
6.13	Sensitivity as a function of device thickness for different applied electric fields.	91
6.14	Drift charge distributions along the photoconductor thickness for various doses.	92
6.15	Trapped charge distributions along the photoconductor thickness for various doses.	93

6.16	Normalized electric field distribution along the photoconductor thickness for various doses.	94
6.17	Sensitivity as a function of X-ray doses for different applied electric fields.	95
6.18	Sensitivity as a function of applied electric field for a-Se and $\text{Cs}_2\text{AgBiBr}_6$ detectors for chest radiographic applications($E=60$ keV).	96
6.19	Sensitivity as a function of applied electric field for a-Se and $\text{Cs}_2\text{AgBiBr}_6$ detectors for mammographic applications($E=20$ keV).	97
B.1	The X-ray photon fluence (photons/ mm^2) per unit X-ray exposure (Gy_{air}) versus X-ray photon energy for diagnostic X-ray imaging.	105
C.1	Discretization of time and space domain to numerically solve normalized semiconductor equations.	107

List of Tables

1.1	Parameters for digital medical X-ray imaging systems.	12
3.1	Properties of different photoconductor materials used in X-ray detection	46
3.2	Properties of different perovskite photoconductors	46
6.1	Optimized parameters for Au/Cs ₂ AgBiBr ₆ /Au X-ray detector	98

Acknowledgement

All praise goes to the Almighty and I am absolutely grateful to Allah for giving me the motivation and perseverance essential to complete my thesis successfully.

I would like to express my deep and sincere gratitude to my supervisor, Dr. Shaikh Asif Mahmood, Associate Professor, Department of Electrical and Electronic Engineering (EEE), Bangladesh University of Engineering and Technology (BUET), for providing me the opportunity to do research under his supervision and guiding me throughout the work. I am immensely grateful to him for his motivation, enthusiasm, persistence, patience, generosity, and above all, belief in my abilities which made this work possible.

I would also like to express my utmost appreciation to the members of the thesis committee Dr. Md. Aynal Haque, Dr. Samia Subrina, Dr. Mahbub Alam, and Dr. M. Mofazzal Hossain for taking the time to evaluate my work and provide insightful suggestions.

I am extremely grateful to my parents for their love, prayers, caring, and sacrifices for educating and preparing me for my future. My Special thanks go to my siblings for their support and valuable prayers.

Abstract

In a direct conversion digital X-ray image detector, incident X-rays are converted to charge and read out using a thin film transistor (TFT) array for storage and display. The digital X-ray imaging system offers better image quality, reduced X-ray exposure, and the possibility for real-time imaging compared to the traditional analog system. The choice of the photoconductor and design for optimum operation is crucial for the superior performance of the detector. In this thesis, a numerical model of X-ray sensitivity assuming a perturbed electric field due to the bulk charge trapping and ion accumulation near the photoconductor/metal interface has been developed. The continuity equations, trapping rate equations, and Poisson's equation are simultaneously solved by numerical method. The continuity equations are solved to calculate charge concentration considering the perturbed electric field. The free carrier concentration and electric field distribution are used to determine the photocurrent. The integration of the photocurrent is the collected charge. The X-ray sensitivity of a photoconductor is the collected charge per unit area per unit exposure of radiation. The developed numerical model has been applied to $\text{Cs}_2\text{AgBiBr}_6$ (CABB) based X-ray detectors. CABB possesses impressive optoelectronic properties suitable for X-ray detection with a highly stable structure and free from toxic Pb. The modeling works in this thesis identify the important factors that limit the detector performance such as the mobility-lifetime product of charge carriers, ion accumulation, and charge carrier injection from electrodes. The optimal device thickness for an Au/CABB/Au X-ray detector is estimated to be ~ 350 and $550 \mu\text{m}$ for 30 keV X-ray energy. It has been found that the optimum dose for maximum sensitivity is $\sim 4.5\text{-}7 \mu\text{Gy}$ for 30 keV X-ray energy. In chest radiology, it is discovered that CABB has higher sensitivity than a-Se by 32% for an applied electric field of $5 \text{ V}/\mu\text{m}$. In mammography, CABB has higher sensitivity than a-Se by 5.58% for an applied electric field of $5 \text{ V}/\mu\text{m}$. This investigation can ultimately lead to the reduction of patient exposure in different diagnostic medical X-ray imaging.

Chapter 1

Introduction

1.1 X-ray Imaging

X-ray imaging is one of the earliest and most widely used imaging processes. It presents useful information about an object or parts of an object by securing a comprehensive image on the film using a minimum dose of radiation. By passing radiation through the object and taking in-depth photos of the inside structures, it is a non-invasive approach of gathering information.

X-ray is a high-energy electromagnetic radiation that can infiltrate through objects, having a wavelength in the range of 10 picometers to 10 nanometers (30 exahertz to 30 petahertz) that correspond to energies in the range of 124 eV to 124 keV. Hard X-rays are X-rays with high photon energies exceeding 5~10 keV, whereas soft X-rays are those with lower photon energies [1]. Several distinct processes, including synchrotrons, channeling sources, free electron lasers, X-ray tubes, etc., can generate X-rays. The conventional X-ray tube, which emits both Bremsstrahlung and the characteristics X-rays, is the most widely used apparatus in the radiology departments worldwide [2]. In an X-ray tube, electrons are accelerated from a cathode towards a metal anode due to a high applied voltage across the tube. When the accelerated electrons striking the target metal anode interact with the coulomb field of the target atoms' nuclei, Bremsstrahlung X-rays are generated. If the striking electrons transfer a portion of their energy to release electrons from the target metal's inner shell, electrons from higher energy levels fall to fill the hole and emit characteristics X-rays. The difference in energy levels are the generated X-ray photons' energies [2].

In honor of the German scientist Wilhelm Conrad Röntgen, who made the discovery of X-rays on November 8, 1895, the term Röntgen radiation is also used for X-rays

[2]. After the discovery of X-rays, they were used in the field of medical imaging and eventually became an effective aid for medical diagnostics. The distinctive penetrating characteristics of X-rays make them perfect for imaging, not only in the field of medical diagnostics but also in non-invasive product inspection, scientific research, and security screening [3]. Soft X-ray photons with an energy range of 284 to 543 eV, sometimes referred to as the water window, can pass through water and are attenuated by carbon. They have been employed in X-ray microscopes to examine living things [4]. Hard X-ray photons with an energy of 25~50 keV are used for mammography, whereas photons with an energy of 80–130 keV are utilized for computed tomography (CT) and radiography. Hard X-rays are also useful for X-ray crystallography since their wavelengths are equivalent to the size of atoms, making them effective for analyzing crystal structures [5]. X-ray photons with energies 100 keV~1 MeV are employed to perform security inspection [6]. For tumor therapy, a medical linear accelerator with X-ray photon energies of up to hundreds MeV is utilized [7].

In an X-ray imaging system, the radiation passes through different structures of the object and gets attenuated. In conventional radiographic imaging systems, transmitted X-rays incident on a light-emitting phosphor screen. The screen emits light that exposes a photographic film placed at the back of the screen and produces a latent image of the object. This image is consequently amplified and developed by a chemical process. However, this process is time-consuming and requires high exposure to radiation [2].

1.2 Digital X-ray Detection

In recent years, there has been growing interest in developing solid-state, digital X-ray systems to improve different features of image quality such as contrast and resolution and hence allowing minimum radiation exposure. In addition, in digital radiography (DR), the process of storage and transfer of images can be easily done electronically without the loss of information [8]. Digital radiography is a superior form of X-ray detection. In DR, the attenuated X-ray which has passed through the object in question, incident on X-ray sensitive semiconductive detectors to eventually generate electronic signals. This analog signal is then amplified and converted to a digital signal using an analog-to-digital converter (A/D converter). After amplification and digitization, the signal is processed to generate a radiographic image and transferred directly to a computer. Hence, DR provides images available immediately to preview and removes the costly and toxic film processing steps. These digital images can be subjected to specific image processing techniques which improve the overall display quality of the image.

The wider dynamic range offered by digital radiography aids in reducing radiation exposure [9].

1.2.1 Flat-panel Detector

Recently significant research work has been done on flat-panel X-ray image detectors based on large-area thin-film transistors (TFT) or switching diodes and they revealed great potential in the field of digital radiography. These self-scanned digital solid-state X-ray imaging systems are superseding conventional analog X-ray imaging systems in various radiographic applications [2] [10]. Flat-panel image detectors that integrate active matrix arrays are called active matrix flat panel imagers (AMFPI). Figure 1.1 is a simplified illustration of diagnostic imaging with a flat-panel X-ray image detector.

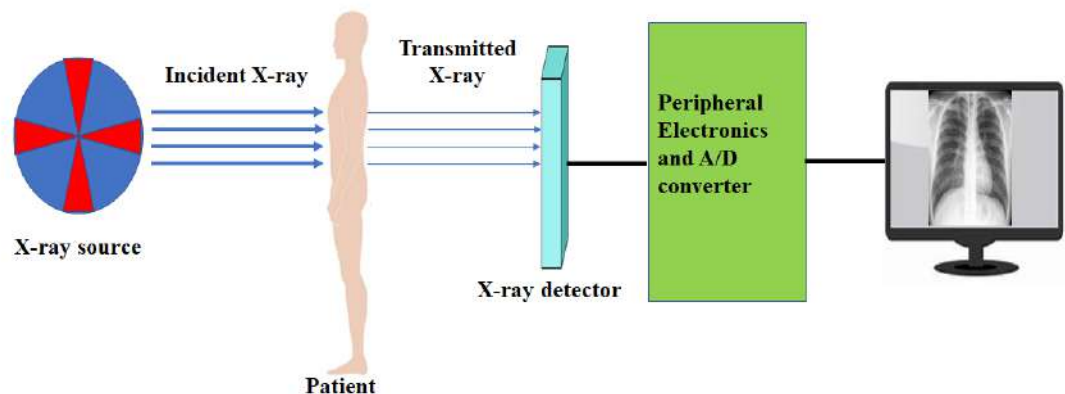


Figure 1.1: Schematic illustration of diagnostic imaging with a flat-panel X-ray image detector.

The AMFPI consists of millions of pixels, each pixel performs as an individual detector. The pixels contain detection layers (phosphor or photoconductor) deposited on the active matrix array of thin-film transistors (TFT) [11]. The detection layer converts the incident X-radiation to an amount of charge that is proportional to the radiation received by that pixel. The generated charges are read out by scanning the arrays, row by row using the peripheral electronics and multiplexing the parallel columns to a serial digital signal.

The AMFPI has a similar structure as a film/screen cassette used in analog X-ray detector systems and it can conveniently replace film/screen cassettes in existing medical X-ray systems. AMFPI systems are developed for large-area displays. These systems are compact and provide excellent image quality with negligible geometrical image distortion. The developed image from AMFPI can be stored and displayed on the computer instantly after the X-ray exposure and the stored image can be transmitted instantaneously to remote locations for consultation and analysis. Better dynamic range than analog X-ray imaging systems can be achieved by AMPFI systems [12] and they have the ability to carry out real-time imaging [13].

Digital flat-panel X-ray detectors are of two types based on their conversion process of X-ray to electric charge: direct and indirect detectors [14]. Direct detection incorporates a photoconductor to produce electrical charges directly from X-rays, whereas indirect detection incorporates a phosphor layer to produce visible photons on detection of an X-ray and then converts photons to charges [2]. The simplified detection process of direct and indirect detectors is illustrated in Figure 1.2 [15].

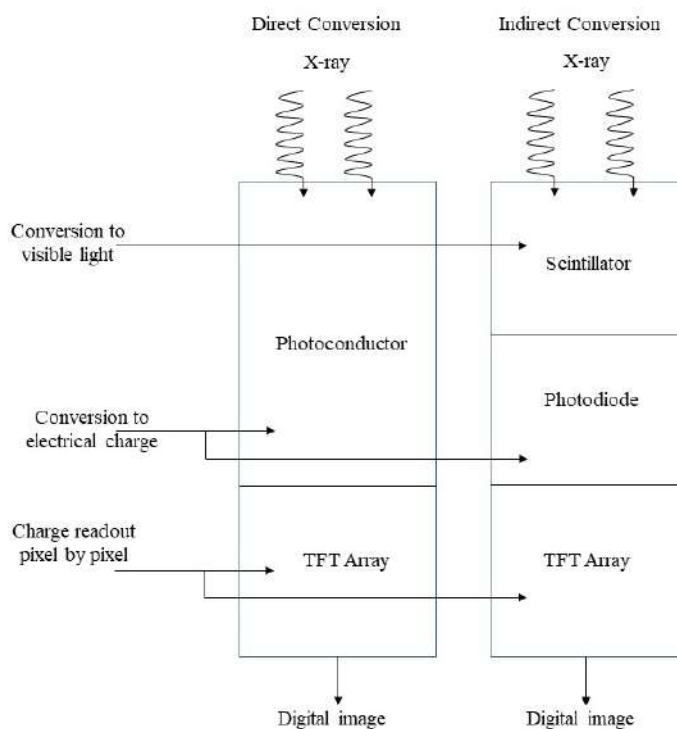


Figure 1.2: Schematic illustration of a direct (left) and indirect (right) X-ray detector.

1.2.2 Indirect Conversion X-ray detector

In indirect X-ray detection, the generation of charge from incident radiation is done in two steps. At first, a scintillating material (phosphor) is used to convert X-rays into visible light. Then the light is converted to electric charges using p-i-n photodiodes. The quantity of generated charge from a photodiode in each pixel is proportional to the light intensity incident on the photodiode. This charge is stored in the pixel capacitor and then read out with active matrix [16] [17].

Figure 1.3 depicts the physical layout of an indirect conversion X-ray image sensor. The intrinsic hydrogenated amorphous silicon (a-Si:H) layer ($\sim 1.5 \mu\text{m}$) is used as a photodiode to convert light to electric charge. Heavily doped n^+ and p^+ layers are placed on either side of the a-Si:H layer as blocking layers. The a-Si:H is doped to create the 10 to 50 nm thick n^+ layer, the p^+ layer is $\mu\text{C-Si}_{1-x}\text{C}_x\text{:H}$ having a thickness of $\sim 10 \text{ nm}$ to 20 nm . The bottom contact of the structure is chromium and the top contact is a transparent indium titanium oxide (ITO) ($\sim 50 \text{ nm}$). External voltage is applied to ITO. A surface passivation layer of oxy-nitride (a mixture of silicon oxide and silicon nitride phase; SiO_xN_y) placed on top of the ITO layer covers the photodiode structure and the TFT array. This passivation layer protects the structure from degradation [15].

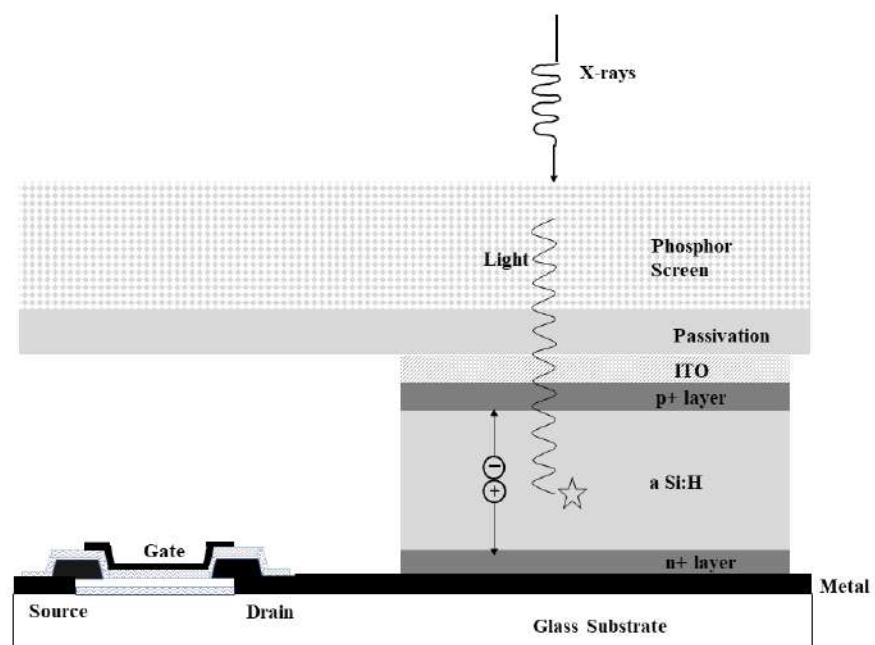


Figure 1.3: Cross-section of a single pixel for an indirect conversion AMFPI.

Despite the materials used in indirect detection may detect X-rays adequately, almost all of them require high synthesis temperatures, demand specific synthesis settings, and are

expensive. In addition, the scintillator X-ray detector's structure is typically complex and calls for more components, which restricts its use to some extent.

1.2.3 Direct Conversion X-ray detector

In direct X-ray detection, the incidence X-ray generates an electric charge directly. Photoconductive material is used for the conversion of X-radiation into charge without using any intermediate steps. The image generated from a direct conversion X-ray image detector is superior in quality than in the indirect conversion process. The manufacturing process of the direct conversion system is simple and inexpensive. The overall system is simple, compact, highly efficient with high spatial resolution, inherently digital, and offers multiple advantages [18] [19]. The light scattering by the scintillator in an indirect approach is not present here. The noise associated with optical coupling does not exist and the photoconductor can be easily deposited on the active matrix array (AMA). Thus direct conversion detector is now considered one of the key choices in digital radiography [2].

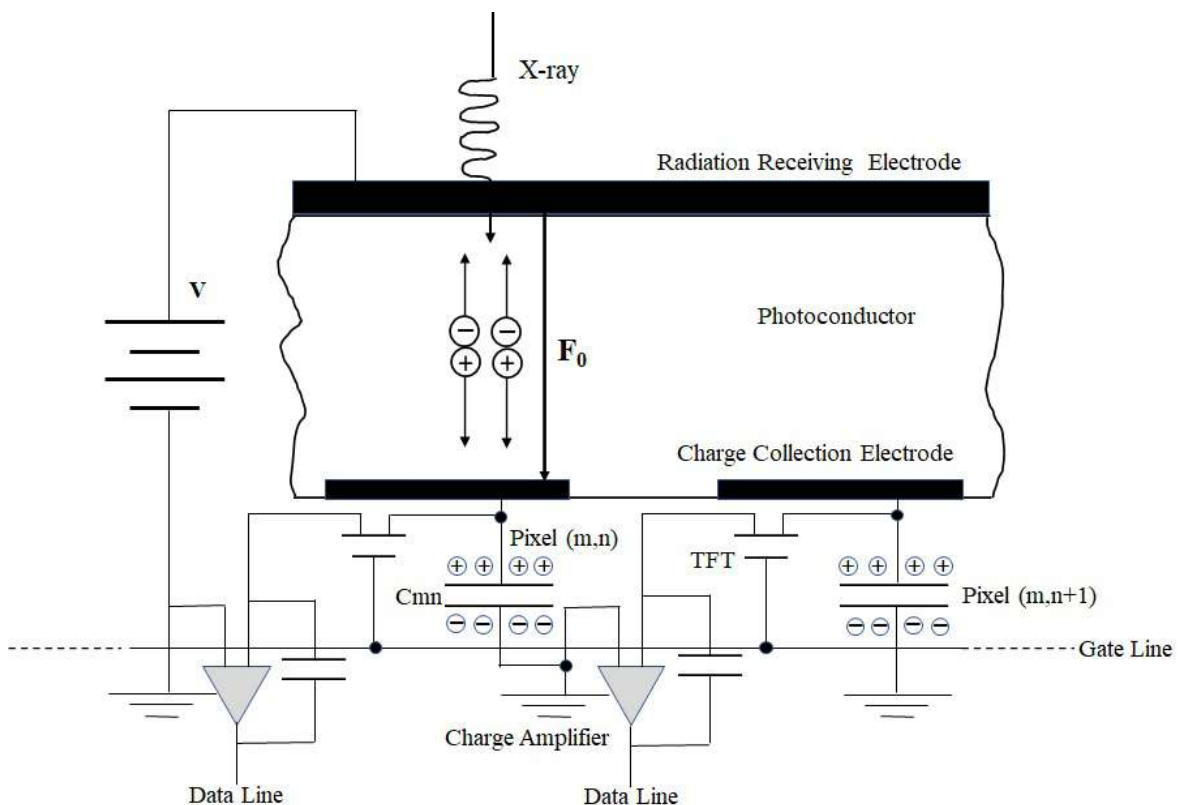


Figure 1.4: A simplified, schematic diagram of the cross-sectional structure of two pixels of a direct conversion X-ray image detector.

A simplified schematic diagram of the cross-sectional structure of a direct conversion

X-ray image detector is shown in Figure 1.4 [8]. In the illustration, two pixels of a direct flat-panel imager are shown. A photoconductive material is fabricated onto an AMA to convert X-radiation into charges. The photoconductor should have certain properties to be used commercially. The ideal properties of a photoconductor for X-ray detection are discussed in section 1.3. At present amorphous Selenium (a-Se) based detectors are commercially used for direct X-ray detection [20]. A continuous metal electrode is placed on top of the photoconductor layer. Another discrete electrode is placed at the bottom that defines each pixel. Since radiation is incident on the top electrode, it is called the radiation-receiving electrode. The bottom electrode is known as a pixel electrode or charge collection electrode. Voltage is applied on the top electrode with respect to the bottom electrode so that a uniform electric field, F_0 is established across the photoconductor. The polarity of the applied voltage depends on the electrical properties of the photoconductive material. The range of the applied bias may vary from a few hundred to several thousand volts depending on the design, characteristics, and application of the detector. The capacitance of the photoconductor layer is smaller than the capacitance of the pixel capacitor, hence the applied voltage mainly drops across the photoconductor.

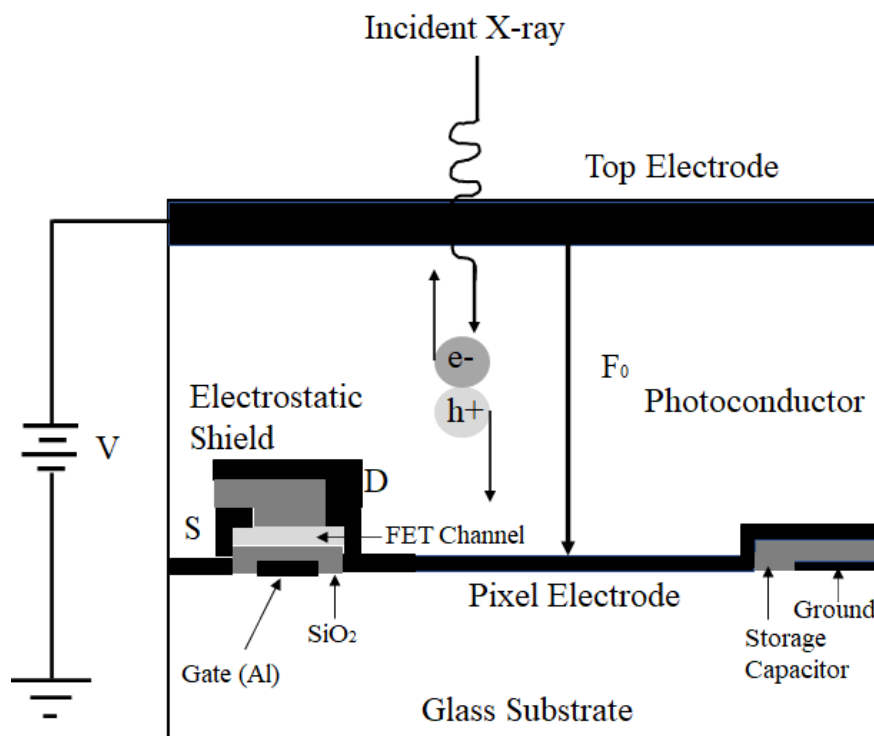


Figure 1.5: Simplified physical cross-section of a single pixel with a TFT switch.

After the incidence of X-rays, absorption of radiation in the photoconductor results in electron-hole pair (EHP) generation in the photoconductor. Charges of opposite polar-

ity move towards opposite electrodes. The generated charge carriers travel along the applied electric field lines that are perpendicular to the plane of the image. Therefore the lateral spread of the X-ray-generated response is negligible. The charges that move towards the bottom electrode would accumulate on the pixel capacitor, and the stored charges on the pixel capacitor generate an electrical signal, Q_{mn} , which is proportional to the amount of incident radiation on that pixel. The signal is read out by scanning the pixel arrays.

Each pixel has a TFT that acts as a switch in sending electrical charges to the image processor. The TFT has three electrical connections: gate, drain, and source. A simplified physical cross-section of a single pixel with a TFT switch is shown in Figure 1.5 [21]. The gate controls the switching. A scanning control unit applies pulses to the gate to turn on the TFT at regular intervals to read out the charge signal, Q_{mn} . The drain (D) terminal is connected to a pixel electrode and a pixel storage capacitor. The source (S) terminal is connected to a common data line.

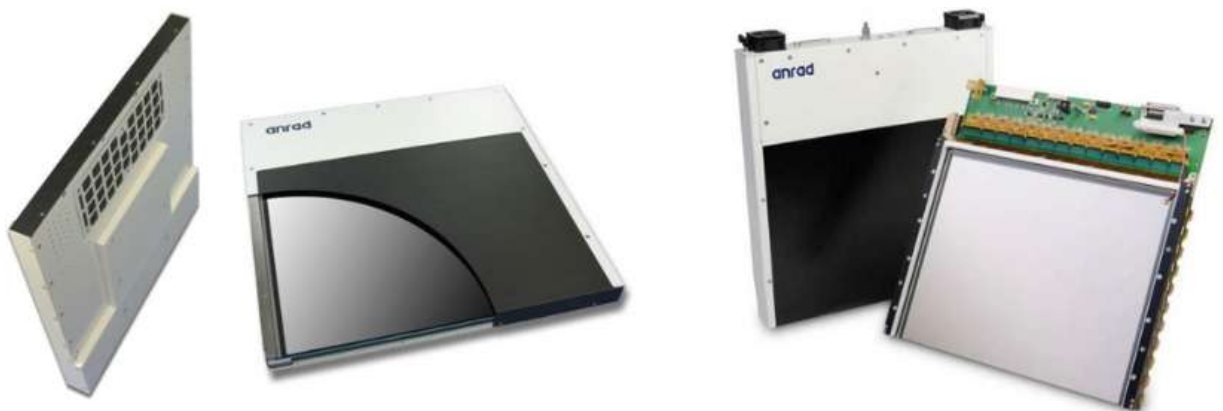


Figure 1.6: Anrad's mammographic FPXI AXS-2430 used in the USA and European mammography markets

Figure 1.6 shows a stabilized a-Se based flat panel active matrix direct conversion X-ray image sensor (AXS-2430) for mammography that has been developed and marketed by Anrad [21]. The AXS-2430 flat panel X-ray imager (FPXI) has a field of view of 24 cm x 30 cm with a pixel pitch of $85 \mu\text{m}$ and $2,816 \times 3,584$ pixels in the sensor. Because such sensors can capture and process images in a very short time, they can be used in tomosynthesis (the three-dimensional reconstruction of an object using several X-ray images taken at different angles), which is a distinct advantage. The mammographic detector in Figure 1.6 can acquire up to 3 frames per second in the breast tomosynthesis mode.

1.2.4 Digital Readout Systems

Large-area integrated circuit or AMA consists of millions of identical electronic elements and acts as the flat-panel image receptor in digital radiographic systems. Figure 1.7 shows a small group of pixels of a flat-panel AMA which has $M \times N$ (e.g. 2480×3072) pixels [22]. A single pixel has a TFT switch for signal transmission control purposes and a storage capacitor for storing the generated and later accumulated charges at the electrode. The gates of the TFTs in each row are controlled by a common signal. The sources of the TFTs in a particular column are connected to a common data line. Initially, TFT gates are controlled to turn off the switches, so that the generated charges accumulate at the capacitor of each pixel. Later, the TFTs in a row are switched on by activating gate control line m . The charges in the pixel electrode propagate to the peripheral amplifiers through data line $n=1$ to N . The signals are multiplexed, digitized, and transmitted to a computer for imaging. This is repeated to read out all the rows.

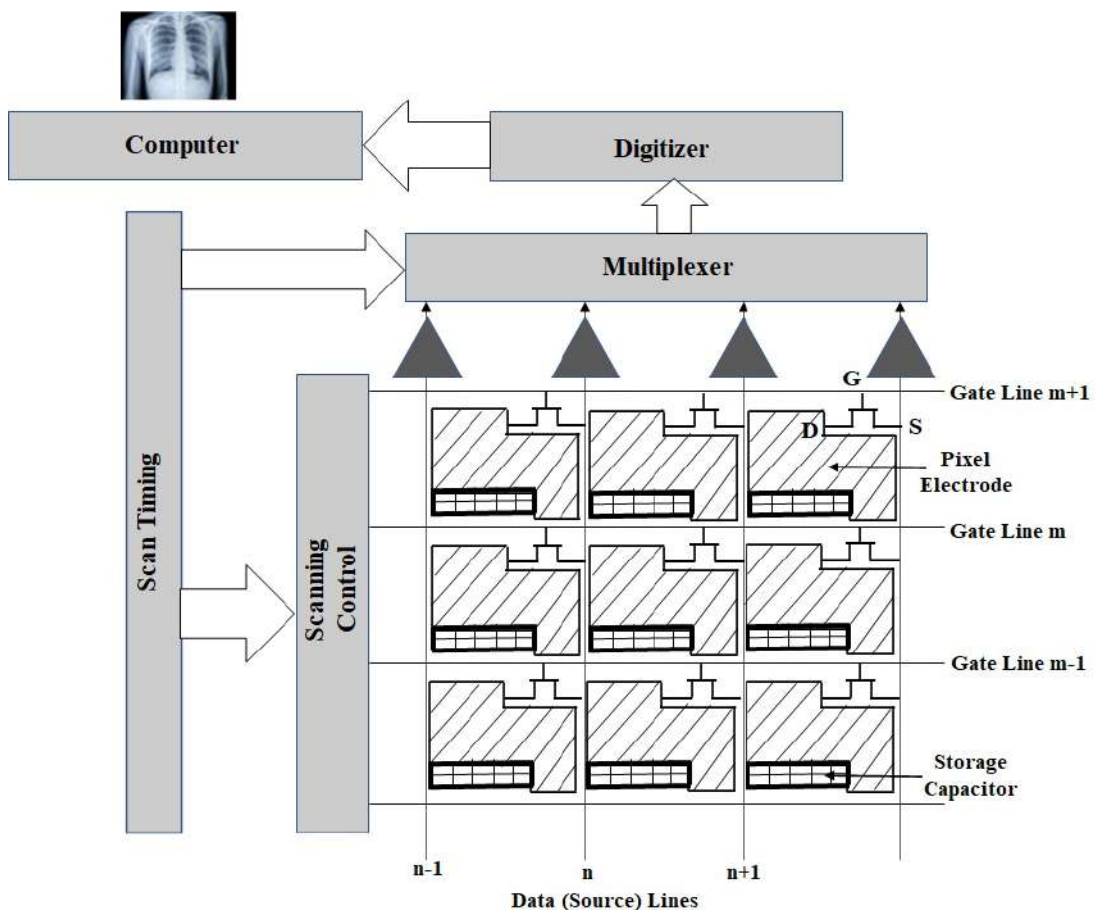


Figure 1.7: Schematic diagram that shows few pixels of active matrix array (AMA) for use in X-ray image detectors with self-scanned electronic readout.

Figure 1.8 shows the schematic diagram of a complete flat-panel X-ray imaging system

[22]. The flat-panel imaging system consists of an active matrix array, and an electronic circuit for amplification, digitization, and synchronization of the readout of the image. The image is processed, displayed, and distributed using a computer.

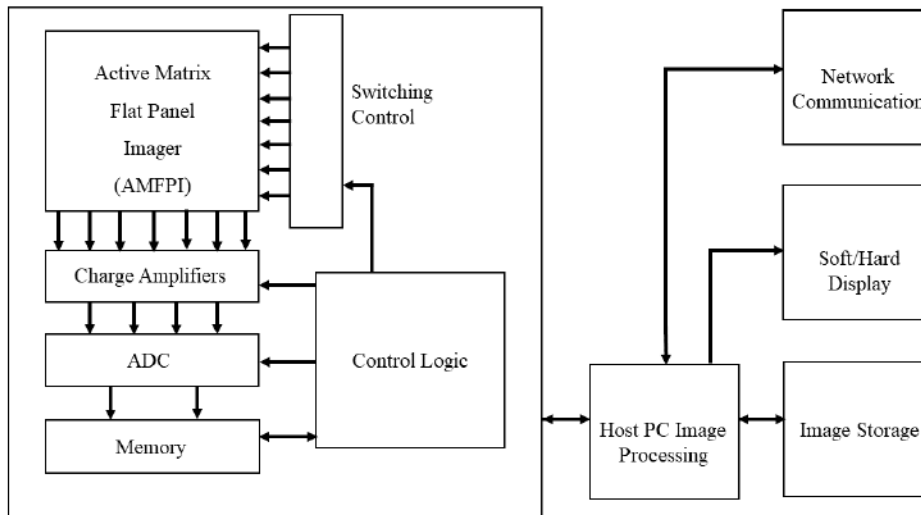


Figure 1.8: Illustration of the configuration of a complete flat-panel X-ray imaging system.

1.3 Characteristics of Ideal X-ray Photoconductors

The choice of the appropriate photoconductor in direct conversion X-ray detectors is essential to ensure the superior performance of the detecting device. Hence, when searching for photoconductors with excellent qualities, one should consider the following material properties:

- (a) In a direct conversion X-ray detector, the photoconductor needs to be fabricated on an AMA panel of the size of 30×30 cm on average. The chosen photoconductor should be such that it can be fabricated on the panel without increasing the temperature of the panel to damaging levels.
- (b) The deposited photoconductor should have uniform properties in the entire area.
- (c) The absorption thickness (δ) of the photoconductor should be such that at the energy range of X-rays in question, nearly all the incident radiation would be absorbed within a viable photoconductor thickness, L ($L > \delta$). It will decrease the probability of unwarranted exposure to radiation.

(d) The radiation energy required to generate a free electron and hole pair (W_{\pm}) is related to the energy bandgap (E_g) of the photoconductor. The lower value of W_{\pm} guarantees a higher number of generations of collectible (free) electron-hole pairs (EHPs) from a single photon. Hence, a photoconductor of high intrinsic X-ray sensitivity and low W_{\pm} is preferable.

(e) The electron-hole pairs created in the bulk of the photoconductor should not be recombined in the bulk during drifting toward the opposite electrodes. Bulk recombination is usually insignificant for clinical exposure rates.

(f) The length a carrier traverses before it gets trapped is called the schubweg ($\mu\tau'F$), where μ is the drift mobility, τ' is the deep trapping time (lifetime), F is the electric field. The deep trapping of generated EHPs in the bulk should be small. For both electrons and holes, the $\mu\tau'F$ must be greater than photoconductor thickness, L since lag and ghosting of the imaging device depend on the rate of carrier trapping.

(g) The drift of carriers in the photoconductor should be far greater than diffusion so that the captured image has a superior spatial resolution and better sensitivity.

(h) The dark current of a photoconductor consists of injected charges from electrodes and thermally generated carriers in the absence of radiation. In a commercially viable photoconductor, the dark current should be insignificant. To ensure this characteristic, the contacts to the photoconductor should be non-injecting and the rate of thermal generation of carriers from various defects or states in the energy bandgap should be exceptionally low. The wider the bandgap of the semiconductor, the lesser the dark current. The preferable range of dark current density is ~ 10 - 1000 pA/cm², for different clinical applications [22].

(i) The time required to read the image should be shorter than the slowest carrier transit time, which depends on the lowest drift mobility, applied voltage, and device thickness.

(j) The properties of the photoconductor should be unaffected by repeated exposure to X-rays.

(k) The image lag and ghosting should be insignificant.

1.3.1 Parameters for Digital X-ray Imaging Systems

To design an AMFPI, there are some specifications that are required to take into consideration depending on the type of medical diagnosis. Table 1.1 summarizes the specifications for flat panel detectors for chest radiology, mammography, and fluoroscopy [2]. kVp is referred to the peak value of the voltage applied across the X-ray generation tube

during operation. Therefore, the maximum energy of the emitted X-ray photons has the maximum energy identical to the kVp value.

Table 1.1: Parameters for digital medical X-ray imaging systems.

Medical diagnostics	Chest Radiology	Mammography	Fluoroscopy
Detector Size	35 cm x 43 cm	18 cm x 24 cm	25 cm x 25 cm
Pixel Size	200 μm x 200 μm	50 μm x 50 μm	250 μm x 250 μm
Number of pixels	1750 x 2150	3600 x 4800	1000 x 1000
Readout time	~ 1 s	~ 1 s	1/30 s
X-ray spectrum	120 kVp	30 kVp	70 kVp
Mean exposure	300 μR	12 mR	1 μR
Exposure range	30-3000 μR	0.6-240 mR	0.1-10 μR

1.4 Motivation

The X-ray sensitivity is a crucial performance parameter for an X-ray image detector to determine the superiority of the image. The X-ray sensitivity (S) of an X-ray image detector can be expressed as the charge collected per unit area per unit exposure of radiation [15]. Sensitivity depends on the material properties of the photoconductor that is responsible for absorption of radiation, and the amount of generated charges collected at the electrodes. Sensitivity is also a function of operating conditions and geometric properties of the X-ray image detector. The demand for a large dynamic range of the image detector and the necessity for low patient exposure to radiation may be ensured by the high X-ray sensitivity of the detector. Low patient exposure is required to prevent health hazards, and a large dynamic range ensures superb image quality. Hence, X-ray photoconductors with high sensitivity are preferred to design X-ray image detectors.

There are primarily three controlling factors that affect the X-ray sensitivity of a photoconductor. Firstly, what fraction of incident radiation is absorbed in the detector to generate EHPs. The linear attenuation coefficient (α) and the thickness (L) of the photoconductor determine the absorbed quantity. The attenuation coefficient of the photoconductor is dependent on the incident X-ray photon energy (E) and the material properties. Secondly, the number of EHPs generated from the interaction of X-rays with the atoms of the material. This depends on the ionization energy or the EHP creation energy (W_{\pm}) of the photoconductor and the average absorbed energy (E_{ab}) per attenuated X-ray photon of energy E . W_{\pm} is a material property, E_{ab} depends on the incident X-ray photon energy [2] and the material properties. Lastly, sensitivity varies with the percentage of

the X-ray-generated charge that is finally collected in the external circuit. This depends on the charge carrier transport properties, i.e. drift mobilities (μ) and lifetimes (τ'), the applied electric field, and the photoconductor thickness. The choice of potential X-ray image detectors depends on these controlling parameters.

Amorphous Selenium (a-Se) is the most developed photoconductor for large-area X-ray imaging for low-energy X-ray detection and is used for the commercially available large-area direct conversion flat-panel X-ray detector. Convenient and uniform deposition over a large area due to having a low melting point and high vapor pressure, moderate radiation sensitivity, superior resolution of images, low thermal noise, and low dark current at the lower electric field, make a-Se based X-ray imaging system a better choice for digital mammography [8]. However, a-Se based detectors are suitable mainly for low X-ray energy (~ 20 keV) applications [23]. Moreover, a-Se based detectors' requirement of higher ionization energy and larger applied electric field, as well as possessing low charge transport properties (i.e. $\mu\tau'$), low charge conversion efficiency, and low attenuation coefficient, limit its application. Moreover, the dark current is very high at a higher electric field [24]. This drives researchers to look into potential photoconductors for X-ray imaging with better sensitivity. For the detection of high energy X-rays and to improve the X-ray sensitivity, various potential photoconductors such as polycrystalline HgI₂ [25], polycrystalline CdZnTe [26], PbI₂ [27], PbO [28], BiI₃ [29], and organolead trihalide perovskites [30] [31] have emerged.

Poly-HgI₂ has several advantages over a-Se, including much lower intrinsic ionization energy [8], and substantially lower bias voltages (by a factor of roughly 10) than a-Se. HgI₂ based X-ray detectors show excellent sensitivity, low detection limit, good detective quantum efficiency, and spatial resolution [32]. However, the grain boundaries in poly-HgI₂ restrict the charge transport properties of the material and result in excessive dark current [32]. Polycrystalline Cadmium Zinc Telluride (CdZnTe) based detectors are appealing in high-energy X-ray detection due to their high energy resolution and good detection efficiency. The high atomic number and density of poly-CdZnTe allow for significant photon absorption and excellent detection efficiency. The manufacturing of high resistive devices with low leakage currents is made possible by the material's wide band gap and it has moderate charge transport properties [3]. However, the difficulty in large-area fabrication of CdZnTe and the presence of toxic Cd limit its benefits [33]. Poly-PbI₂ is another potential semiconductor in high-energy X-ray detection. Having constituents of high Z materials such as lead (Pb) and iodine (I), large band gap and low dark current make this material suitable for radiation detection [27]. Despite these benefits, researchers continue to look for better alternatives because of the low carrier mobility and the presence of the toxic element Pb [34].

Recently, Halide Perovskite direct detectors in the form of single crystals (SCs), polycrystalline materials, and nanocrystals (NCs) have garnered a lot of interest in the field of X-ray detection. Since the halide perovskites (HPs) are solution-processable and inexpensive, they can be cost-effectively coated on Si substrate and easily incorporate with the existing imaging technology, making them a superior choice for next-generation X-ray detectors [33]. They are high Z material, demonstrate very high effective mobility-lifetime product, tunable and direct bandgap, larger attenuation coefficient, and greater sensitivity, providing excellent options for low-dose X-ray imaging [31] [35]. Nevertheless, most HPs contain lead as a core component and the toxicity due to the presence of lead in the perovskite material, unstable structure, severe halide migration, and the requirement of high operating voltage [36] lead the researchers to investigate novel inorganic perovskite photoconductive materials for direct conversion X-ray image detectors.

Low-cost solution-processed lead-free perovskite $\text{Cs}_2\text{AgBiBr}_6$ (CABB) single crystal has been demonstrated as a potential X-ray detector in recent years. $\text{Cs}_2\text{AgBiBr}_6$ is a lead-free inorganic double perovskite photoconductor that has a stable structure, good thermal and light stability, high resistivity and suppressed ionic migration [37]. Moreover, $\text{Cs}_2\text{AgBiBr}_6$ has large average atomic number [37], which result in high probability for X-ray absorption. Additionally, it does not contain toxic Pb as some other potential perovskite materials. Not only that, $\text{Cs}_2\text{AgBiBr}_6$ has a much higher resistivity and allows comparatively low dark current. This solution-processed compound is primarily an indirect bandgap material having a wide band gap [38]. The electron-hole pair creation energy (W_{\pm}) of $\text{Cs}_2\text{AgBiBr}_6$ is much lower than a-Se [37] and sensitivity of $\text{Cs}_2\text{AgBiBr}_6$ based detector is reported to be multiple times superior to commercial a-Se based detectors [37]. The $\text{Cs}_2\text{AgBiBr}_6$ based detector's lowest detectable dose rate has been reported to be comparable to LoD of MAPbBr_3 single crystals' [37]. Although $\text{Cs}_2\text{AgBiBr}_6$ has the potential to dominate the future X-ray detection market, it also has certain inherent disadvantages such as charge carrier trapping (recombination) and ion accumulation near the metal/photoconductor interfaces. It is important to theoretically analyze the performance of $\text{Cs}_2\text{AgBiBr}_6$ based X-ray detector.

Sinchita et al. have developed a mathematical model for transient photocurrent in X-ray imaging detectors, considering charge carrier trapping under exponentially distributed carrier generation across the photoconductor [39]. This model assumed uniform electric field distribution across the photoconductor over the course of operation ignoring the space charge effect on the electric field.

S O Kasap presented a theoretical model of the X-ray sensitivity of a high-resistivity photoconductive X-ray detector operating in a constant electric field by taking into ac-

count exponential charge carrier generation and carrier trapping [40]. By combining the Hecht collection efficiency with Ramo's theorem throughout the sample thickness, the quantity of charge that has been collected in the external circuit as a result of distributed generation of electrons and holes through the detector was determined. The sensitivity model ignored recombination, the effect of bulk space charge on electric field distribution, and the diffusion of mobile carriers.

Kabir et al. established a numerical model to address the sensitivity reduction mechanisms in organic perovskite based X-ray detectors [41]. The model included the recombination between X-ray photogenerated electrons and holes as well as the recombination between trapped and mobile charges. However, the model does not consider the effects of ion accumulation in the perovskite materials.

In photoconductors, ions travel as a result of external bias application. These ions eventually accumulate near the semiconductor/metal interface and attain equilibrium. This ion migration phenomenon is especially severe in perovskite materials. Among the four types of ions in $\text{Cs}_2\text{AgBiBr}_6$: Cs, Ag, Bi, and Br, it was reported that vacancy associated with Br, V_{Br} is the most mobile defect in $\text{Cs}_2\text{AgBiBr}_6$ having the lowest diffusion barrier of ~ 0.33 eV [42]. Moreover, during the initial setup of the X-ray generator, small dosages of X-rays may penetrate the detector, creating free charges. These released charge carriers drift in the direction of the electrodes due to the bias voltage. In $\text{Cs}_2\text{AgBiBr}_6$, the holes have substantially better charge transport characteristics than the electrons [37]. Therefore, holes move more quickly and do not become trapped as easily, but electrons are more easily trapped due to their slower transit time and shorter lifetime. As a result, the distribution of the trapped holes is consistent over the thickness of the device whereas, the trapped electron distribution follows exponential decay. Charge carrier trapping in the bulk and ion accumulation near the perovskite/metal interface disturb the applied electric field in $\text{Cs}_2\text{AgBiBr}_6$ [43]. Hence, the X-ray generated free carriers travel under the influence of this non-uniform electric field, which in turn affects both the detector's sensitivity and charge collection efficiency. Furthermore, mobile electron and hole recombination can cause a significant drop in sensitivity and impair the performance of imaging detectors. We must explore the characteristics and electrical and optical properties of lead-free perovskite-based detectors in order to increase their sensitivity and X-ray image quality. Thus, we can evaluate their future prospects. No physical sensitivity model has been developed that takes into account the sensitivity to the disturbed electric field caused by ion buildup as well as charge carrier trapping including carrier recombination. Hence, it is necessary to create a theoretical model of sensitivity for $\text{Cs}_2\text{AgBiBr}_6$ detectors.

1.5 Research Objectives

The objectives of this work are:

- i. To develop a numerical model of X-ray sensitivity considering the perturbed electric field due to charge carrier trapping in the bulk and ion accumulation near the perovskite/metal interfaces.
- ii. To analyze the impact of the electric field perturbation on the X-ray sensitivity of $\text{Cs}_2\text{AgBiBr}_6$ X-ray detector.
- iii. To explore the effects of X-ray interaction and charge transport properties on the X-ray sensitivity of $\text{Cs}_2\text{AgBiBr}_6$ based detectors.
- iv. To compare the performance of $\text{Cs}_2\text{AgBiBr}_6$ based detectors with the existing a-Se based detectors in the medical diagnostics applications.

In this work, we have developed a numerical model of the sensitivity of a direct conversion X-ray image detector. $\text{Cs}_2\text{AgBiBr}_6$ photoconductor has been used as the detector. The model is based on numerical solutions of semiconductor continuity equations, Poisson's equation, and trapping rate equations in the photoconductor layer. Poisson's equation has been used to determine the initial electric field distribution along photoconductor thickness considering the presence of trapped charges in the bulk and accumulated ions near the electrodes. The presence of space charges affects the otherwise uniform distribution of the electric field across the photoconductor. The semiconductor continuity equations including carrier trapping, monomolecular and bimolecular recombination of free charges, are solved considering the perturbed electric field to calculate the free electrons and holes distributions. The charge-trapping equations are solved for both trapped electrons and holes. The analytical model of photocurrent [39] and dark current [44] have been used to determine the charge-transport properties (e.g. mobility, lifetime, capture coefficient, etc.) of $\text{Cs}_2\text{AgBiBr}_6$ detector by fitting the model result with the experimental data [37] [45]. The sensitivity of the photoconductor has been obtained using the numerical model. The continuity equations, trapping rate equations, and Poisson's equation have been expressed in normalized coordinates in order to simplify the calculation. The equations have been solved numerically using the finite difference method.

1.6 Thesis Outline

This dissertation is divided into seven chapters. Chapter 1 is an introduction to digital X-ray imaging systems. In this chapter X-rays and their generation are discussed. It

describes the direct and indirect types of digital X-ray imaging systems as well as the characteristics of an ideal photoconductor. The motivation and research objectives of our work are explained later including the outline of the thesis. In Chapter 2, a review of related theories, mechanisms, definitions, and descriptions of crucial terms related to X-ray image detectors are discussed. In Chapter 3, the optical and electrical properties of the existing (i.e. a-Se) and some prospective photoconductors for X-ray image detection are reviewed. At the conclusion of the third chapter, a comparison of these photoconductors' properties, including $\text{Cs}_2\text{AgBiBr}_6$, is provided. Chapter 4 presents the analytical model of photocurrent in an X-ray photoconductor. The origin of dark current along with the analytical model of dark current in photoconductive devices are discussed. The analytical model is applied to the $\text{Cs}_2\text{AgBiBr}_6$ detector and compared with the available experimental data. Chapter 5 discusses the numerical model of the sensitivity of an X-ray photoconductor. The numerical model is developed by solving basic semiconductor equations. The effect of space charge on the applied electric field is considered in the numerical model. The numerical solution process has been carried out using the finite difference method (FDM). In Chapter 6, the results obtained from the numerical model are discussed. The performance of $\text{Cs}_2\text{AgBiBr}_6$ photoconductor as an X-ray detector is discussed and analyzed as well. In Chapter 7, the conclusions reached from the sensitivity analysis of $\text{Cs}_2\text{AgBiBr}_6$ are presented and some recommendations for future works are provided. Some X-ray related terms are defined in Appendix A. Appendix B discusses X-ray photon fluence for various X-ray energy. The FDM is explained in detail to determine sensitivity in normalized coordinates in Appendix C. A list of the relevant references is provided at the end of the thesis.

Chapter 2

Background Theory of X-ray Detector

Basic concepts and key terms related to different methods of X-ray attenuation and absorption in the matter, electron-hole pairs (EHPs) generation, charge transport properties, carrier trapping, recombination, charge collection in the electrodes, and X-ray sensitivity of X-ray image detectors are discussed in this chapter. Intrinsic charge carriers in the bulk of X-ray photoconductors are usually insignificant. As the photoconductors have a higher bandgap, they behave as insulators in the dark without the presence of incident radiation.

2.1 Attenuation of X-rays in the Material

Incidence of X-rays on the material results in a small part of it getting reflected. Another portion of it gets transmitted. The rest gets scattered or absorbed in the material. The process by which X-rays get absorbed or scattered in the material is called X-ray attenuation. The fraction of transmitted, reflected and attenuated X-rays depend on material characteristics.

Let's assume X_I is the number of X-ray photons that are incident perpendicularly on a thin plate of thickness dx' as shown in Figure 2.1. The portion of the incident X-ray that gets scattered or absorbed in the detector is proportional to the product of the thickness of the material and the number of incident X-ray photons [46]. If α signifies the probability of interaction, then the reduction of photons (dX_I) from the incident X-ray may be expressed as,

$$dX_I = -\alpha X_I dx' \quad (2.1)$$

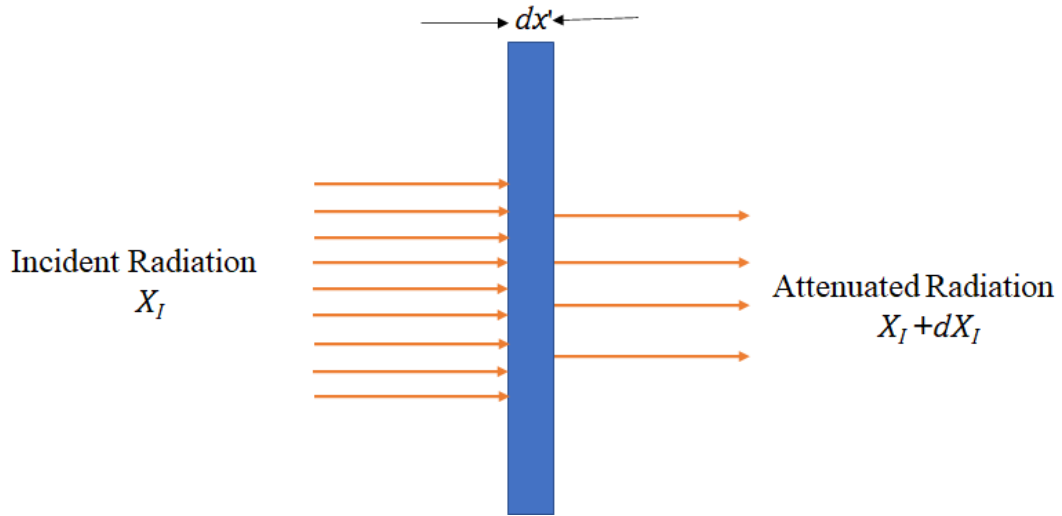


Figure 2.1: Attenuation of incident X-rays in photoconductive material.

Rearranging and integrating equation (2.1), we get,

$$\int_{X_I}^X \frac{dX_I}{X_I} = -\alpha \int_0^{x'} dx' \quad (2.2)$$

Here, X_I is the incident photons and X is the transmitted X-ray photons at a distance x' from the radiation incident surface. Hence, the transmitted X-ray photons, X , can be derived from equation (2.2),

$$X(x') = X_I e^{-\alpha x'} \quad (2.3)$$

Equation (2.3) is called the Beer-Lambert law. The linear attenuation coefficient of the medium is described as the constant α , which depends on the energy of the incident radiation (E_{ph}), atomic number (Z) of the material of interest as well as density of the material (ρ). The linear attenuation coefficient of high Z material is larger than that of low Z material.

The photon concentration per unit thickness that interacts with the material is obtained from equation (2.3).

$$X_{ph}(x') = \alpha X_I e^{-\alpha x'} \quad (2.4)$$

The quantum efficiency, η of the X-ray detector may be defined as the fraction of the X-ray photons that are attenuated in the photoconductor layer, where the layer thickness is L .

$$\eta = \frac{\int_0^L \alpha X_I e^{-\alpha x'} dx'}{X_I} \quad (2.5)$$

or,

$$\eta = 1 - e^{-\alpha L} \quad (2.6)$$

Either L or α has to be sufficiently large to make quantum efficiency near 1, which signifies complete absorption in the material. A thin detector is sufficient to fully absorb the incident radiation if the attenuation coefficient of the detector material is large enough for an X-ray of a specific energy. This is important since it will guarantee the requirement for minimal patient exposure.

2.2 Interaction Mechanisms of X-rays with Material

There are various different ways that X-rays interact with materials. Interactions with the material can cause a localized deposition of energy, and occasionally an X-ray will persist beyond the initial interaction in the form of a dispersed X-ray, distinctive X-rays, or annihilation radiation photons. Photoelectric effect, Compton scattering, and Rayleigh scattering are the three major interaction mechanisms of X-rays that get attenuated in the materials. The overall X-ray interaction processes with the atoms of the absorbing medium (e.g., photoconductor) are shown in Figure 2.2.

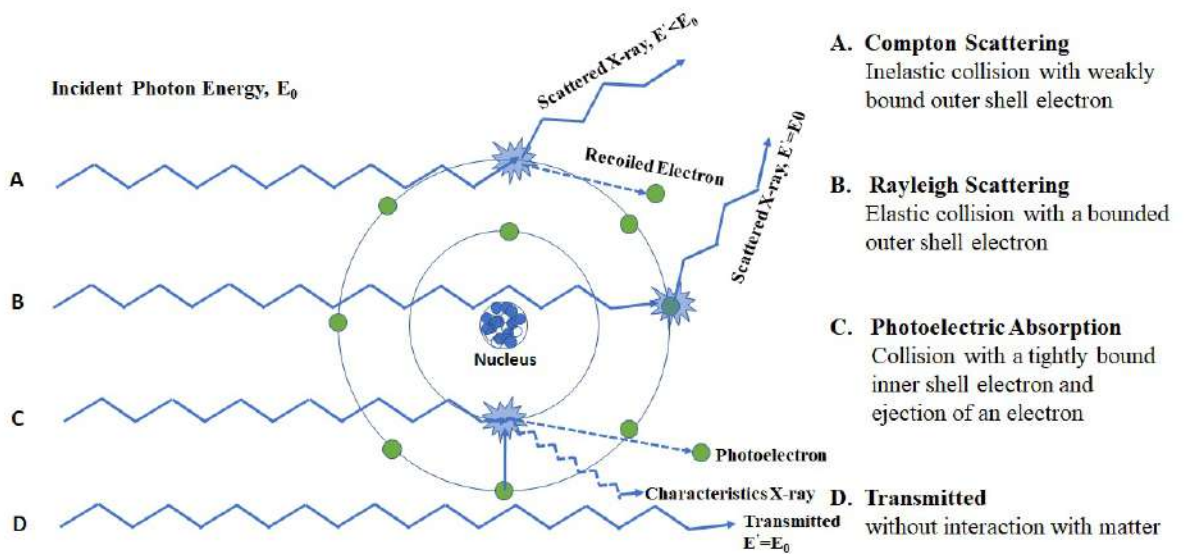


Figure 2.2: Interaction of X-rays with matter.

2.2.1 Photoelectric Absorption

In the photoelectric interaction, the incident X-ray interacts with an electron in the medium, and the energy is completely absorbed by the electron. If the binding energy of the electron with the atom (E_{BE}) is less than the energy of incidence radiation (E_0),

then the difference of the energy $E_0 - E_{BE}$ transfers to the electron as kinetic energy. The photoelectric effect results in ionization of the atom and an electron-hole pair (EHP) is generated. If the energy of the incident X-ray is less than the binding energy of the electron, photoelectric interaction with that electron will not occur. When $E_0 = E_{BE}$ photoelectric interaction is most probable and the interaction probability decreases with the increase of radiation energy. The binding energy of electrons in the innermost shell (K-shell) is greater than the electrons in the outer shell (L shell, M shell). Therefore, if the photoelectric interaction of X-ray of particular energy with K-shell electrons is not feasible, incident radiation may interact with outer shell electrons. The binding energy associated with the K shell is called the K edge and so on. When an electron is freed from an inner shell, an electron from the outer shell might transit to fill up the vacancy, which can produce characteristic X-rays. Nonradiative transitions involving Auger electrons may take place as well. These phenomena result in the complete local deposition of energy through charged particles. The characteristics X-rays are named K-fluorescent, L-fluorescent, etc. based on the electron-receiving shell.

2.2.2 Rayleigh Scattering

The mechanism of Rayleigh scattering involves the elastic scattering of X-rays by atomic electrons. In Rayleigh scattering no energy is transferred to the material and the scattered X-ray has the same energy as the incident X-ray, $E' = E_0$. Ionization in the matter does not occur, the incident X-ray only changes direction. Higher energy X-rays undergo very small angle scattering compared to lower energy X-rays since the rules of conservation of energy and momentum hold, and the recoil imparted to the atom involved in the interaction must not result in ionization. Consequently, Rayleigh scattering is more likely for low-energy X-rays and high-Z materials.

2.2.3 Compton Scattering

In the process of Compton scattering an X-ray photon interacts with an atomic electron and gets scattered. This scattering process is inelastic. The Compton scattering occurs by interaction with the electrons in the outer shell of the atom and liberates electrons. In this process, an incident photon of energy E_0 interacts with an atom and frees an electron with energy T , creating an ionized atom and becomes scattered with energy E' which is less than E_0 . Thus some energy is imparted to the medium in the Compton scattering event. The imparted energy depends on the scattering angle.

2.3 Ionization Energy

The ionization energy (W_{\pm}) of a material is defined as the amount of radiation energy required to generate a free electron-hole pair (EHP) from an atom of the medium. The amount of charge generated from the material after absorption of radiation of energy E_{ab} , is eE_{ab}/W_{\pm} . Hence, the ionization energy or EHP generation energy of the material is required to be very low to obtain better sensitivity.

Energy is absorbed after an X-ray strikes a photoconductive material, producing a free electron-hole pair. The initial highly energetic free electron then moves along the medium and further generates more EHPs along the way. The ionization energy, W_{\pm} is dependent on the bandgap energy, E_g of the semiconductor. The Klein's rule depicts the relationship between W_{\pm} and E_g for majority semiconductors which is given by [47],

$$W_{\pm} = 2.8E_g + E_{phonon} \quad (2.7)$$

Since, the phonon energy, E_{phonon} is usually small (0.1~0.5 eV) for crystalline materials, W_{\pm} is close to 2.8 times E_g . For various crystalline semiconductors, W_{\pm} is well-defined and independent of the electric field in the material due to their well-ordered structure. Nevertheless, in amorphous and polycrystalline materials the ionization energy is less than depicted by Klein's rule. For these materials, the ionization energy becomes [48],

$$W_{\pm} = 2.2E_g + E_{phonon} \quad (2.8)$$

In some cases of amorphous materials, W_{\pm} depends on the applied electric field as well as the incident X-ray photon energy. In the case of a-Se, the recombination of the generated EHPs may be responsible for the dependence of W_{\pm} on the electric field, though not conclusive. An empirical relation of W_{\pm} for a-Se has been developed by fitting the experimental results that is the electric field and the photon energy dependent. The expression for W_{\pm} at ambient temperature for an applied field, F and X-ray energy E is [49],

$$W_{\pm}(F, E) = (6 + 300/F^{0.9})(0.38 + 0.48/E^{0.5})eV \quad (2.9)$$

2.4 Carrier Transport Phenomena

Currents are produced in semiconductors by the net movement of electrons and holes. Transport describes the movement of these charged particles. Drift, which is the flow of charges caused by the applied electric field, and diffusion, which is the flow of charges

caused by the density gradient of charge carriers, are the two fundamental transport mechanisms in a semiconductor.

2.4.1 Carrier Drift

Mobile electrons and holes will experience a force when an electric field is applied to a semiconductor, causing them to travel in the direction of the electric field. This general charge movement brought on by an electric field is termed drift. Drift current results from net charge movement under the influence of an applied electric field.

If the charge density of free holes in the photoconductor is p' and v_h is the velocity of holes, the drift current density for holes can be expressed as,

$$j'_h = (ep')v_h \quad (2.10)$$

The velocity, v_h increases with time due to the applied electric field F_0 . However, in a semiconductor, charged particles collide with ionized impurity atoms and thermally vibrating lattice atoms during traveling. The velocity properties of the particles are thus changed by these collisions or scattering occurrences. The charge carriers will accelerate in the presence of the applied electric field until they get scattered and lose energy. This process will repeat until they reach electrodes. Hence, instead of an accelerated carrier, we can consider a carrier with an average drift velocity at lower applied electric fields where the average drift velocity is directly proportional to the applied electric field. The average velocity attained by hole is $v_{(avg)}$,

$$v_{(avg)} = \mu_h F_0 \quad (2.11)$$

Here, μ_h is the proportionality factor and defined as hole mobility. The carrier mobility signifies how effectively the carrier will move in the semiconductor under the influence of the applied electric field, hence it is a fundamental semiconductor property. Using the average velocity of the charge carrier from equation (2.10) in equation (2.11) we get,

$$j_{h|drift} = ep'\mu_h F_0 \quad (2.12)$$

Electron is negatively charged and the average velocity of the electron is proportional to the electric field but moves in the opposite direction of the applied electric field. For electrons with concentration n' and mobility μ_e , the drift current density for electrons becomes

$$j_{e|drift} = en'\mu_e F_0 \quad (2.13)$$

Total drift current density hence becomes,

$$j_{T|drift} = ep'\mu_h F_0 + en'\mu_e F_0 \quad (2.14)$$

2.4.2 Carrier Diffusion

In addition to drift, there is another mechanism, diffusion that can cause a current to flow through a semiconductor. Diffusion is the motion of particles in a substance along a concentration gradient from a location of higher concentration to a region of lower concentration.

Assuming a concentration gradient along the x-axis, a flux of electrons moving in the negative x-direction is created when electrons diffuse from a location of high concentration to a region of low concentration. The typical current flow is in the positive x-direction since electrons have a negative charge. When 1D charge flow is taken into account, electron diffusion current density becomes,

$$j_{e|diff} = eD_e \frac{dn'}{dx'} \quad (2.15)$$

Here, n' is free electron concentration at position x' and D_e is called the electron diffusion coefficient. The electron diffusion current density will be in the negative x-direction if the electron density gradient turns negative.

Similarly, a flux of holes moving in the negative x-direction is created when holes diffuse from a location of high concentration to a region of low concentration, provided that hole concentration increases along the positive x-direction. The resultant current flow is in the negative x-direction since holes have a positive charge. The hole diffusion current density for 1D charge movement is

$$j_{h|diff} = -eD_h \frac{dp'}{dx'} \quad (2.16)$$

Here, p' is free hole concentration at position x' and D_h is called hole diffusion coefficient. The hole diffusion current density will be in the positive x-direction if the hole density gradient turns negative. The total diffusion current density is

$$j_{T|diff} = eD_e \frac{dn'}{dx'} - eD_h \frac{dp'}{dx'} \quad (2.17)$$

The total current density due to charge drift and diffusion is

$$j'_T = ep'\mu_h F_0 + en'\mu_e F_0 + eD_e \frac{dn'}{dx'} - eD_h \frac{dp'}{dx'} \quad (2.18)$$

2.5 Carrier Trapping and Recombination

Electronic energy levels do not exist within the forbidden-energy bandgap in an ideal semiconductor. A perfect single-crystal material exhibits an ideal periodic-potential function. The perfect-periodic potential function is disturbed by crystallographic imperfections in a real semiconductor material. These imperfections will produce discrete electronic energy states within the forbidden-energy band if their density is not too high. Any defect in a semiconductor that generates localized electronic states that are energetically and spatially scattered throughout the semiconductor's band gap is known as an electronic trap. Several sources can produce electronic traps in materials. The disorder is the primary cause of traps. The static disorder is brought on by structural defects and chemical impurities. They develop during or after crystal/film formation, and their creation can be prevented by carefully managing the growth process. By being exposed to gases, electromagnetic radiation, temperature gradients, and dopants, or by interacting with other materials like a metal, or another semiconductor, extrinsic traps can be intentionally or accidentally introduced into the material.

As shown in Figure 2.3, traps can be shallow if they are close to the band edges (a few kT) or deep if they are farther (several kT) from the band edges. Shallow traps are typically thought of as localized tail states in the band gap, where acceptor-like states close to the top of the valence band (VB) and donor-like levels close to the bottom of the conduction band (CB) represent the trap states for holes and electrons, respectively. A charge carrier may be temporarily trapped and confined by a trap prior to getting released back into the band through an external signal (e.g. electric field, thermal energy, or a photon). If the trap depth is low enough ($\sim kT$), thermal detrapping of charge carriers is conceivable. Charge carriers in shallow traps at a given temperature are more likely to be thermally excited back into the band, whereas those in deep traps have a very small chance of doing so. When taking into account the transit time of a carrier over a specimen under a strong electric field, the deep trap release time is significantly prolonged, and a deeply trapped carrier is essentially permanently eliminated from conduction. The charge carrier transport properties are affected by these traps. The mobility of drift charges is dependent on shallow traps and the lifetime of carriers gets reduced by deep traps.

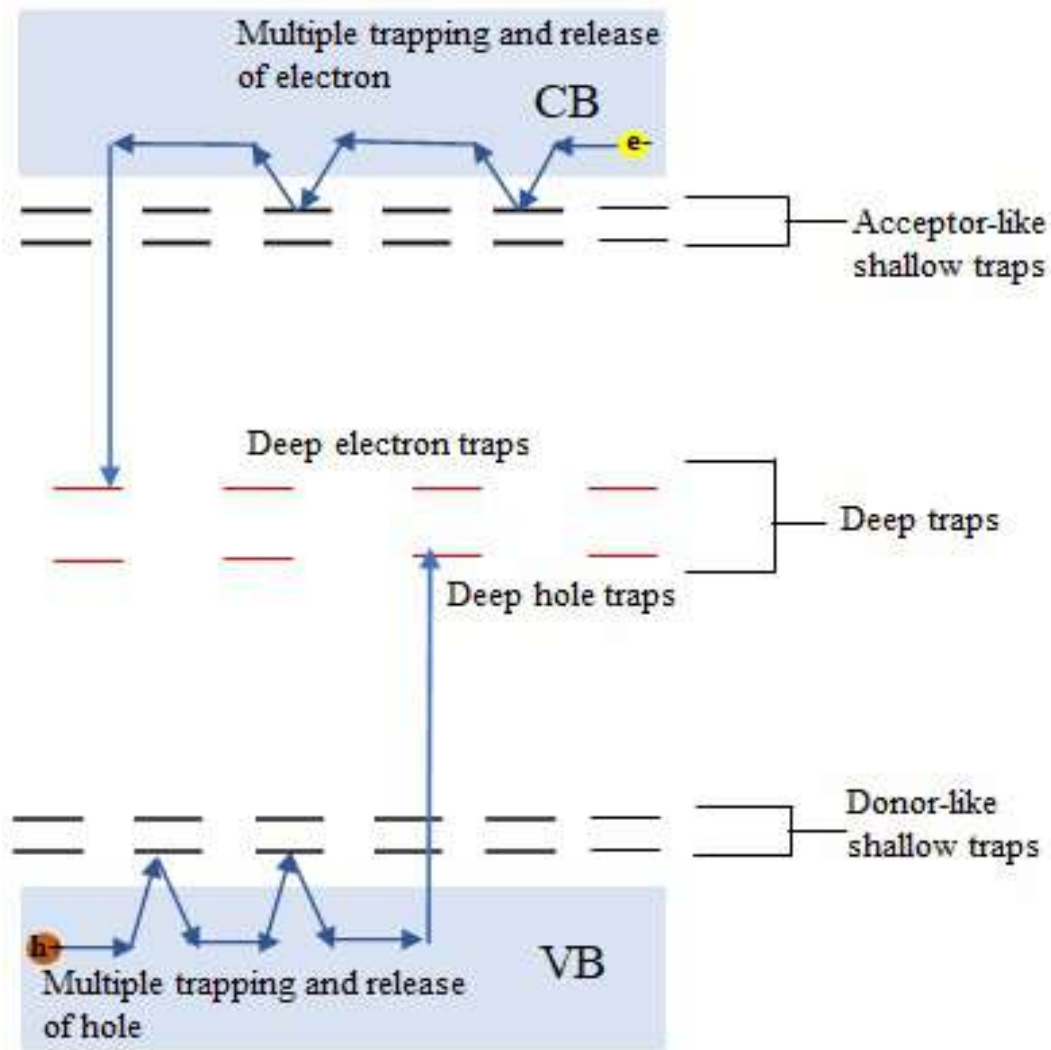


Figure 2.3: Deep and shallow traps in the bandgap of a semiconductor with defects.

The presence of shallow traps changes the actual mobility (μ_0) of the photoconductor to the effective drift mobility (μ) of carriers that is decreased by trapping and release events in the shallow traps.

$$\mu = \frac{\tau_c}{\tau_c + \tau_r} \mu_0 \quad (2.19)$$

The capture time, τ_c is the average amount of time a mobile carrier travels in the extended states prior to becoming caught in a shallow trap center. The release time, τ_r is the average amount of time a carrier spends in a trap prior to being let out into the extended states. Release from shallow traps occur due to thermal activation energy and a carrier goes through many capture and release process before reaching the electrodes.

The deep states frequently serve as charge carrier recombination sites, shortening their total lifetime. The Shockley-Read-Hall recombination theory allows for the calculation of the mean carrier lifetime in presence of traps. The Shockley-Read-Hall recomb-

nation theory determines the mean carrier lifetime in a semiconductor. The theory assumes there is only one trap or recombination center at the energy E_t that lies within the bandgap. Figure 2.4 depicts the fundamental four processes that could take place at a single trap. The trap is considered to be an acceptor-like trap, meaning that it is neutral when there is no electron present and negatively charged when there is an electron present.

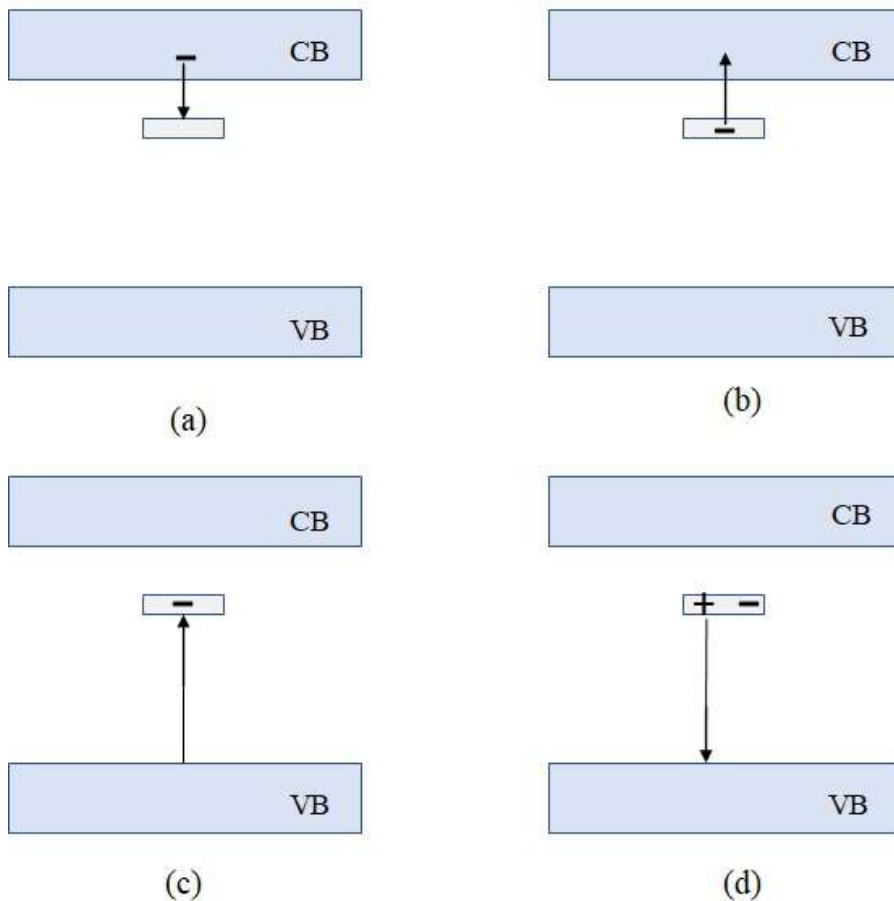


Figure 2.4: The four basic deep trapping and emission processes for the case of an acceptor-like trap

The four fundamental procedures are:

- (a) Trapping of an electron from the conduction band to an empty trap
- (b) Transfer of electron from trap to conduction band
- (c) Recombination of a hole with a trapped electron
- (d) Release of the hole from a trap to valence band

Considering the four processes and assuming low carrier injection in a weakly doped

semiconductor, the recombination rate of holes can be expressed as,

$$R = C_{th}N_{th}p' \quad (2.20)$$

Here, C_{th} = hole capture coefficient and N_{th} = total concentration of hole trapping centers. If the carrier lifetime is τ'_h and the carrier concentration of holes is p' , the recombination rate of these carriers becomes,

$$R = \frac{p'}{\tau'_h} \quad (2.21)$$

Equating equations (2.20) and (2.21), gives the hole lifetime,

$$\tau'_h = \frac{1}{C_{th}N_{th}} \quad (2.22)$$

Similarly, the electron lifetime is,

$$\tau'_e = \frac{1}{C_{te}N_{te}} \quad (2.23)$$

Here, C_{te} = electron capture coefficient and N_{te} = total concentration of electron trapping centers.

2.6 X-ray Sensitivity of a Photoconductor

The sensitivity of an X-ray image detector is defined as the collected charge per unit area per unit exposure of radiation.

$$S = \frac{Q}{AX} \quad (2.24)$$

Here, Q is the collected charge at the electrodes, A is the surface area where radiation incidence upon, and X is the radiation exposure. The unit of sensitivity is $\text{CR}^{-1}\text{cm}^{-2}$ or $\text{CGy}^{-1}\text{cm}^{-2}$. The radiation needed to produce ions with a combined charge of $2.58 \times 10^{-4}\text{C}$ per kg of air is equal to one Roentgen (R) [2]. 1 Roentgen (R) is equivalent to 1/114.025 Gray (Gy). When X-rays incident on a photoconductor, a portion of radiation gets absorbed in the medium and generates EHPs. Free holes and electrons move toward opposite electrodes as a result of the applied electric field. Before the free charges reach the electrodes for collection, they might become trapped or recombined in the bulk. The presence of space charge modifies the electric field. X-ray photocurrent is produced when the carrier moves and the integrated photocurrent is the collected

charge Q . The detector's sensitivity depends on the amount of X-rays absorbed, the ionization energy of the material, charge transport properties of the carriers, trapping and recombination of free carriers, and the presence of a perturbed electric field in the photoconductor.

2.6.1 Normalized Sensitivity

The normalized sensitivity is the ratio of the actual sensitivity to the maximum possible sensitivity assuming all of the incident X-ray photons are absorbed and the generated free charges are entirely collected by the electrodes. The photoconductor thickness, X-ray absorption profile, and charge collection efficiency all impact the normalized sensitivity. The normalized sensitivity, S is produced by multiplying the quantum efficiency (η) by the normalized collected charge Q .

The maximum collectible charge is

$$Q_0 = \frac{5.45 \times 10^{13} e \eta}{\left(\frac{\alpha_{air}}{\rho_{air}}\right) W_{\pm}} A X \left(\frac{\alpha_{en}}{\alpha}\right) \quad (2.25)$$

where e is the elemental charge and W_{\pm} is the ionization energy. α_{air} and ρ_{air} are the energy absorption coefficient and the density of air, respectively. A is the area and X is the exposure. α_{en} and α are the energy absorption coefficient and linear attenuation coefficient, respectively. The normalized collected charge, Q is

$$Q = Q'/Q_0 \quad (2.26)$$

Here, Q' is the actual collected charge. The normalized sensitivity, S is

$$S_{normalized} = Q\eta \quad (2.27)$$

2.7 Summary

The various interaction mechanisms of X-rays with materials are explained in this chapter. The photoelectric process generates EHPs, which depend on the ionization energy of the material. The free charge carriers' movement is influenced by the charge transport properties of the material. The free charges can get trapped and recombined during drifting, which affects the total collected charges and the sensitivity of the device.

Chapter 3

Photoconductors in X-ray Image Detection

3.1 Introduction

The evolution from analog to digital X-ray imaging has been largely facilitated by present flat-panel X-ray imaging detectors. They allow the transformation from conventional to digital radiography by electronically capturing an X-ray image. While indirect detectors first convert X-rays to visible light and subsequently to electrons, direct detectors convert X-rays to electrons directly. Direct detectors provide better image quality, greater dynamic range, and better resolution compared to indirect detectors. The choice of X-ray photoconductors in direct detection has a significant effect on the efficacy of a direct conversion detector. Since the photoconductive material has to be deposited uniformly with ease onto the large area AMA panel by conventional vacuum deposition techniques and the temperature of the AMA should be maintained below damaging levels (e.g., 300°C for a-Si panels), single crystal materials are not suitable as photoconductor at present, as it would require much higher temperature if they were to be grown directly onto the AMA panel. Thus amorphous or polycrystalline (poly) photoconductors are used at present for large-area flat-panel X-ray image detectors. The electrical and optical properties of the X-ray photoconductor and the design of the detector are the chief factors that affect the performance of a direct conversion X-ray detector. The chosen photoconductor should have low ionization energy, high absorption coefficient, low dark current, large bulk resistivity, low trap states, and large mobility-lifetime product, thus providing excellent sensitivity and low detection limit. For direct conversion detectors and semiconductor materials, a-Se is the most widely used. Poly-HgI₂, poly-PbI₂, poly-CdTe, and poly-CdZnTe are commercially used in

X-ray detection as well. In recent years, halide perovskites have gained popularity as a potential photoconductor in the X-ray imaging industry due to their excellent charge transport properties. This chapter discusses the characteristics of commercially available photoconductors as well as the properties of various potential detectors.

3.2 Classification of Solids

Solids are classified as crystalline and amorphous solids based on the nature of order present in the arrangement of their constituent particles. The constituent particles (i.e. atoms, ions, or molecules) in crystalline solids are arranged in a definite geometric pattern within the solids whereas for amorphous solids the constituents are not arranged in any order. Polycrystalline solids have a structure where the long-range order of crystals has been disrupted.

3.2.1 Crystalline Solids

In crystals or crystalline solids, molecules, atoms, or subatomic particles are arranged in a perfectly ordered fashion. Crystalline solids, thus, have distinct and predictable geometrical shapes. As seen in Figure 3.1 (a), the crystalline solids have a highly organized atomic arrangement.

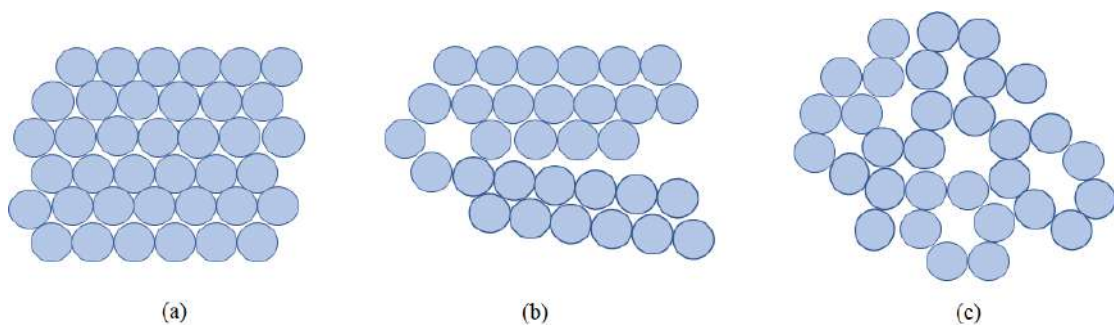


Figure 3.1: Two-dimensional representation of atomic structure for (a) a crystalline solid, (b) a polycrystalline solid, and (c) an amorphous solid.

3.2.2 Polycrystalline Solids

Crystals typically appear to have broken the long-range order in nature. Many small crystals make up polycrystalline materials. The atomic structure of a polycrystalline solid is shown in Figure 3.1 (b). Polycrystalline material contains small crystals, also

referred to as crystallites or grains [Figure 3.2 (a)]. These are positioned in various orientations and are constrained by defect boundaries. The atoms that border two crystallites are bonded together. The atoms at the boundary, however, are unable to follow their typical bonding characteristics. This boundary is called the grain boundary. There are vacancies, strained bonds, and dangling bonds at the grain boundary as a result of the uneven shapes and orientations of these grains [Figure 3.2 (b)]. A grain boundary also contains misplaced atoms that are unable to follow the crystalline pattern on either side of the boundary. Impurities frequently gather in the grain border region of polycrystalline materials. The atomic configuration near the grain boundary is assumed as disorderly.

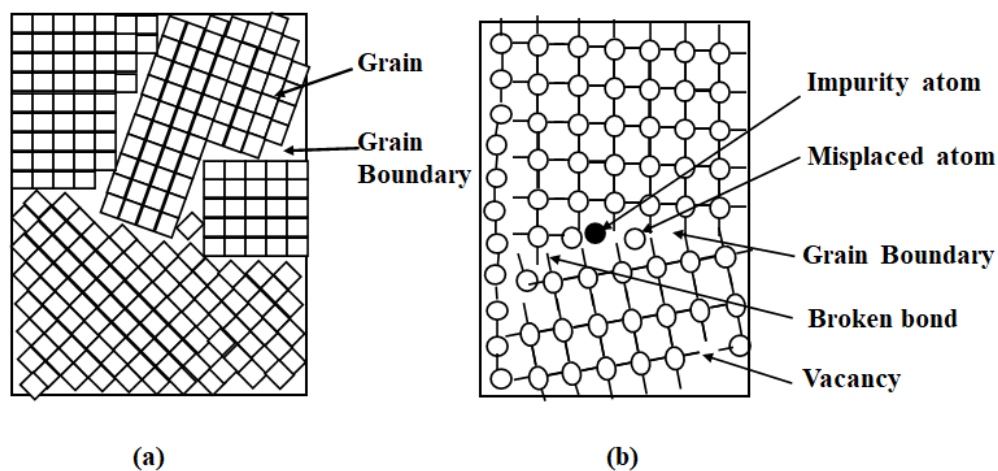


Figure 3.2: a) The grain structure of polycrystalline solids. (b) The grain boundaries with impurity atoms, vacancies, misplaced atoms, and broken bonds.

3.2.3 Amorphous Solids

The amorphous solids lack the regular crystalline structure and long-range order. They have short-range order having a few atomic or molecular dimensions. The presence of short-range order is due to the requirements of valence bonding of a particular atom in the solids. They do not possess definite bond lengths and bond numbers at the atomic level. In amorphous solids, the only certain characteristic is the connection between an atom and its nearby atoms. An amorphous semiconductor's main defect is a coordination defect, which occurs when an atom's regular structural bonding results in either an atom's over- or under-coordination. Amorphous materials don't have grain boundaries or dislocations because they lack long-range order, which has a clear advantage in several engineering applications. The isotropic qualities of amorphous solids make them appropriate for X-ray detection purposes since the X-ray photoconductor must be

coated onto the AMA panel by normal vacuum processes without raising the temperature of the AMA to destructive levels (e.g., $\sim 300^\circ\text{C}$ for a-Si panels). Figure 3.1 (c) shows the disorganized structure of an amorphous solid.

3.3 Amorphous Selenium (a-Se)

Selenium has a fascinating history as an elemental semiconductor, both in terms of its significance to physics and in terms of its uses in electronics. Because of its suitable photoconductivity, X-ray imaging fields are using Selenium in its amorphous form [24]. Since the late 1990s, a-Se based flat-panel X-ray imagers (FPXI) have been the subject of substantial research for further improvement in its applications [50] [51] [52] [53] [54]. For a variety of reasons, stabilized a-Se photoconductor materials are the industry standard in direct conversion flat-panel X-ray imagers. The pure a-Se is alloyed with around 0.2-0.5 % As and doped with 10-20 ppm Cl to produce stabilized a-Se [55]. Due to its low melting point and high vapor pressure, it can be uniformly deposited over a large area flat-panel using the conventional vacuum deposition process [56]. Because pure a-Se is thermally unstable and crystallization takes much time, stabilized a-Se is utilized in X-ray sensors instead of pure a-Se. Crystalline Se is not a good candidate for use as an X-ray photoconductor since it has high orders of magnitude of dark current and substantially lower dark resistivity than a-Se. With a highly applied electric field, a-Se shows good photoconductivity and has a superior spatial resolution. It exhibits good charge transport characteristics, a low dark current, good X-ray photoconductivity in the energy range utilized for mammography, and a reasonable X-ray absorption coefficient for low X-ray energy. As a result, amorphous Selenium (a-Se) has undergone extensive research as a photoconductor material, from its early use in xerography to its current use in FPXI [56].

In the periodic table, Selenium is a nonmetal group VI element that lies between Tellurium and Sulfur. Chalcogens are the collective term used for the elements in group VI. The chalcogens are two electrons shy of having a complete outer shell since they have six valence electrons. The density of a-Se is 4.3 g/cm^3 , relative permittivity $\epsilon_r=6.7$ and band gap $E_g=2.22 \text{ eV}$ [8]. Selenium has an atomic number(Z) of 34 and an electronic structure of $[\text{Ar}]3d^{10}4s^24p^4$. The valence band of Se is made up of lone-pair orbitals at the top, bonding states considerably deeper, whereas antibonding states make up the conduction band. Lone pairs(LP) are non-bonding states that are created when the s state of the fourth shell and one of the three p states are both filled with electron pairs. The two remaining singly occupied p states combine to form covalent bonds, which

divide into orbitals that form bonding and antibonding (B and AB) states. The bond angle is 105° , and the atomic coordination is 2. Chalcogens produce chains-like structures because of their divalent bonding. Covalent bonds are formed within the chain and Van der Waals bonds are formed between two chains. The divalent chains are cross-linked by the addition of atoms with trigonally bound bonds, such as those from Groups IV or V of the periodic table. This makes the amorphous solid stable in three dimensions. Figure 3.3 depicts the bonding arrangement of the selenium atoms.

There exist localized states (traps) in the bandgap of a-Se. The shallow traps are situated near the band edges and the deep traps exist deep in the band gap. The charge carrier transport properties are affected by these traps. Shallow traps affect the mobility of the drift charges, and deep traps shorten the lifetime of carriers. The hole drift mobility in the extended states is $\mu_{0h} \approx 0.3 \text{ cm}^2\text{V}^{-1}\text{s}^{-1}$ and the electron mobility is $\mu_{0e} \approx 0.1 \text{ cm}^2\text{V}^{-1}\text{s}^{-1}$ at room temperature [57] [58]. The effective mobility of holes in a-Se is $\mu_h \approx 0.12 \text{ cm}^2\text{V}^{-1}\text{s}^{-1}$ at room temperature and it is independent of the fabrication process. The effective mobility of electrons at room temperature is in the range $\mu_e \approx 0.003\text{-}0.006 \text{ cm}^2\text{V}^{-1}\text{s}^{-1}$ [22]. In stabilized a-Se, hole mobility remains unchanged, however, electron mobility reduction occurs with the addition of As, whereas Cl addition does not affect electron mobility.

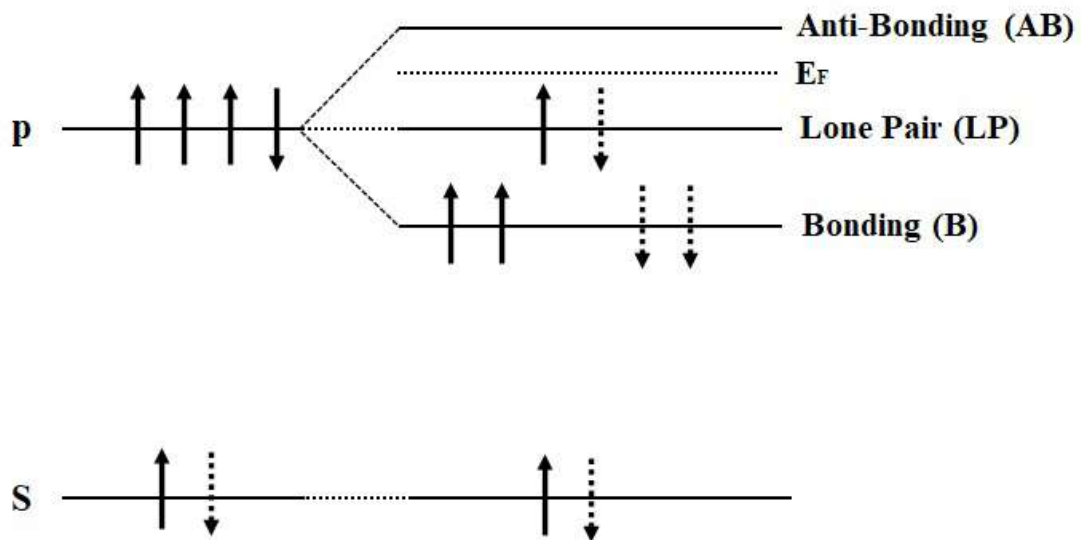


Figure 3.3: The bonding arrangement of Selenium.

Lifetimes in stabilized a-Se usually vary from 10 to 500 μs for holes and 100 to 1500 μs for electrons [22]. Deep trapping capture coefficient is $10^{-8} \text{ cm}^3\text{s}^{-1}$ [59] and integral concentration of deep trap centers is $\sim 10^{12} \text{ cm}^{-3}$ [60] [61]. The deep electron traps are located $\sim 1 \text{ eV}$ below the conduction band and deep hole traps $\sim 0.85 \text{ eV}$ above the valence band [59] [62].

Although a-Se provides several benefits when employed in X-ray detectors, it also has inherent drawbacks.

Low Charge Carrier Mobility: Low charge carrier mobility is one of the most unfavorable characteristics of a-Se. The hole drift mobility is 0.13-0.14 $\text{cm}^2\text{V}^{-1}\text{s}^{-1}$, whereas electron mobility is $5-7 \times 10^{-3} \text{cm}^2\text{V}^{-1}\text{s}^{-1}$ [63] [64]. Compared to other semiconductor materials this is much smaller, for instance, Silicon has much higher drift hole and electron mobility 480 and 1400 $\text{cm}^2\text{V}^{-1}\text{s}^{-1}$, respectively. To guarantee the full collection of generated charge at the electrodes, the drift length of both charges has to be greater than the photoconductor thickness. However, for a-Se only holes fulfill this criterion. This limitation to capture all of the X-ray-generated charges hampers the performance of the a-Se detector, particularly in breast imaging applications where a-Se is frequently utilized due to its superior spatial resolution.

Low Charge Conversion Efficiency: X-ray detectors based on a-Se have low charge conversion efficiency because the ionization energy (W_{\pm}) of a-Se is very high and dependent on the applied electric field. The EHP creation energy of a-Se is found to be 45-50 eV for an applied field of 10 $\text{V}/\mu\text{m}$, whereas, for other semiconductor materials such as Silicon, CdZnTe, poly-HgI₂, poly-PbI₂ have $W_{\pm} \approx 5$ eV at the same electric field. The ionization energy of a-Se decreases with increasing applied field. The empirical equation to establish the relationship between W_{\pm} of a-Se and the electric field for X-ray energy E is given by [49],

$$W_{\pm}(F, E) = (6 + 300/F^{0.9})(0.38 + 0.48/E^{0.5})eV \quad (3.1)$$

To lower ionization energy and therefore increase charge conversion efficiency, the a-Se detector is operated at 10 $\text{V}/\mu\text{m}$ or greater electric field. However, due to charge injections brought on by the highly applied field, dark current will certainly increase, which will result in a reduced energy resolution and a low signal-to-noise ratio. Various recombination processes can be attributed to the strong dependence of the electric field on the ionization energy of a-Se.

Dark Current: The resistivity of a-Se is $\sim 10^{14} \Omega\text{cm}$. Hence, a-Se shows a lower dark current in comparison to other potential photoconductors. However, a strong bias is required to be applied across the metal/a-Se/metal detector to achieve enough X-ray photogeneration efficiency because of the low charge transport properties of a-Se and to achieve low ionization energy [49]. The strong applied electric field in turn increases the dark current significantly due to the charge injection from the metal electrodes. The high dark current is responsible for the reduction of the dynamic range of the detector. The reported dark current in a-Se detectors is less than 1 nA/cm^2 at an applied electric

field of 20 V/ μm . With the same field dark current is found to be less than 100 pA/cm² in a p-i-n a-Se detector [65].

3.4 Polycrystalline HgI₂

One of the best alternative photoconductive materials for direct digital X-ray detectors for both static and dynamic applications in medical imaging is polycrystalline mercury iodide (HgI₂) coated on a flat panel thin film transistor (TFT) array. The high atomic number ($Z=62$) of the material makes it an excellent choice for X-ray detection [66]. HgI₂ is a highly dense material with a density of 6.3 g/cm³ and a wide bandgap of 2.1 eV [8]. The low ionization energy of HgI₂, which is 5 eV, is one of its clear advantages over a-Se. Therefore, compared to an a-Se detector, a thinner layer of HgI₂ can be used to obtain a higher X-ray sensitivity at a lower electric field. The hole and electron mobility-lifetime product of Poly-HgI₂ are $10^{-7}\sim 10^{-6}$ and $10^{-6}\sim 10^{-4}$ cm²/V, respectively [8]. Poly-HgI₂ demonstrates greater resistivity of $\sim 4\times 10^{13}$ Ωcm . Using the PVD and PIB methods, the poly-HgI₂ based detector sizes of 20 cm x 25 cm (1536 x 1920 pixels) and 9.8 cm x 9.8 cm (768 x 768 pixels), respectively, have been reported [67] [68]. The greatest drawback of the HgI₂ based detector is that it exhibits a nonuniform response from pixel to pixel because of the adverse effect of large grain size. The sensitivity variation from pixel to pixel decreases the dynamic range of the detector [67]. Moreover, the dark current of HgI₂ detectors increases super-linearly with the applied bias voltage [67]. Therefore, poly-HgI₂ based detector's performance is hindered by the presence of a large leakage current and structure's poor stability [32].

3.5 Polycrystalline PbI₂

Polycrystalline lead iodide (PbI₂) has been under research as direct conversion layers for digital X-ray imaging for a number of years. PVD polycrystalline-PbI₂ based AMFPI of 20 cm x 25 cm (1536 x 1920 pixels) has been demonstrated. The photoconductor thickness varies from 60-250 μm [67]. The range of electrons and holes in PVD PbI₂ are 7×10^{-8} cm²/V and 1.8×10^{-6} cm²/V, respectively [67]. PbI₂ has a high atomic number of 62.7 [66], a low ionization energy of ~ 5 eV, a high density of 6 g/cm³ and a high resistivity of $10^{11} \sim 10^{12}$ Ωcm [15]. PbI₂ has a wide bandgap energy of 2.3 eV [66] that helps in achieving very low thermal noise [8]. PbI₂ imagers show acceptable spatial resolution, though sensitivity is slightly lower than HgI₂. Lead iodide detectors have a very long image lag decay time which makes them unsuitable for fluoroscopic applica-

tion [67]. Additionally, the dark current of PbI_2 detectors is significantly higher than that of PVD HgI_2 detectors, making them unsuitable for applications requiring extended exposure times.

3.6 Polycrystalline CdZnTe

In commercial direct X-ray detection, polycrystalline films of CdZnTe ($< 10\%$ Zn) have been used as a photoconductor layer [69]. The thickness of the CdZnTe (CZT) layer ranges from 200 to 500 μm . $\text{Cd}_{0.95}\text{Zn}_{0.05}\text{Te}$ has a high density of 5.8 g/cm^3 and low EHP creation energy of $\sim 5 \text{ eV}$. The band gap is 1.57 eV , the relative permittivity 10.7, and resistivity $10^{11} \Omega\text{cm}$ [8]. CdZnTe has a high X-ray attenuation efficiency and a high $\mu\tau'$ product. The electron and hole mobility-lifetime products are $\sim 2 \times 10^{-4}$ and $\sim 3 \times 10^{-6} \text{ cm}^2/\text{V}$, respectively [70] [71], which increase in orders for single crystal CZT. Large and nonuniform grain sizes are believed to be responsible for temporal lag and the nonuniform response of the poly-CZT sensor. Recent studies show that Cl doping into CZT photoconductive layer makes a finer and more uniform grain structure [26]. The difficulty of large-area fabrication of CdZnTe is a challenge. Moreover, long-term exposure to toxic Cd through air, water, soil, and food leads to health hazards.

3.7 Perovskites in Radiation Detection

The exceptional optoelectronic properties of metal halide perovskites have garnered widespread interest in the fields of materials science, physics, and optoelectronics. In recent years, perovskites have demonstrated both their superior X-ray detection performance and their potential for low-dose, high-resolution imaging. They have achieved recognition as future-generation X-ray detectors due to their adjustable bandgaps, and structural dimensionality as well as their outstanding optical and electronic properties. Even though sensitive photoconduction can be seen in a variety of crystalline inorganic semiconductors when illuminated by X-rays [66], very few of these substances can be uniformly deposited onto thin-film transistor active-matrix arrays that are required for reading out the electronic signals in pixel array detectors below the temperatures that cause active-matrix degradation [22] [72]. Solution-processed perovskite materials could be used to make thick perovskite films over large regions at low cost, enabling inexpensive low-dose X-ray imaging. Halide perovskites has various benefits over conventional X-ray detection materials (i.e. a-Se) including a large effective atomic number and mobility-lifetime product, high X-ray sensitivity and high resistivity, and a low

dark current. The performance and properties of various perovskite materials in X-ray imaging are discussed in the next section.

3.7.1 Organic-Inorganic 3D Perovskites

Lead halide organic-inorganic hybrid perovskites have shown a variety of exceptional qualities, including a high carrier drift length per unit electric field (the mobility-lifetime product), low-cost solution growth of single crystals (SCs), and simple silicon electronics integration for imaging applications [37]. The general molecular formula for hybrid halide 3D perovskites is ABX_3 . A represents a small organic cation (e.g., MA^+ = Methylammonium, FA^+ = Formamidinium), B is a metal cation (e.g., Pb^{2+} , Sn^{2+}), and X is a halide anion (I^- , Br^- , Cl^-). In the perovskite structure, cation A is surrounded by eight corner-sharing octahedrons, B cations occupy the center of them, while the octahedron's points are determined by the X anions. The basic perovskite structure, ABX_3 , is cubic in shape and has $Pm - 3m$ symmetry. Nevertheless, by rotating or twisting the BX_6 octahedra and translating the A site or B site cations, it is possible to reduce this symmetry [73].

The development of X-ray detectors based on the organic-inorganic hybrid $MAPbX_3$ (MA=Methylammonium, X=Br or I) perovskite material with excellent detection sensitivity [45], increased the demand for perovskite materials for radiation detection in different applications. All the reported X-ray detectors based on perovskite materials have higher sensitivities than those currently available amorphous Selenium (a-Se) X-ray detectors [45]. In comparison to CdTe and (Cd, Zn)Te radiation sensor materials, hybrid methylammonium lead halide perovskite $MAPbX_3$ single crystals have shown similar radiation detection capability. The outstanding performance of $MAPbX_3$ is due in part to its low density of trap states (10^9 - 10^{10} cm^{-3}) as well as its noticeably high values of resistivity (10^7 - $10^8 \text{ } \Omega\text{cm}$) and mobility-lifetime product (1.2 - $4.19 \times 10^{-2} \text{ cm}^2\text{V}^{-1}$) [37].

With a bandgap energy of 1.6 eV and a relative dielectric constant of 28, $MAPbI_3$ is a direct bandgap semiconductor. $MAPbI_3$ has a density of 4.3 g/cm^3 [74] and a high atomic number of ~ 49 [33]. In polycrystalline $MAPbI_3$ films, the electron and hole mobilities are ~ 8 and $\sim 15 \text{ cm}^2/\text{Vs}$, respectively [31] and the dark resistivity is $10^9 \text{ } \Omega\text{cm}$. $MAPbI_3$ has exceptionally longer lifetimes for both electrons, $\tau'_e=10 \text{ } \mu\text{s}$ and holes, $\tau'_h=17 \text{ } \mu\text{s}$ [33]. The effective masses of electrons and holes are 0.23 and 0.29 m_0 [75], respectively, where m_0 is the free electron mass. Three structural phases of $MAPbI_3$ have been identified: an orthorhombic $Pnma$ phase below 160K, a tetragonal $I4/mcm$ phase between 160 and 330K, and a cubic $Pm - 3m$ phase above

330K [73]. Hu et al. reported an MAPbI₃ wafer-based X-ray detector with high ambipolar carrier mobility of 20 cm²V⁻¹s⁻¹ and an extremely high $\mu\tau'$ product of 3.84x10⁴ cm²V⁻¹ [76]. With a 10 V bias, the detector displayed a sensitivity as high as 122,000 $\mu\text{CGy}_{air}^{-1}\text{cm}^{-2}$. However, the dark current was much higher, 2.5x10⁻⁵ Acm⁻² at electric field of 12.5 Vmm⁻¹. The MAPbI₃ single crystals exhibited record-breaking sensitivity above 700,000 $\mu\text{CGy}_{air}^{-1}\text{cm}^{-2}$ during X-ray irradiation, which permits an extremely low X-ray detection limit of 1.5 nGy_{air} s⁻¹ [77].

MAPbBr₃ has a bandgap of 2.3 eV [78], a density of 3.8 g/cm³, and a relative dielectric constant of 28 [79]. In crystalline MAPbBr₃, the electron and hole mobilities are 190 and 206 cm²/Vs [35], respectively. The atomic number is 45.1 [33]. At room temperature, MAPbBr₃ crystal adopts cubic *Pm-3m* space group. As the temperature dropped from 300K to 20K, the crystal go through three phase transformations, going from cubic to tetragonal, tetragonal to orthorhombic I, and orthorhombic I to orthorhombic II [80]. Huang et al. reported a Si-integrated MAPbBr₃ single crystal (SC) detector with a very high sensitivity of 2.1x10⁴ $\mu\text{CGy}_{air}\text{s}^{-1}$ and very low limit of detection (LoD) <0.1 μGys^{-1} [81]. Song et al. fabricated a MAPbBr₃ SC with low trap density 2.3x10⁹ cm⁻³ and resistivity 1.25x10⁸ Ωcm with excellent $\mu\tau'$ of 0.0259 cm²/V and sensitivity of 3928.3 $\mu\text{CGy}_{air}^{-1}\text{cm}^{-2}$ [82].

Prior to the incorporation of perovskites into industrial applications, a few issues must yet be resolved: scalability, sustainability, and stability are a few of these. Due to the presence of organic groups, the issue of the instabilities of organic-inorganic hybrid perovskite materials severely limits their application. Rapid material deterioration prevents perovskite devices from being commercially utilized [83]. Consequently, the goal of the upcoming research is to create high-detection sensitivity X-ray detectors based entirely on inorganic perovskites, which may provide similar optoelectronic properties without stability issues.

3.7.2 All Inorganic Lead Perovskites

The chemical formula for inorganic halide perovskites is ABX₃, where A is an inorganic cation (i.e, Cs⁺ or Rb⁺), B is a metal cation (e.g., Pb²⁺ or Sn²⁺), and X is a halide anion (i.e, I⁻, Br⁻, Cl⁻). It has been demonstrated that almost all-inorganic halide perovskites, such as CsPbBr₃, CsPbI₃, and their alloys (CsPbBr_xI_{3-x}), are more stable than MAPbI₃, while their optoelectronic properties are comparable to those of organic-inorganic hybrids [84] [85]. Due to their high X-ray absorption cross sections caused by the heavy atom compositions (such as Pb²⁺, I⁻), metal halide perovskite-based direct conversion detectors are promising candidates for such applications. Additionally, these

materials are solution-processable at low temperatures, show thermal stability, have tunable bandgaps, near-unity photoluminescence quantum yields, low trap density, high charge carrier mobility, and fast photoresponse times [86]. Recently, CsPbBr₃, CsPbI₃ inorganic lead halide perovskites have been explored for X-ray detection.

CsPbBr₃ is a stable inorganic perovskite with a bandgap of 2.36 eV [87] and the density of 4.42 g/cm³ [88]. The electron effective mass is $\sim 0.2m_e$ [87]. CsPbBr₃ goes through structural phase transformations from orthorhombic, space group *Pnma* (below 80°C) to tetragonal (80°C to 130°C) and eventually to cubic at a temperature greater than 130°C [89] [90] [91] [92] [93] [94]. Tang et al. fabricated thick quasi-monocrystalline films of CsPbBr₃ with high carrier mobility and a large $\mu\tau'$ product. The sensitivity of the fabricated X-ray detector was 55,684 $\mu\text{CGy}^{-1}\text{cm}^{-2}$ with a low detection limit of 215 nGy/s [95]. Matt et al. fabricated CsPbBr₃ film, where the hole mobility and the resistivity of the film were 18 cm²/Vs and 8.5 G Ωcm , respectively. The sensitivity of the X-ray detector was 1450 $\mu\text{CGy}^{-1}\text{cm}^{-2}$ [96].

CsPbI₃ is a thermally stable photoconductor with a bandgap of ~ 1.75 eV [97] and density of 4.54 g/cm³ [98]. Zhang et al. fabricated CsPbI₃ based X-ray detectors with low LoD of 0.219 μGys^{-1} , having high sensitivity of 2370 $\mu\text{CGy}^{-1}\text{cm}^{-2}$ for applied field of 4.17 Vmm⁻¹. The electron and hole mobilities are 44.3 ± 3.3 cm²V⁻¹s⁻¹ and 30.4 ± 1.9 cm²V⁻¹s⁻¹, respectively [99]. The difference in mobility is due to the difference in effective masses of the electron ($\sim 0.2m_0$) and hole ($\sim 0.9m_0$). The electron and hole lifetimes are 81.9 μs and 119.4 μs , respectively. The reported resistivity of CsPbI₃ is as large as $7.4 \times 10^9 \Omega\text{cm}$ [99]. At ambient conditions, CsPbI₃ crystals adopt orthorhombic phase (*Pnma*) and transformed to cubic phase (*Fm-3m*) at $\sim 310\text{K}$. Also at high pressure (3.9 GPa), the phase transformation from orthorhombic to monoclinic (*P2₁/m*) has been observed [100].

Despite the large detection sensitivity, low detection limit, and high charge carrier range of organic-inorganic hybrid lead halide perovskite and inorganic lead halide perovskites X-ray detectors, lead has emerged as the biggest barrier to their development. The toxic lead, which is related to brain complications, can be easily dissolved in water or in humid air and infiltrate the soil, thus polluting the environment and harming human health. 3,336 g Pb per m² is found in a 2 mm thick MAPbBr₃ SC-based FPXI, which is significantly above the EU RoHS regulatory limit of 1,000 ppm Pb [37] [101]. Finding a Pb-free alternative imager with superior sensitivity and detection limits is therefore crucial for X-ray detection applications. All-inorganic lead-free perovskite materials have the potential to be more environmentally friendly and some of them have improved thermal, light, and environmental stability, allowing for longer device life and less environmental contamination [37].

3.8 3D Double Perovskite : $\text{Cs}_2\text{AgBiBr}_6$

Lead-free double perovskites are among the most promising lead-free perovskite candidates for X-ray detection due to their structural and functional diversity, excellent thermal and light stability, and suitable optical and electrical properties for use in a variety of optoelectronic applications. The X-ray detectors based on all-inorganic lead-free perovskite materials are anticipated to have the potential to achieve high detection sensitivity with minimal environmental pollution concerns and stability issues by optimizing the material growth and the device fabrication process. These materials possess a diverse range of characteristics, such as excellent stability against air and moisture, non-toxicity, low carrier effective masses, a long carrier recombination lifetime, and the capacity to absorb visible light. By using a first-principles calculation method, Sun and Yin have thoroughly investigated the thermodynamic stabilities of 138 cubic perovskite materials [102]. By carefully regulating the material synthesis procedure, high-quality perovskite SCs can be produced, which is particularly advantageous for lowering leakage current, device noise, and material defects [45]. X-ray detectors using low-cost solution-processed lead-free double perovskite $\text{Cs}_2\text{AgBiBr}_6$ (CABB) single crystal has been demonstrated in recent years. The $\text{Cs}_2\text{AgBiBr}_6$ photoconductor is well suited for usage as a radiation sensor due to its chemical components and crystalline structure. Due to the fact that the breakdown enthalpy of the $\text{Cs}_2\text{AgBiBr}_6$ single crystal (SC) is greater than zero ($\Delta H_D > 0$), stability was predicted [45]. In addition to being exceptionally stable under moisture, heat, and light exposure conditions, $\text{Cs}_2\text{AgBiBr}_6$ do not contain toxic lead elements [103]. The perovskite CABB has a high optical absorption coefficient, strong thermoelectric transport characteristics, and mechanical stability. $\text{Cs}_2\text{AgBiBr}_6$ has a large average atomic number $Z=53.1$ [37], compared to MAPbI_3 and MAPbBr_3 's $Z = 49$ and 45.1 , respectively, and its density is 4.92 g/cm^3 [104], which results in a high probability for X-ray absorption. This is important since it affects the ultimate electrical signal output. Enhanced absorption enables the material to completely absorb X-ray photons while maintaining a reduced layer thickness. Due to the low energy of the X-rays and the high atomic number of the $\text{Cs}_2\text{AgBiBr}_6$ perovskite materials, the interaction between the X-rays and the material is predominantly a photoelectric process rather than a Compton scattering or pair production process [37]. When X-ray photons hit on the $\text{Cs}_2\text{AgBiBr}_6$ SC, many electron-hole pairs will be photogenerated. These EHPs will travel under the influence of an externally created electric field until they are eventually gathered by the electrodes at both ends, resulting in the generation of the photocurrent. Suppressed ion migration in $\text{Cs}_2\text{AgBiBr}_6$ permits relatively large external bias, guaranteeing efficient charge collection without a substantial increase in noise current and thus enabling the low detection limit. The electron and hole

effective masses of CABB are $\sim 0.37m_e$ and $\sim 0.14m_e$ [105], respectively, where m_e is the electron rest mass and the electron-hole pair creation energy (W_{\pm}) of $\text{Cs}_2\text{AgBiBr}_6$ is much lower (~ 5.61 eV) than a-Se (~ 45 eV at $10 \text{ V}\mu\text{m}^{-1}$) [37]. The relative dielectric constant of CABB is 51. This solution-processed compound is primarily an indirect bandgap material having E_g range from 1.7 eV to 2.19 eV [38], higher resistivity than other perovskites (10^9 – $10^{11} \Omega\text{cm}$), similar trap density ($\sim 10^9 \text{ cm}^{-3}$), moderate μ (0.5 – $12 \text{ cm}^2/\text{Vs}$), and good sensitivity (105 – $1974 \mu\text{CGycm}^{-2}$) [37] [104], which is multiple times superior to commercial a-Se based detectors with a sensitivity of $20 \mu\text{CGy}^{-1}\text{cm}^{-2}$ at $10 \text{ V}\mu\text{m}^{-1}$ [37] and low detection limits of 45.7 – 59.7 nGy/s [104] [37], which is comparable to MAPbBr_3 single crystals' detection limit of $36 \mu\text{Gys}^{-1}$ [37]. These electrical and radiation detection performance parameters reflect the beneficial chemical composition and crystal structure of the $\text{Cs}_2\text{AgBiBr}_6$ radiation sensor material.

3.8.1 Structure and Chemical Bonds

The chemical formula for 3D double perovskite is $\text{A}_2\text{B}_I\text{B}_{II}\text{X}_6$. In order to replace toxic Pb in lead halide perovskites, and maintain the structure's three-dimensional connectivity, $\text{Cs}_2\text{AgBiBr}_6$ double perovskite employs a heterovalent substitution approach using a monovalent Ag^+ and trivalent Bi^{3+} metal cations as replacements. $\text{Cs}_2\text{AgBiBr}_6$ SC exhibits a face-centered cubic double perovskite structure and belongs to the $Fm - 3m$ space group at room temperature. The lattice parameter is 11.27 \AA . Compared to the MAPbX_3 , this structure allows for more flexibility [105] [106] [107]. With the rock-salt arrangement of the B-crystallographic site cations in the double perovskite, $\text{Cs}_2\text{AgBiBr}_6$ belongs to the elpasolite class of minerals ($\text{A}_2\text{B}^+\text{B}^{3+}\text{X}_6$). In this rock salt arrangement, the corners of the $[\text{AgBr}_6]^{5-}$ and $[\text{BiBr}_6]^{3-}$ octahedra are connected in all 3D and the Cs^+ are positioned in the structural cavities (A-site). The structure of $\text{Cs}_2\text{AgBiBr}_6$ is displayed in Figure 3.4 [108]. The electronic structure and, consequently, the optoelectronic properties of perovskites are greatly influenced by the structure of the octahedra. Since the two types of octahedra are electrically isolated, there is zero electronic dimensionality, which leads to comparatively higher effective masses of charge carriers [109]. Since the measured effective mass for holes is smaller than that for electrons in the cubic phase, it is expected that holes have greater mobility than electrons. Considering the crystal's shape and constitution, a higher charge carrier-lattice interaction than in the MAPbX_3 might result in self-trapped charges, which invariably results in lower $\mu\tau'$ [110] [111] [112].

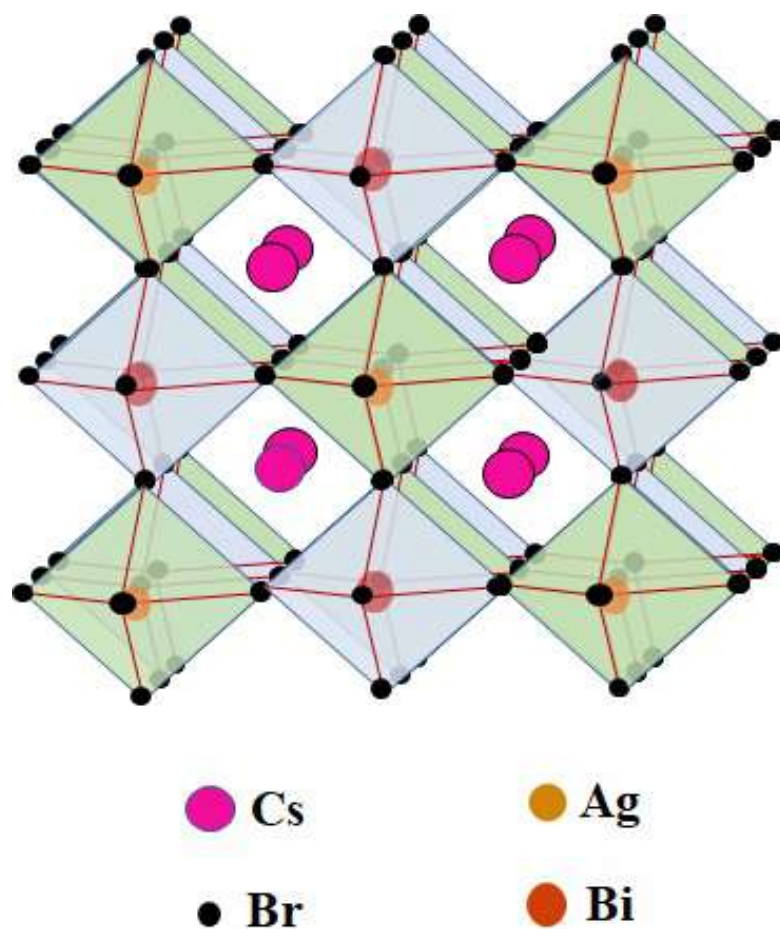


Figure 3.4: A single crystalline $\text{Cs}_2\text{AgBiBr}_6$ double perovskite unit cell. Small black spheres represent Br^- , large magenta spheres represent Cs^+ , and light green and blue octahedrons represent $[\text{AgBr}_6]^{5-}$ and $[\text{BiBr}_6]^{3-}$, respectively.

The Ag-Br/Bi-Br and Ag-Br-Bi bonds in the $\text{Cs}_2\text{AgBiBr}_6$ crystal all preserve a 90° or 180° angle [Figure 3.4], and the Ag-Br and Bi-Br bonds have similar lengths (2.804-2.828 Å). Since the electrons are more closely connected to the atoms with a reduced bond length than with MAPbI_3 , the $\text{Cs}_2\text{AgBiBr}_6$ structure has stronger bonds and is more robust [113].

The atomic electronic configurations for CABB: Cs: $[\text{Kr}] 4d^{10}5s^2 5p^6 6s^1$, Ag: $[\text{Kr}] 4d^{10} 5s^1$, Bi: $[\text{Xe}] 4f^{14} 5d^{10} 6s^2 6p^3$ and Br: $[\text{Ar}] 3d^{10} 4s^2 4p^5$. The Cs p and d states do not contribute to the band edges, however, through bonding interactions between Cs^+ and the metal framework, they can affect the band structure. The band edges are primarily made up of the states of Ag, Bi, and Br. While Ag-s and Bi-p states contribute to the formation of the valence band maximum (VBM), Ag-d and Bi-s states are primarily responsible for the conduction band minimum (CBM). The Br-p orbital contributes to both VBM and CBM. The indirect bandgap character of CABB is caused

by the hybridization of Ag and Bi orbitals near band edges [113] [114]. $\text{Cs}_2\text{AgBiBr}_6$ has a large bandgap of ~ 2 eV, which leads to low thermal noise in the device.

No phase transition was reported in the face-centered cubic crystal of the lead-free halide double perovskite $\text{Cs}_2\text{AgBiBr}_6$ up to 703 K. However, by lowering the temperature, modifying the material's dimensions, employing a high-pressure treatment, or adding additional elements to the lattice, phase transitions (cubic, tetragonal, monoclinic, and triclinic) may happen. This causes distortion or tilting of the crystal lattice, especially the distortion in $[\text{AgBr}_6]^{5-}$ octahedra is more dominant. Recent studies have shown that $\text{Cs}_2\text{AgBiBr}_6$ double perovskite transitioned from cubic (space group $Fm - 3m$) to tetragonal structure (space group $I4/m$) when it cools at 122 K with a high applied pressure of 2.3 GPa [113] [114].

3.8.2 Defects in $\text{Cs}_2\text{AgBiBr}_6$

Throughout the synthesis and processing of photoconductive materials, several defects are unavoidably produced. Depending on the fabrication process, impurities, and structural defects, therefore, the mobility-lifetime products, and deep trap density may differ significantly from sample to sample. The most significant shallow defects in CABB are V_{Ag} (acceptor) due to low formation enthalpy [113] and Ag_i (donor), however, these shallow defects do not hamper optoelectronic properties of the device. The acceptor shallow defects contribute to the intrinsic p-type characteristics of $\text{Cs}_2\text{AgBiBr}_6$. The deep defects are Bi_{Ag} , Ag_{Bi} , Bi vacancies, and Br vacancies [113] [115] and affect device performance by acting as trapping and non-radiative recombination centers. The weakly p-type and defect-filled $\text{Cs}_2\text{AgBiBr}_6$ perovskite materials allow photogenerated holes to be transported and trap electrons. By carefully regulating the material synthesis process, high-quality perovskite SCs with minimal defects can be developed. After thermal annealing, defect density in $\text{Cs}_2\text{AgBiBr}_6$ can be reduced to $\sim 10^9 \text{ cm}^{-3}$ [37].

Ionic migration in $\text{Cs}_2\text{AgBiBr}_6$ occurs from the drift of Br^- ions from lattice sites through Br vacancies [116] since Br vacancies have the lowest diffusion barrier of 0.33 eV and shortest migration distance [37]. Migration of Br^- anions and their accumulation at the electrodes affects the internal electric field of the detector [108]. Ionic migration directly affects the input and output signals [42]. However, the effective activation energy for $\text{Cs}_2\text{AgBiBr}_6$ SCs is reported to be 348 meV, much larger than MAPbBr_3 (168 meV) [117] which indicates that the ionic migration in $\text{Cs}_2\text{AgBiBr}_6$ is much lower than MAPbBr_3 . Suppressing ionic conductivity and reducing defects will result in the enhancement of resistivity and mobility-lifetime product as well.

3.8.3 Linear Attenuation Coefficient

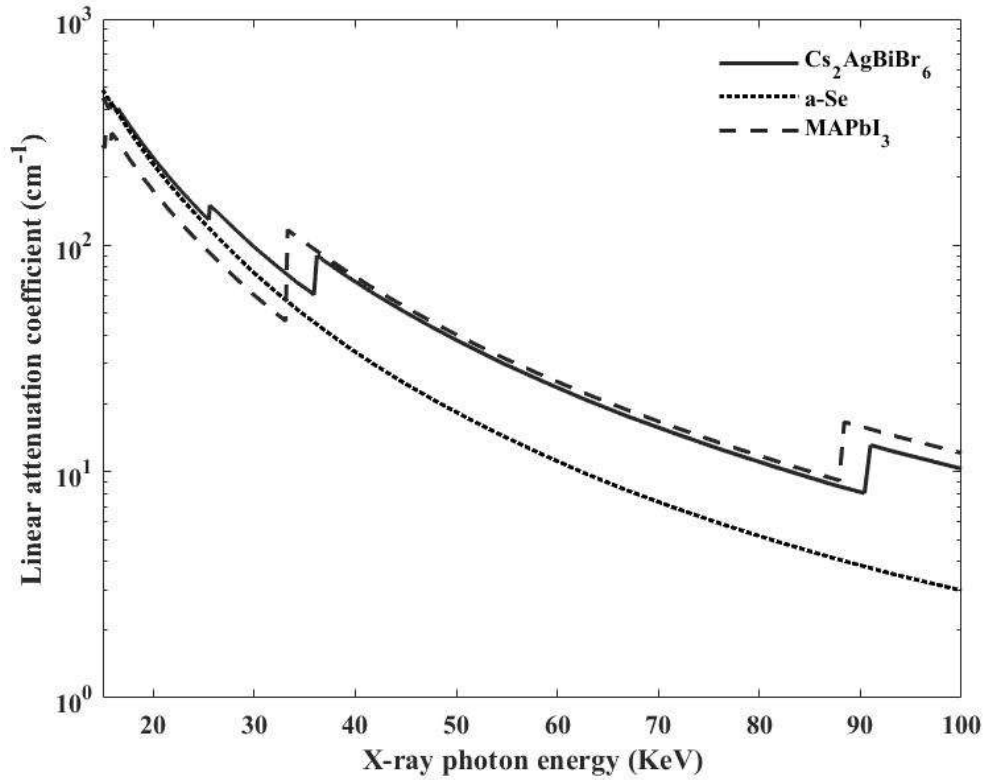


Figure 3.5: Linear attenuation coefficients of $\text{Cs}_2\text{AgBiBr}_6$, MAPbI_3 and a-Se at different X-ray energies.

The linear attenuation coefficient, $\alpha \propto Z^4/E^3$, where Z is the atomic number and E is the radiation energy. Since one of the constituents of $\text{Cs}_2\text{AgBiBr}_6$ is the heaviest stable element, Bi, it has a comparatively high Z value of 53.1, which is beneficial for better absorption of radiation. Figure 3.5 shows the linear attenuation coefficients of $\text{Cs}_2\text{AgBiBr}_6$ in comparison to hybrid lead halide perovskite (MAPbI_3) and a-Se as a function of X-ray photon energies. The values of linear attenuation coefficients are obtained from the database of the National Institute of Standards and Technology (NIST) [118]. $\text{Cs}_2\text{AgBiBr}_6$ has higher linear attenuation coefficients than a-Se have as well as MAPbI_3 for X-ray photon energy less than 33.1 keV. Again, it is evident that the linear attenuation coefficients of $\text{Cs}_2\text{AgBiBr}_6$ are much higher than a-Se for X-ray photon energy above 36 keV, which leads to the superiority of $\text{Cs}_2\text{AgBiBr}_6$ for high energy X-ray detection.

3.9 Summary

The X-ray imaging capabilities of several existing and potential photoconductors for X-ray image detectors have been addressed. Stabilized a-Se is currently available in the digital X-ray imaging industry. With excellent optoelectronic properties recently perovskites have emerged as potential X-ray detectors. With advantageous traits and intriguing possibilities, $\text{Cs}_2\text{AgBiBr}_6$ halide double perovskite has laid the foundations for the future generation of X-ray detectors. Our study contributes to a better understanding of the remarkable radiation detection capabilities that this double perovskite material offers.

Table 3.1 and Table 3.2 list the features of different photoconductors for direct X-ray detection.

Table 3.1: Properties of different photoconductor materials used in X-ray detection

Properties	a-Se	HgI ₂	PbI ₂	CdZnTe
D(g/cm ³)	4.3	6.3	6	5.8
E _g (eV)	2.22	2.1	2.3	1.57
Z	34	62	62.7	-
W _± (eV)	-	~5	~5	~5
ε _r	6.7	-	-	11
ρ(Ωcm)	~10 ¹⁴	~4x10 ¹³	~10 ¹¹ -10 ¹²	~10 ¹¹
μτ'(cm ² /V)	10 ⁻⁷ -10 ⁻⁵	10 ⁻⁶ -10 ⁻⁴	10 ⁻⁸ -10 ⁻⁶	10 ⁻⁶ -10 ⁻⁴
S(μC/Gycm ²)	20	1600	1200	2400
LoD(nGy/s)	5500	10000	<52.8	50000
Ref	[8] [15]	[8] [66] [67] [68]	[8] [15] [66] [71]	[8] [70] [86] [119] [120]

Table 3.2: Properties of different perovskite photoconductors

Properties	MAPbI ₃	MAPbBr ₃	CsPbBr ₃	CsPbI ₃	Cs ₂ AgBiBr ₆
D(g/cm ³)	4.3	3.8	4.42	4.54	4.92
E _g (eV)	1.6	2.3	2.36	1.75	1.7-2.19
Z	49	45	-	-	53.1
W _± (eV)	~5	~5.3	~6	~5	5.61
ε _r	28	28	-	-	51
ρ(Ωcm)	~10 ⁸	~10 ⁸	8.5x10 ⁹	7.4x10 ⁹	~10 ⁹ -10 ¹¹
μτ'(cm ² /V)	10 ⁻⁴ -10 ⁻³	10 ⁻⁴ -10 ⁻²	10 ⁻²	10 ⁻³	~10 ⁻³
S(μC/Gycm ²)	700000	3928.3	55684	2370	105-1974
LoD(nGy/s)	1.5	<8800	215	219	45.7-59.7
Ref	[33] [74] [77] [121]	[33] [78] [79] [121]	[33] [87] [88] [95]	[33] [97] [98] [99]	[33] [37] [38] [104]

Chapter 4

Photocurrent in X-ray Detector

4.1 Introduction

The photocurrent is the induced electric current due to the movement of free charges generated from the absorption of photons in the photoconductor. In the event that X-rays are absorbed by a photoconductor, many electron-hole pairs (EHPs) are generated. The generated EHPs follow an exponential distribution in the device following the exponential absorption profile. The applied electric field causes these EHPs to migrate in the direction of the opposite electrodes. The introduction of mobile carriers into the photoconductive detector causes currents that are totally attributable to induction since there is no availability of free carriers present in the photoconductors to surround drifting carriers and maintain local charge neutrality. Since there is generated charge concentration gradient in the detector, diffusion of charges is present. Therefore, both drift and diffusion of charges contribute to the current.

A direct conversion X-ray image detector's cross-sectional simplified structure is shown in Figure 4.1. An X-ray absorber layer made of photoconductive material, such as $\text{Cs}_2\text{AgBiBr}_6$, is inserted between two metal electrodes placed at the top and bottom. The generated charges are collected at the electrodes by applying an electric field across the detector. To create a uniform electric field F_0 in the photoconductor, a bias voltage V (either positive or negative) is applied to the radiation-receiving electrode. The top electrode is assumed to be positively biased.

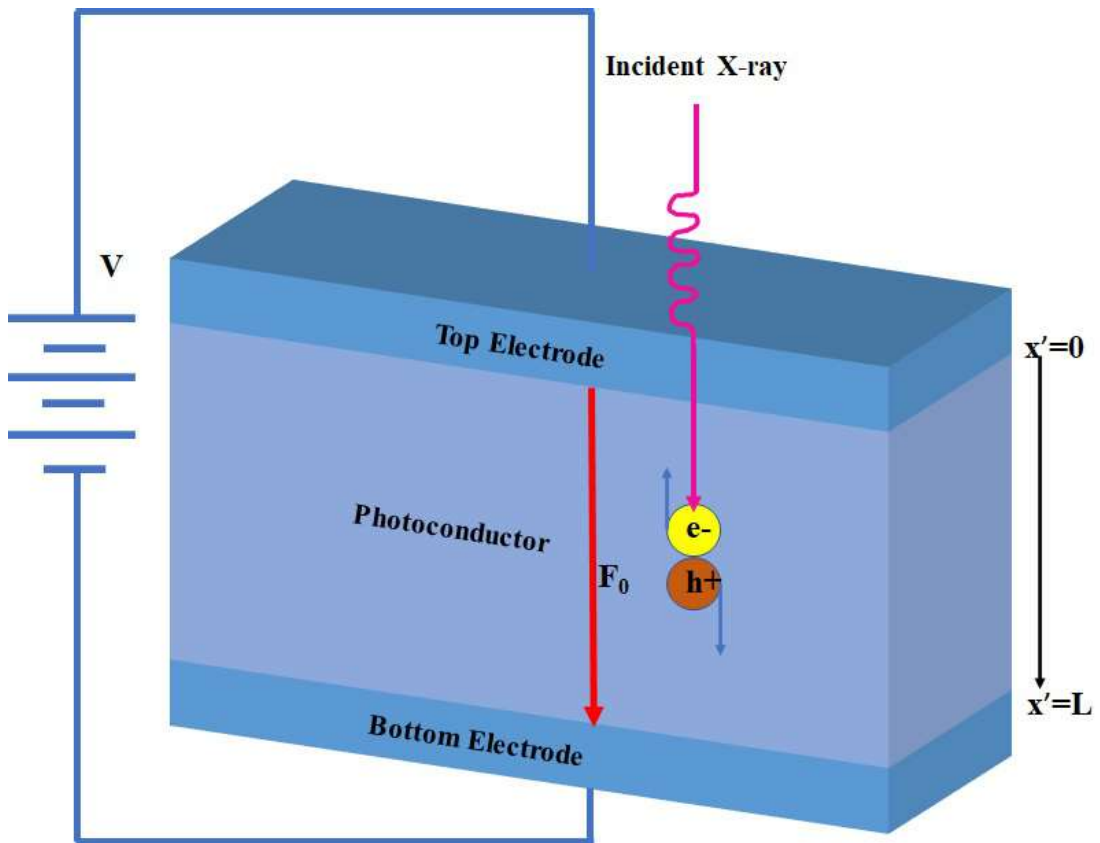


Figure 4.1: Basic structure of an X-ray image detector.

4.2 Analytical Model of Photocurrent

The analytical model of transient photocurrent in an X-ray detector was developed by Sincita et al. [39]. The photocurrent was developed by solving the carrier continuity equations for both holes and electrons. It was assumed that the amount of space charge carriers generated after the application of X-rays for medical diagnostics is insufficient to disturb the electric field distribution across the photoconductor. Hence, during operation, the electric field was considered uniform along the detector thickness. Additionally, it was assumed the applied electric field is high enough, hence diffusion of X-ray-generated carriers is insignificant compared to drift.

The continuity equations for holes and electrons, after the application of positive bias to the illuminated electrode during irradiation, are as follows:

$$\frac{\delta p'(x', t')}{\delta t'} = -\mu_h \frac{\delta p'(x', t') F_0}{\delta x'} - \frac{p'(x', t')}{\tau'_h} + G_0 e^{-\alpha x'} \quad (4.1)$$

$$\frac{\delta n'(x', t')}{\delta t'} = \mu_e \frac{\delta n'(x', t') F_0}{\delta x'} - \frac{n'(x', t')}{\tau'_e} + G_0 e^{-\alpha x'} \quad (4.2)$$

Here, $p'(x', t')$ is the hole concentration at position x' at time t' , $n'(x', t')$ is the electron concentration at position x' at time t' , $F_0 (= V/L)$ is the applied electric field, that is uniform along the photoconductor thickness, V is the applied bias and L is the thickness of the photoconductor. $\mu_{h(e)}$ is the hole (electron) mobility, $\tau'_{h(e)}$ is the hole (electron) lifetime, G_0 is the EHP generation rate at $x' = 0$ for an X-ray dose of X of energy of E_{ph} , α is the linear attenuation coefficient of the photoconductor for X-ray energy of E_{ph} in eV. The EHP generation rate is assumed to decay exponentially towards the bottom electrode since the charge generation tracks the X-ray absorption profile across the photoconductor thickness. The photon fluence is

$$\phi_0 = \frac{5.45 \times 10^{13} X}{(\alpha_{air}/\rho_{air}) E_{ph}} \quad (4.3)$$

where ϕ_0 is photons/cm⁻², α_{air} and ρ_{air} are the energy absorption coefficient and the density of air, respectively, and α_{air}/ρ_{air} is in cm²g⁻¹. Considering the photon fluence is ϕ_0 , the EHPs generation rate becomes

$$G_0 = \frac{\phi_0 E_{ph} \alpha}{T_{ex} W_{\pm}} \quad (4.4)$$

Here, G_0 is in cm⁻³s⁻¹, T_{ex} is the total exposure time, and W_{\pm} is the EHP generation energy in eV at an electric field of F_0 .

The generated holes drift toward the bottom electrode and electrons move toward the top electrode due to the applied bias. The initial condition for holes is $p'(x', 0) = 0$. The holes' movement towards the bottom electrode is immediate, hence the boundary condition is $p'(0, t') = 0$. Using a similar line of argument used for holes, the initial condition for electrons is $n'(x', 0) = 0$ and the boundary condition for electrons is $n'(L, t') = 0$, assuming the transfer of electrons towards the top electrode. The solutions of continuity equations for holes and electrons described in equations (4.1) and (4.2) using initial and boundary conditions are [39]

$$p'(x', t') = \begin{cases} A e^{-\alpha x'} (1 - e^{-\frac{t'}{\tau'_h} + \alpha \mu_h F_0 t'}); & x' > \mu_h F_0 t' \\ A (e^{-\alpha x'} - e^{-\frac{x'}{\mu_h \tau'_h F_0}}); & x' < \mu_h F_0 t' \end{cases} \quad (4.5)$$

$$n'(x', t') = \begin{cases} B e^{-\alpha x'} (1 - e^{-\frac{t'}{\tau'_e} - \alpha \mu_e F_0 t'}); & L - x' > \mu_e F_0 t' \\ B (e^{-\alpha x'} - e^{-\alpha L} e^{-\frac{L-x'}{\mu_e \tau'_e F_0}}); & L - x' < \mu_e F_0 t' \end{cases} \quad (4.6)$$

Here, $A = \frac{G_0\tau'_h}{1-\alpha\mu_h\tau'_hF_0}$ and $B = \frac{G_0\tau'_e}{1+\alpha\mu_e\tau'_eF_0}$.

The hole photocurrent density is given by

$$j'_h(t') = \frac{(e\mu_hF_0)}{L} \int_0^L p'(x', t') dx' \quad (4.7)$$

The electron photocurrent density is given by

$$j'_e(t) = \frac{(e\mu_eF_0)}{L} \int_0^L n'(x', t') dx' \quad (4.8)$$

Replacing $p'(x', t')$ and $n'(x', t')$ in equations (4.7) and (4.8), using the expressions from equations (4.5) and (4.6) the hole and electron photocurrent densities are obtained.

$$j'_h(t') = \begin{cases} \frac{Ae\mu_hF_0}{\alpha L} \{(1 - e^{-\frac{t'}{\tau'_h}})(1 - \alpha\mu_h\tau'_hF_0) - e^{-\alpha L}(1 - e^{-\frac{t'}{\tau'_h} + \alpha\mu_hF_0t'})\}; & 0 < t' < t_h \\ \frac{Ae\mu_hF_0}{\alpha L} (1 - \alpha\mu_h\tau'_hF_0 + \alpha\mu_h\tau'_hF_0e^{-\frac{t_h}{\tau'_h}} - e^{-\alpha\mu_hF_0t_h}); & t' > t_h \end{cases} \quad (4.9)$$

$$j'_e(t') = \begin{cases} \frac{Be\mu_eF_0}{\alpha L} \{(1 - e^{-\frac{t'}{\tau'_e} - \alpha\mu_eF_0t'}) - e^{-\alpha L}(1 - e^{-\frac{t'}{\tau'_e}})(1 + \alpha\mu_e\tau'_eF_0)\}; & 0 < t' < t_e \\ \frac{Be\mu_eF_0}{\alpha L} \{1 - e^{-\alpha L} - e^{-\alpha L}(1 - e^{-\frac{t_e}{\tau'_e}})\alpha\mu_e\tau'_eF_0\}; & t' > t_e \end{cases} \quad (4.10)$$

Here, $t_h(= \frac{L}{\mu_hF_0})$ and $t_e(= \frac{L}{\mu_eF_0})$ are hole and electron transit time, respectively.

The total photocurrent density is

$$j_T(t') = j'_h(t') + j'_e(t') \quad (4.11)$$

4.3 Dark Current

One of the primary sources of noise in image sensors is dark current. Dark current is a fairly small electric current that runs through photosensitive devices in the absence of photons. It is made up of the charges generated in the detector when no outside radiation enters the device. A superior photoconductor should have the smallest dark current possible. For diagnostic X-ray imaging applications, a dark current of less than 100 pA/cm² is preferable to achieve an enhanced dynamic range of the detector [44]. The dark current originated from either thermally generated carriers or contact-injected carriers, hampers the dynamic range of the detector. The addition of these charges with the photogenerated charges disturbs the original signal.

4.3.1 Origin of Dark Current

The inherent dark current of a semiconductor is often attributable to either bulk thermal generation within the photoconductor or charge carrier injection from the metal contacts into the semiconductor. Thermal generation normally contributes insignificantly to dark current since the choice of photoconductive materials in X-ray detectors ensures that they have a relatively wide bandgap (>1 eV). However, charge injection from metal contacts may not be as insignificant under the applied bias voltage.

The two main mechanisms of the dark current of an X-ray imager are:

a) Contact injection current

b) Bulk thermal generation current

(a) Contact Injection Current: The origin of contact injection current is the injection of carriers from the metal to the semiconductor. The carrier injection is a function of the junction electric field, effective barrier height at the interface, and junction states. The injected current densities from the injection of holes and electrons are [44]

$$J_{(hinj)} = eN_V v_{dh} \frac{v_R}{v_{dh} + v_R} e^{-\frac{\phi_h - \beta_s \sqrt{F_1}}{kT}} \quad (4.12)$$

$$J_{(einj)} = eN_C v_{de} \frac{v_R}{v_{de} + v_R} e^{-\frac{\phi_e - \beta_s \sqrt{F_2}}{kT}} \quad (4.13)$$

Here, $N_{V(C)}$ is the effective density of states in the valence (conduction) band, $v_{de(h)}$ is the drift velocity of electron (hole) and v_R is the thermal velocity. F_1 and F_2 are the electric fields at the top and bottom metal/photoconductor interfaces, respectively. β_s ($=\sqrt{\frac{e^3}{4\pi\epsilon_s}}$) is the Schottky coefficient, ϵ_s is the dielectric constant of the photoconductor. $\phi_{h(e)}$ is the effective barrier height that is required to be overcome by the holes (electrons) to be injected from the contact to the photoconductor.

During the $\text{Cs}_2\text{AgBiBr}_6$ film fabrication, several intrinsic point defects (e.g. elemental vacancies, interstitials, cation-on-cation antisites, cation-on-anion antisites, and anion-on-cation antisites) may form [115], although formation enthalpies of these defects are relatively too high to facilitate their formation. However, Ag vacancies (V_{Ag}) can form comparatively easily, making $\text{Cs}_2\text{AgBiBr}_6$ p-type. The energy barriers for Cs, Bi, Ag, and Br ions migration are 1.413, 3.363, 0.895, and 0.43 eV, respectively [122]. Therefore, the Br and Ag ions primarily move when intrinsic vacancies exist. The ions slowly move to the ion-blocking electrodes (e.g., Au) under the influence of an applied electric field [123], resulting in the formation of ion-accumulation layers near the metal/photoconductor interfaces. The presence of accumulated ions perturbs the electric field and instead of a uniform field (F_0), causes elevation of the electric field at the interfaces. The elevation depends on the accumulated charge concentration and width of

the accumulation layer. Figure 4.2 shows the electric field profile in the presence of accumulation layers. F_1 and F_2 are the elevated electric fields at the top and bottom interface, respectively. F_3 is the electric field in the bulk.

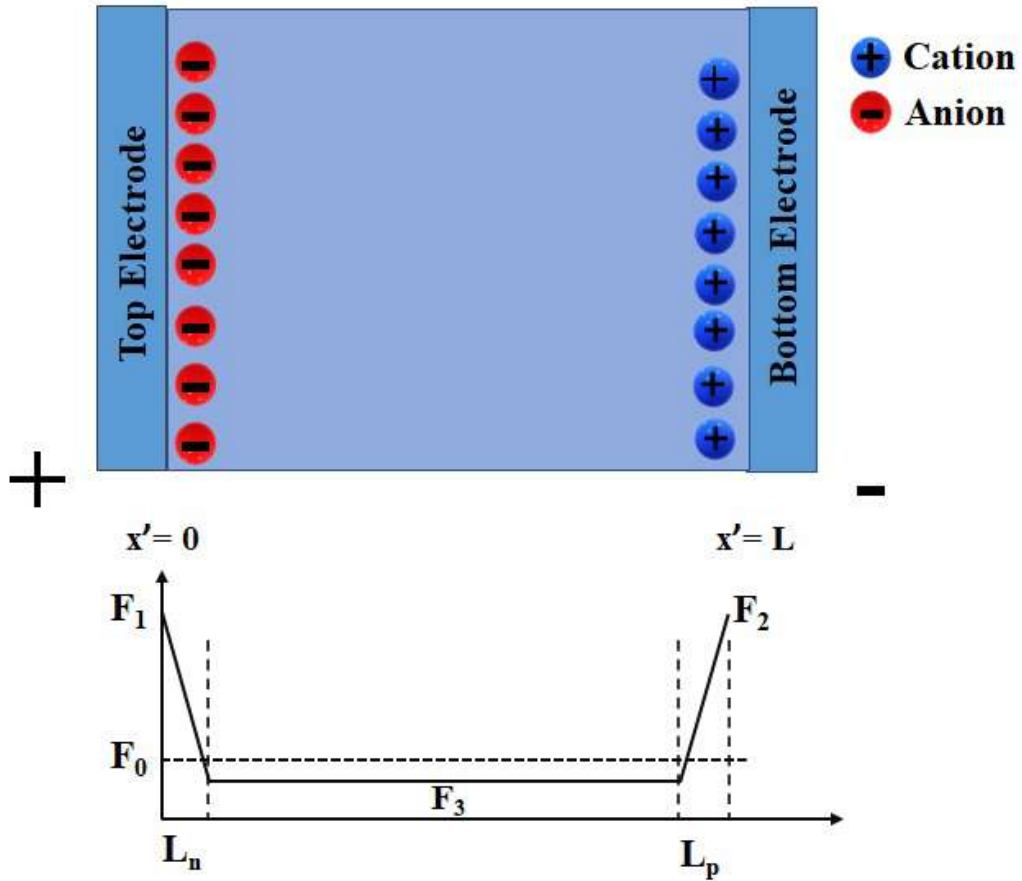


Figure 4.2: Electric field distribution across the photoconductor in the presence of accumulated ions near the photoconductor/metal interfaces.

If the thermal velocity is much greater than the drift velocity, ($v_R \gg v_{de(h)}$), equations 4.12 and 4.13 become

$$J_{(hinj)} = eN_V\mu_h F_1 e^{-\frac{\phi_h - \beta_s \sqrt{F_1}}{kT}} \quad (4.14)$$

$$J_{(einj)} = eN_C\mu_e F_2 e^{-\frac{\phi_e - \beta_s \sqrt{F_2}}{kT}} \quad (4.15)$$

The total injection current density is

$$J_{(inj)} = J_{(einj)} + J_{(hinj)} \quad (4.16)$$

It is apparent from equations (4.14) and (4.15) that the injection current depends on the interface electric field and effective barrier height for holes (electrons) to inject

from top (bottom) electrodes to the photoconductor. Figure 4.3 and Figure 4.4 show two possible contacts between metal and p-type semiconductors: the Schottky contact and the ohmic contact. When the work function of the metal is lower than the work function of p-type material ($\phi_M < \phi_S$), Schottky contact is established. If the work function of the metal is higher than the work function of p-type material ($\phi_M > \phi_S$), ohmic contact is established. The effective barrier height for ohmic contact depends on the band bending near the interfaces due to the presence of interface states. Ohmic contacts with low resistance permit charge to flow in both directions.

The barrier height for holes to flow from positively biased electrode to photoconductor can be determined by

$$\phi_h = \chi + E_g - \phi_M \quad (4.17)$$

The barrier height for electrons to flow from the negatively biased electrode to the photoconductor can be determined by

$$\phi_e = \phi_M - \chi \quad (4.18)$$

Here, χ is the electron affinity of the semiconductor, E_g is the bandgap of it and ϕ_M indicates the work function of the metal.

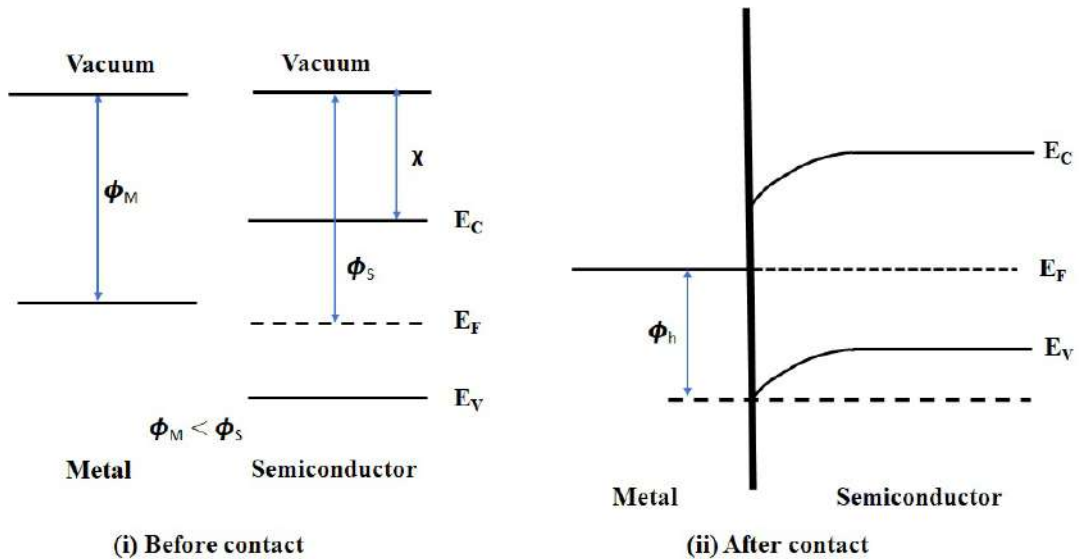


Figure 4.3: Schottky contact between metal and p-type semiconductor.

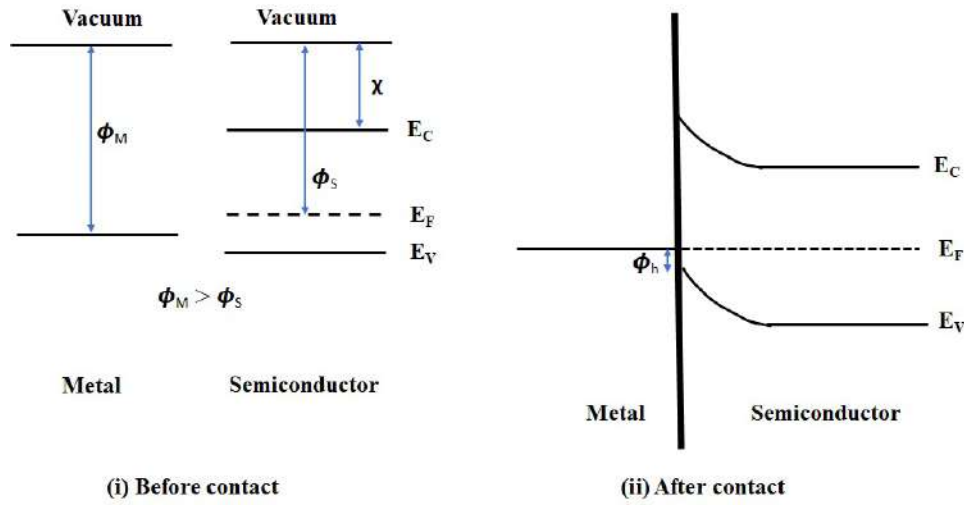


Figure 4.4: Ohmic contact between metal and p-type semiconductor.

Figure 4.5 shows the energy level diagram of the $\text{Cs}_2\text{AgBiBr}_6$ single crystal and different electrodes (i.e. Au, Ag, Al). The work function of Au, Al, and Ag are 5.1, 4.28, and 4.26 eV, respectively. The electron affinity of CABB is 3.64 eV [124]. The Fermi level is reported to be ~ 0.788 eV above of valence band [125] for p-type $\text{Cs}_2\text{AgBiBr}_6$ and the bandgap is ~ 2.1 eV. The work function of CABB (ϕ_s) is ~ 4.9 eV, which is greater than the work function of Al and Ag, but less than that of Au. Hence, Ag/p- $\text{Cs}_2\text{AgBiBr}_6$ and Al/p- $\text{Cs}_2\text{AgBiBr}_6$ are Schottky contacts, whereas Au/p- $\text{Cs}_2\text{AgBiBr}_6$ is ohmic contact. However, the dark conductivity (σ) of $\text{Cs}_2\text{AgBiBr}_6$ is $\sim 10^{-11}$ S/cm [37]. Assuming ohmic contact for Au/p- $\text{Cs}_2\text{AgBiBr}_6$, the dark current density ($=\sigma F_0$) is 0.25 nA/cm² when a 5 V is applied across a 2 mm detector, which is almost twice the measured dark current for this device that is ~ 0.15 nA/cm² [37]. Hence, it can be concluded that the contact is weakly Schottky type due to the presence of interface states [125] [121]. For Ag/ $\text{Cs}_2\text{AgBiBr}_6$ /Ag X-ray detector, the hole barrier height (ϕ_h) is $\sim (3.64+2.1-4.26)$ eV ~ 1.48 eV. The electron barrier height (ϕ_e) is $\sim (4.26-3.64)$ eV ~ 0.62 eV. For Au/ $\text{Cs}_2\text{AgBiBr}_6$ /Au X-ray detector, the hole barrier height (ϕ_h) is $\sim (3.64+2.1-5.1)$ eV ~ 0.64 eV and the electron barrier height (ϕ_e) is $\sim (5.1-3.64)$ eV ~ 1.46 eV. Therefore, the hole injection in Ag/ $\text{Cs}_2\text{AgBiBr}_6$ and the electron injection in Au/ $\text{Cs}_2\text{AgBiBr}_6$ can be ignored since barrier height is greater than 1 eV.



Figure 4.5: The energy level diagram of the $\text{Cs}_2\text{AgBiBr}_6$ single crystal and different electrodes (Au, Ag, and Al).

(b) Bulk Thermal Generation Current: In a semiconductor crystal lattice, all the atoms should be in perfect alignment and free from imperfections. Yet, during the growth and processing of materials, several defects are unavoidably produced. The four basic types of defects found in semiconductors are point defects, line defects, plane defects, and bulk defects. Point defects include vacancies, interstitials, and antisites. These defects create localized states in the forbidden band. The bulk thermal generating current is the flow of generated charges through these band-gap states. Electron-hole pairs are produced as a result of the excitation of electrons from the valence band to empty gap states and from the filled traps to the conduction band. These thermally generated carriers drift under the influence of the electric field and are later collected at the electrodes. The continuity equations for thermally generated charges are

$$\frac{\delta p'(x', t')}{\delta t'} = -\mu_h F_0 \frac{\delta p'(x', t')}{\delta x'} - \frac{p'(x', t')}{\tau'_h} + g_h \quad (4.19)$$

$$\frac{\delta n'(x', t')}{\delta t'} = \mu_e F_0 \frac{\delta n'(x', t')}{\delta x'} - \frac{n'(x', t')}{\tau'_e} + g_e \quad (4.20)$$

Here, $g_{h(e)}$ is the thermal generation rate of holes (electrons). $p'(x', t')$ and $n'(x', t')$ are thermally generated holes and electrons concentrations. $\mu_{h(e)}$ is the mobility of holes

(electrons) and $\tau'_{h(e)}$ is the lifetime of holes (electrons). F_0 is the applied electric field. Assuming a uniform electric field in the bulk, the thermal generation rate of holes and electrons can be written as [44]

$$g_h = N(E_F)kT\omega_0 e^{-\frac{E_F - E_V - \beta_{pf}\sqrt{F_0}}{kT}} \quad (4.21)$$

$$g_e = N(E_F)kT\omega_0 e^{-\frac{E_C - E_F - \beta_{pf}\sqrt{F_0}}{kT}} \quad (4.22)$$

Here, $N(E_F)$ is the density of states at Fermi energy E_F , $E_{V(C)}$ is the band edge of valence (conduction) band and $\beta_{pf} (= \sqrt{e^3/\pi\epsilon_s})$ is the Poole-Frenkel coefficient. $\omega_0 (= N_V C_t)$ is the attempt to escape frequency, where C_t is the deep trapping capture coefficient.

The solutions of equations (4.19) and (4.20) are given by [44]

$$p'(x') = g_h \tau'_h \left(1 - e^{-\frac{x'}{\mu_h \tau'_h F_0}}\right) \quad (4.23)$$

$$n'(x') = g_e \tau'_e \left(1 - e^{-\frac{x'}{\mu_e \tau'_e F_0}}\right) \quad (4.24)$$

Now, the hole current density is

$$J_{sh} = \frac{e\mu_h F_0}{L} \int_0^L p'(x') dx' \quad (4.25)$$

The electron current density is

$$J_{se} = \frac{e\mu_e F_0}{L} \int_0^L n'(x') dx' \quad (4.26)$$

Hence, the current densities due to the thermal generation of electrons and holes become

$$J_{se(h)} = e\mu_{e(h)} \tau'_{e(h)} F_0 g_{e(h)} \left[1 - \frac{\mu_{e(h)} \tau'_{e(h)} F_0}{L} \left\{1 - e^{-\frac{L}{\mu_{e(h)} \tau'_{e(h)} F_0}}\right\}\right] \quad (4.27)$$

The total dark current density is

$$J_{Dark} = J_{inj} + J_{sh} + J_{se} \quad (4.28)$$

The total photocurrent density is obtained by adding equations (4.11) and (4.28).

$$J_T(t') = j(t') + J_{Dark} \quad (4.29)$$

4.4 Initial Field Distribution in the Presence of Trapped Charge in the Bulk and Accumulated Ion near the Metal/Photoconductor Interface

After the application of a voltage across the photoconductor, the positive and negative ions in the detector move towards the opposite direction and ions accumulate near the metal/photoconductor interfaces and reach equilibrium. The accumulated ion concentration depends on the applied electric field. This phenomenon affects the electric field distribution across the detector. As a result, the electric field induced by the ionic accumulation impacts the distribution and movement of the photogenerated carriers. The accumulated ion-induced electric field, E_{ion} might partially screen applied field $E_{applied}$, hence reducing the number of carriers collected by the electrode. As a result, the charge collection efficiency (CCE) of the detector lessens. Moreover, the trapped charge from earlier exposure can still be in the detector. Furthermore, small doses of X-ray incident on the detector during starting of the X-ray generator, generate free charges. The liberated charge carriers move toward the electrodes after the application of supply voltage V . If one of the charge carriers has much higher mobility than the other, the faster one will move toward the assigned electrode and will not get easily trapped. Hence, the trapped charge concentration will be lower and uniformly distributed in the device. However, the slower one will get easily trapped and the trapping distribution will follow an exponential distribution. Figure 4.6 shows the initial trapped charge distribution in the photoconductor (i.e. $Cs_2AgBiBr_6$) where holes are much faster than electrons. The accumulation of ions near the metal/photoconductor interfaces after the application of bias voltage is also depicted in Figure 4.6.

The initial conditions of trapped electron and hole concentrations for our device are as following [126]:

$$n'_t(x', 0) = N_t \alpha e^{-\alpha x'} \quad (4.30)$$

$$p'_t(x', 0) = \frac{N_t \theta}{L} \quad (4.31)$$

Here, N_t is the trapped charge carrier per unit area of the detector, and θ is the ratio of trapped holes to electrons.

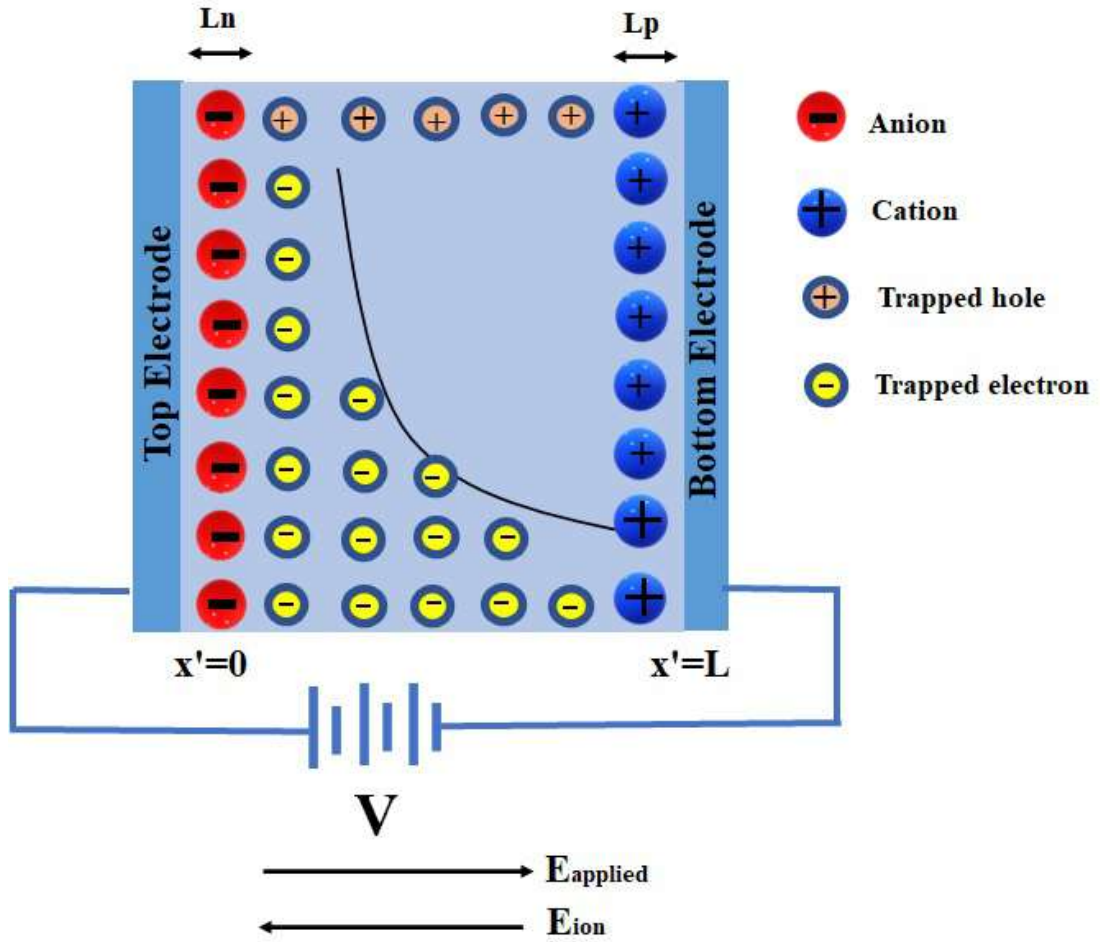


Figure 4.6: Steady-state initial distribution of trapped holes and electrons across the $\text{Cs}_2\text{AgBiBr}_6$ photoconductor and accumulation of ions near the electrode/photoconductor interfaces.

We consider that accumulated anion concentration near the top electrode is N_{acc} and within an accumulation layer thickness of L_n . The cation accumulation layer thickness is L_p which is near the bottom electrode and the accumulated cation concentration is P_{acc} . Now from the top electrode to thickness L_n , trapped charges and anions exist, Hence, in this part of the device considering both trapped charge and ion accumulation, Poisson's equation becomes,

$$\nabla^2 \phi'(x', 0) = \frac{eN_{acc}}{\epsilon} + \frac{eN_t}{\epsilon} (\alpha e^{-\alpha x'} - \frac{\theta}{L}) \quad (4.32)$$

The solution of Poisson's equation gives the potential distribution for $0 \leq x' \leq L_n$ which is

$$\phi'(x', 0) = \frac{eN_{acc}x'^2}{2\epsilon} + \frac{eN_t}{\alpha\epsilon} (e^{-\alpha x'} - \frac{\theta\alpha x'^2}{2L}) + C_1x' + C_2 \quad (4.33)$$

Here, C_1 and C_2 are constants of integration. The negative gradient of the potential is the electric field, so the electric field distribution along the device thickness in the region $0 \leq x' \leq L_n$ is

$$F'(x', 0) = -\frac{eN_{acc}x'}{\epsilon} + \frac{eN_t}{\epsilon}(e^{-\alpha x'} + \frac{\theta x'}{L}) - C_1 \quad (4.34)$$

Between the two ion accumulation layers, in the photoconductor, only trapped charges affect the electric field. Applying Poisson's equation in the region $L_n \leq x' \leq L - L_p$ we get

$$\nabla^2 \phi'(x', 0) = \frac{eN_t}{\epsilon}(\alpha e^{-\alpha x'} - \frac{\theta}{L}) \quad (4.35)$$

The potential distribution obtained from equation (4.35) is

$$\phi'(x', 0) = \frac{eN_t}{\alpha\epsilon}(e^{-\alpha x'} - \frac{\theta\alpha x'^2}{2L}) + C_3x' + C_4 \quad (4.36)$$

Here, C_3 and C_4 are integral constants.

The negative derivative of potential gives the electric field in the region $L_n \leq x' \leq L - L_p$ which is

$$F'(x', 0) = \frac{eN_t}{\epsilon}(e^{-\alpha x'} + \frac{\theta x'}{L}) - C_3 \quad (4.37)$$

The Poisson's equation in the cation accumulation layer is given by

$$\nabla^2 \phi'(x', 0) = -\frac{eP_{acc}}{\epsilon} + \frac{eN_t}{\epsilon}(\alpha e^{-\alpha x'} - \frac{\theta}{L}) \quad (4.38)$$

The potential distribution at $L - L_p \leq x' \leq L$ is

$$\phi'(x', 0) = -\frac{eP_{acc}x'^2}{2\epsilon} + \frac{eN_t}{\alpha\epsilon}(e^{-\alpha x'} - \frac{\theta\alpha x'^2}{2L}) + C_5x' + C_6 \quad (4.39)$$

Here, C_5 and C_6 are integral constants. The electric field distribution at the cation accumulation layer is

$$F'(x', 0) = \frac{eP_{acc}x'}{\epsilon} + \frac{eN_t}{\epsilon}(e^{-\alpha x'} + \frac{\theta x'}{L}) - C_5 \quad (4.40)$$

The potential $\phi'(0, 0) = V$, hence from equation (4.33) we get

$$C_2 = V - \frac{eN_t}{\alpha\epsilon} \quad (4.41)$$

Now, we apply boundary conditions to determine integral constants $C_1, C_3, C_4, C_5,$ and C_6 . Equating the potential at $x'=L_n$ from equations (4.33) and (4.36) and the electric field from equations (4.34) and (4.37), we get

$$C_4 = C_2 - \frac{eN_{acc}L_n^2}{2\epsilon} \quad (4.42)$$

$$C_3 = C_1 + \frac{eN_{acc}L_n}{\epsilon} \quad (4.43)$$

Equating the potential at $x'=L - L_p$ from equations (4.36) and (4.39) and electric field from equations (4.37) and (4.40) we get

$$C_6 = C_4 - \frac{P_{acc}(L - L_p)^2}{2\epsilon} \quad (4.44)$$

$$C_5 = C_3 + \frac{P_{acc}(L - L_p)}{\epsilon} \quad (4.45)$$

Now, $\phi(L, 0) = 0$, hence from equation (4.39) we get

$$C_5 = \frac{eP_{acc}L}{2\epsilon} - \frac{eN_t}{\alpha\epsilon L} \left(e^{-\alpha L} - \frac{\theta\alpha L}{2} \right) - \frac{C_6}{L} \quad (4.46)$$

Using equations (4.34), (4.37), and (4.40) and replacing values of integration constants $C_1, C_2, C_3, C_4, C_5,$ and C_6 , initial normalized electric field distribution due to the presence of trapped charge and accumulated ions can be determined.

$$\begin{aligned} \frac{F'}{F_0} = F\left(0 \leq x \leq \frac{L_n}{L}, 0\right) &= 1 + \frac{eN_t}{\epsilon F_0} \left(e^{-\frac{x}{\Delta}} + \theta x - \Delta\eta - \frac{\theta}{2} \right) - \frac{eN_{acc}L_n^2}{2\epsilon L F_0} \\ &\quad - \frac{eP_{acc}L_p^2}{2\epsilon L F_0} - \frac{eN_{acc}(xL - L_n)}{\epsilon F_0} \end{aligned} \quad (4.47)$$

$$\begin{aligned} \frac{F'}{F_0} = F\left(\frac{L_n}{L} \leq x \leq \frac{L - L_p}{L}, 0\right) &= 1 + \frac{eN_t}{\epsilon F_0} \left(e^{-\frac{x}{\Delta}} + \theta x - \Delta\eta - \frac{\theta}{2} \right) - \frac{eN_{acc}L_n^2}{2\epsilon L F_0} \\ &\quad - \frac{eP_{acc}L_p^2}{2\epsilon L F_0} \end{aligned} \quad (4.48)$$

$$\begin{aligned} \frac{F'}{F_0} = F\left(\frac{L - L_p}{L} \leq x \leq 1, 0\right) &= 1 + \frac{eN_t}{\epsilon F_0} \left(e^{-\frac{x}{\Delta}} + \theta x - \Delta\eta - \frac{\theta}{2} \right) - \frac{eN_{acc}L_n^2}{2\epsilon L F_0} \\ &\quad - \frac{eP_{acc}L_p^2}{2\epsilon L F_0} + \frac{eP_{acc}}{\epsilon F_0} \{xL - (L - L_p)\} \end{aligned} \quad (4.49)$$

Here, $x(= x'/L)$ is the normalized distance from the top electrode, η is the quantum efficiency, and $\Delta(= 1/\alpha L)$ is the normalized attenuation depth. The presence of space

charge is the reason we get a non-uniform electric field distribution. The electric field distribution has an elevation at the electrodes and a low value in the bulk. The minimum value of the electric field is reached in the region $L_n \leq x' \leq L - L_p$. The accumulation layer thickness L_n and L_p are much smaller than the device thickness, L . Hence, equation (4.48) can be approximated as

$$F\left(\frac{L_n}{L} \leq x \leq \frac{L - L_p}{L}, 0\right) = 1 + \frac{eN_t}{\epsilon F_0} \left(e^{-\frac{x}{\Delta}} + \theta x - \Delta\eta - \frac{\theta}{2} \right) \quad (4.50)$$

The location of the electric field minimum (x_{min}) can be determined by setting the gradient of equation (4.50) to zero.

$$x_{min} = -\Delta \ln(\Delta\theta) \quad (4.51)$$

Putting the value of x_{min} in the equation (4.50), the normalized minimum electric field will be

$$F_{min} = 1 + \frac{eN_t}{\epsilon F_0} \left\{ \Delta\theta - \Delta\theta \ln(\Delta\theta) - \Delta\eta - \frac{\theta}{2} \right\} \quad (4.52)$$

If the trapped charge N_t increases, the elevation of the electric field at the electrodes gets higher and the minimum electric field decreases. The trapped charge for which the electric field collapses is called the critical trapped charge (N_{tc}) that can be obtained from equation (4.52), which is,

$$N_{tc} = \frac{F_0 \epsilon}{e} \left\{ \Delta\theta \ln(\Delta\theta) + \Delta\eta + \frac{\theta}{2} - \Delta\theta \right\}^{-1} \quad (4.53)$$

4.5 Electric Field Distribution in $\text{Cs}_2\text{AgBiBr}_6$

Since most reports on $\text{Cs}_2\text{AgBiBr}_6$ suggested that it is a weakly p-type device [108], we can assume in $\text{Cs}_2\text{AgBiBr}_6$, the mobility-lifetime product of electron is much lower than hole mobility-lifetime product (i.e. $\mu_e \tau'_e \ll \mu_h \tau'_h$). Hence, in the $\text{Cs}_2\text{AgBiBr}_6$ detector, the radiation-receiving electrode is positively biased to obtain higher sensitivity. Since the range of holes is greater than electrons, the faster holes do not get trapped easily, whereas, the slower electrons get trapped easily. As a result, the initial trapped hole distribution is much lower and uniform across the device thickness. The trapped electron distribution is exponentially decaying as X-rays interact with the material exponentially.

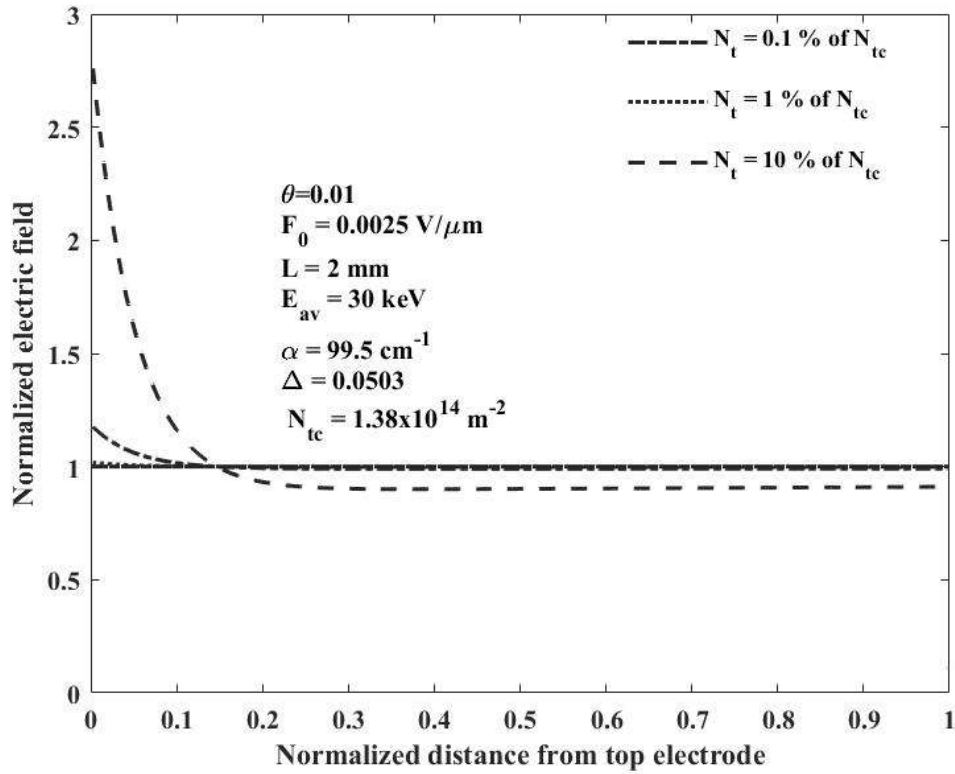


Figure 4.7: Steady-state initial distribution of normalized electric field across the $\text{Cs}_2\text{AgBiBr}_6$ photoconductor in the presence of different initial trapped charges.

A MATLAB code calculates the electric field distribution for the $\text{Au}/\text{Cs}_2\text{AgBiBr}_6/\text{Au}$ X-ray detector. Figure 4.7 shows the effect of the initial trapped charge on the electric field distribution. The relative dielectric constant is 51 for $\text{Cs}_2\text{AgBiBr}_6$. The device thickness has been 2 mm and the applied bias has been 5 V. The X-ray energy is 30 keV [37], and the linear attenuation coefficient is 99.5 cm^{-1} for X-ray energy of 30 keV [118]. The critical trapped charge (N_{tc}) is $1.38 \times 10^{14} \text{ m}^{-2}$. The trapped holes to electrons ratio (θ) has been assumed 0.01. The dashed, dash-dotted, and dotted lines represent the initial trapped charge of 10%, 1%, and 0.1% of critical trapped charge. At the top electrode, the electric field is elevated to 2.8 times of applied electric field, when N_t is 10% of N_{tc} because of high electron trapping. The electric field reaches the minimum in the bulk. For 1% carrier trapping the elevation is ~ 1.18 times, and the electric field in the bulk is close to the applied electric field. For very low carrier trapping (0.1% of N_{tc}), the electric field is essentially uniform and almost equal to the applied electric field. Hence, the effect on electric field distribution can be neglected for low carrier trapping.

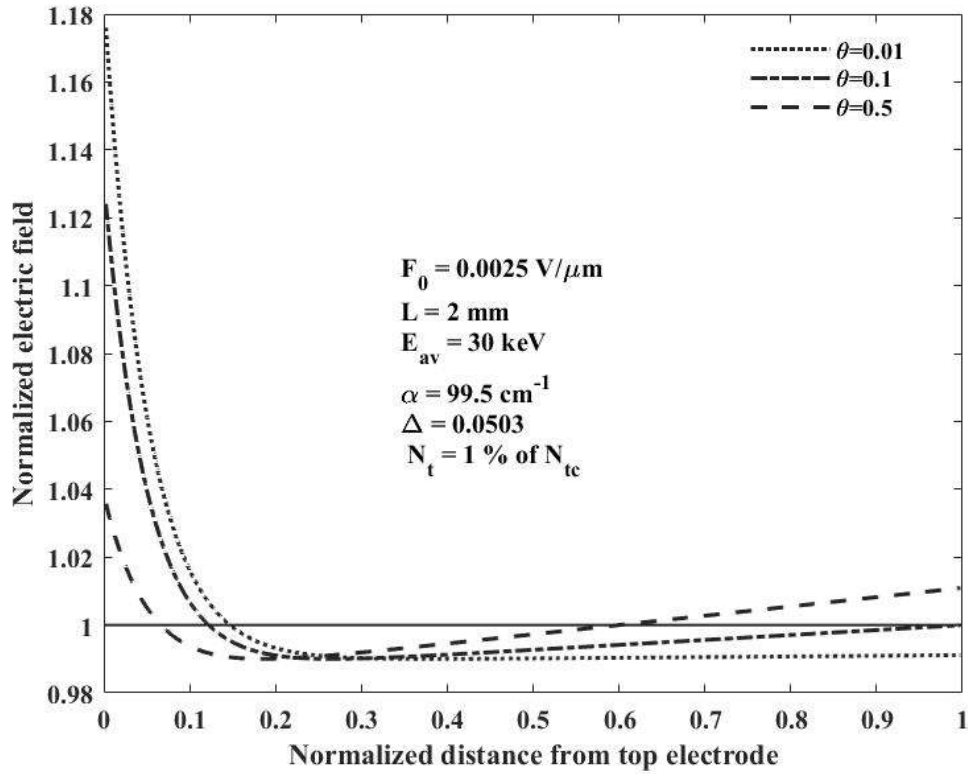


Figure 4.8: Steady-state initial distribution of normalized electric field across the $\text{Cs}_2\text{AgBiBr}_6$ photoconductor in the presence of initial trapped charges for different θ .

The dependence of electric field distribution on trapped holes to electron ratio (θ) is illustrated in Figure 4.8. The trapped charge concentration (N_t) has been assumed 1% of the critical trapped charge (N_{tc}). The dashed, dash-dotted, and dotted lines represent $\theta=0.5$, 0.1, and 0.01, respectively. The increase of θ reduces the electric field elevation at the radiation-receiving electrode. The electric field reaches ~ 1.176 times at the top for $\theta=0.01$, with an almost uniform distribution in the bulk, whereas for $\theta=0.5$, the elevation is 1.035 times with a non-uniform distribution in the bulk.

In Figure 4.9, the normalized electric field distribution across the photoconductor is shown considering the ion accumulations near the electrode/photoconductor interfaces for an $\text{Au}/\text{Cs}_2\text{AgBiBr}_6/\text{Au}$ X-ray detector. Positive 5 V is applied to the radiation-receiving electrode for a 2 mm thick device. Hence, the applied electric field is the same as in Figure 4.7. Anions would be concentrated near the top electrode while cations would be concentrated near the bottom electrode, respectively. The ion accumulation thickness has been assumed to be $5 \mu\text{m}$ [127]. It is evident that the initial field is affected by the accumulated ions. Due to the presence of these ions near the interfaces, the electric field elevates at the metal/photoconductor junctions and becomes uniform ($<$ applied electric field) in the bulk of the photoconductor. The elevation of

the electric field is 8.1, 4.54, and 1.71 times the applied electric field for ion accumulation concentration of 1×10^{19} , 5×10^{18} and $1 \times 10^{18} \text{ m}^{-3}$, respectively. The accumulated ion concentration depends on the applied electric field, the dielectric constant of the photoconductor, the defect density of the device, and energy barriers for ion migration. The raised interface electric field due to ion accumulation will influence the injection of charges from the two electrodes and contribute to dark current. However, in the bulk, the electric field is uniform and almost equal to the applied electric field. Therefore, the elevated electric field at the junction does not affect the drift of the free charges.

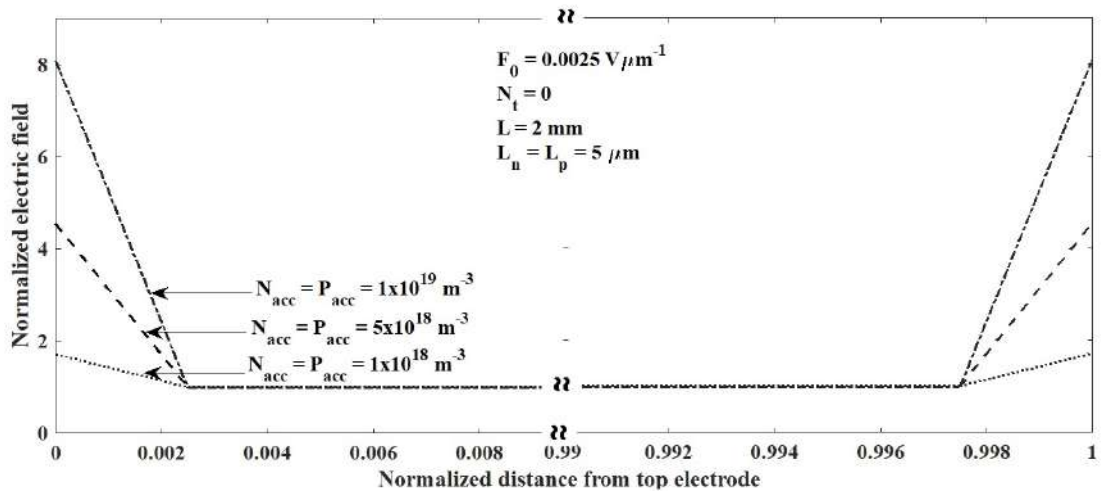


Figure 4.9: Steady-state initial distribution of normalized electric field across the $\text{Cs}_2\text{AgBiBr}_6$ photoconductor in the presence of accumulated ions near the metal/semiconductor interface without any initial trapped charges.

The effect of ion accumulation and trapped charges on the initial electric field distribution is shown in Figure 4.10. The applied electric field is the same as in Figure 4.9. The accumulated ion concentration and accumulation thickness have been assumed 10^{18} m^{-3} and $5 \text{ } \mu\text{m}$, respectively. The critical trapped charge is the same as mentioned in Figure 4.7. The initial carrier trapping has been assumed 0.01% of the critical trapped charge and $\theta = 0.01$. The electric field is raised to ~ 1.71 times the applied electric field at the top and bottom electrodes due to trapped carriers and accumulated ions. In the bulk, the electric field is uniform and slightly less than the applied electric field. The elevated interface electric field will increase the charge carrier injection and hence the dark current of the detector. The charge carrier injection from the electrodes depends on the metal/photoconductor effective barrier height as well.

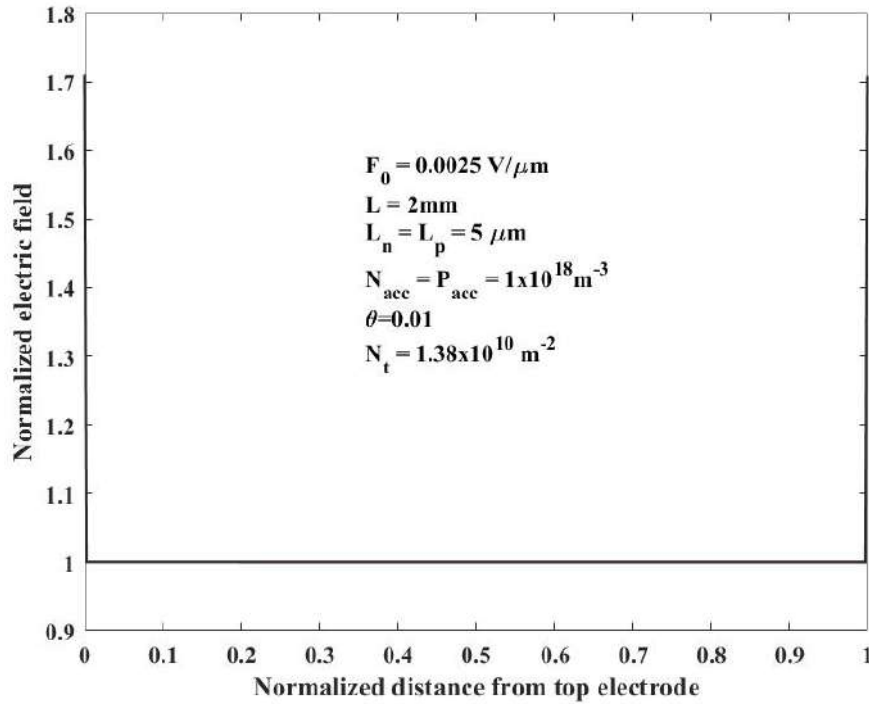


Figure 4.10: Steady-state initial distribution of normalized electric field across the $\text{Cs}_2\text{AgBiBr}_6$ photoconductor in the presence of accumulated ions near the metal/semiconductor interface along with initial trapped charges.

4.6 Photocurrent in $\text{Cs}_2\text{AgBiBr}_6$

Modern X-ray detectors require photoconductors to have excellent sensitivity, good resolution, a large dynamic range, and acceptable dark current. Wide bandgap semiconductors are suitable for X-ray detectors since they ensure negligible dark current in the device, however, wider bandgap also suggests higher ionization energy and lower X-ray sensitivity. Hence, the choice of photoconductors relies on the optimization of these material properties. For our analysis, we have considered $\text{Cs}_2\text{AgBiBr}_6$ photoconductor. MATLAB script is used to calculate photocurrent.

Figure 4.11 shows the steady state photocurrent density as a function of dose rate for a pristine sample of $\text{Cs}_2\text{AgBiBr}_6$ based 2 mm thick direct X-ray detector with Au as an electrode and applied bias of 5 V. The initial trapped charge, ion accumulation layer thickness, and the concentration of accumulated ions are considered to be the same as in Figure 4.10. Therefore, the electric field distribution is considered the same as in Figure 4.10. The symbols and the dotted line in Figure 4.11 represent experimental results [37] and steady-state photocurrent density calculated from equations (4.11), respectively.

The mobility of holes has been considered $3.17 \text{ cm}^2\text{V}^{-1}\text{s}^{-1}$ [37] and lifetime $3 \mu\text{s}$ [125] for the pristine sample. $\text{Cs}_2\text{AgBiBr}_6$ contains easily formed Ag vacancies acting as shallow acceptor defects. Therefore, the electron gets frequently trapped in the shallow traps [113]. Hence the mobility of electrons has been assumed $2 \text{ cm}^2\text{V}^{-1}\text{s}^{-1}$. The lifetime of electrons has been assumed $0.5 \mu\text{s}$. The linear attenuation coefficient is 99.5 cm^{-1} for X-ray energy of 30 keV [118]. The dose rate has been varied up to $141 \mu\text{Gys}^{-1}$ for an exposure time of 5 s . From Figure 4.11 it is evident that there is a photocurrent gain from the theoretical calculation, which is due to the presence of the dark current.

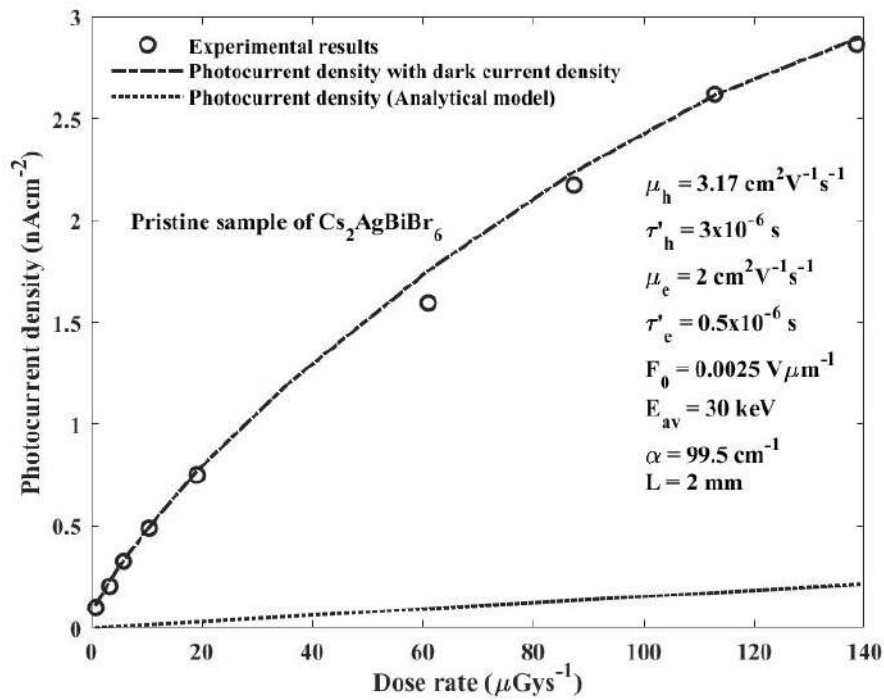


Figure 4.11: Photocurrent density as a function of dose rate for a pristine sample of $\text{Cs}_2\text{AgBiBr}_6$ based direct X-ray detector. Symbols and the dash-dotted line represent experimental results and photocurrent calculated from the analytical model added with the dark current, respectively. The dotted line represents the photocurrent obtained from the analytical model.

The total photocurrent (dash-dotted line) has been calculated by adding the dark current with the theoretical photocurrent (dotted line) to fit the experimental results (symbols) in Figure 4.11. The dark current has been calculated using equation (4.29). The density of states at the valence and conduction bands has been considered $N_V=N_C=2.8\times 10^{24} \text{ m}^{-3}$ [121]. The attempt to escape frequency (ω_0) has been assumed $10^{13}/\text{s}$ [128]. Using the principle of detail balance ($\omega_0 = C_t N_V$), the deep trapping capture coefficient for holes and electrons is found to be $3.6\times 10^{-12} \text{ m}^3/\text{s}$. The integral concentration of deep trap centers for electrons ($N_{te} = 1/C_t\tau'_e$) and holes ($N_{th} = 1/C_t\tau'_h$) are $5.6\times 10^{17} \text{ m}^{-3}$ and

$9 \times 10^{16} \text{ m}^{-3}$, respectively [108]. The effective hole barrier height has been varied from 0.7 eV to 0.616 eV for dose rates up to $141 \mu\text{Gys}^{-1}$ to fit with the experimental data. The reported bandgap of CABB is 1.7 eV to 2.19 eV [38]. Considering a bandgap of 2.19 eV, the theoretical barrier height for injecting holes is 0.73 eV, hence the fitted effective barrier height is within the expected range. The hole injection current density varies from 0.1 to 2.68 nAcm^{-2} with dose rate. The electron barrier height is much higher, hence electron injection is insignificant. The bulk thermal generation current density is 0.015 pAcm^{-2} , which is negligible to hole injection current density. It is evident from Figure 4.11 that the theoretical photocurrent has a linear dependence on the dose rate. The nonlinearity in the total current versus dose rate curve is due to the change in the effective barrier with the dose rate for injecting holes from the metal electrode to the photoconductor. In the absence of illumination, the barrier height is larger. Under X-ray exposure, the photogenerated carriers get trapped close to the metal/photoconductor interface, which causes band bending, and barrier thickness reduction, and leads to effective barrier height reduction [121]. We can conclude that the difference between theoretical photocurrent and total current represents the photocurrent gain, which is due to the enhanced carrier injection under X-ray illumination.

The current density as a function of dose rate for an annealed sample of $\text{Cs}_2\text{AgBiBr}_6$ with Au as the electrode is shown in Figure 4.12. The symbols and dotted line in Figure 4.12 represent experimental results [37] and photocurrent obtained from the theoretical model, respectively. The mobility of holes has been considered $11.81 \text{ cm}^2\text{V}^{-1}\text{s}^{-1}$ [37] and lifetime is $5.2 \mu\text{s}$ [125] for annealed sample. The mobility of electrons has been assumed to be $6.5 \text{ cm}^2\text{V}^{-1}\text{s}^{-1}$, and the lifetime of electrons is $0.5 \mu\text{s}$. The applied electric field and X-ray energy are the same as in a pristine sample. The variation of dose rate has been the same as the pristine sample as well. It is evident that there is a photocurrent gain, although it is less than the pristine sample. The photocurrent in the annealed sample is much higher than in the pristine sample due to the large mobility-lifetime product in the annealed sample. The hole injection current is added to the theoretical photocurrent, which is represented by the dash-dotted line in Figure 4.12, to fit the experimental results. The effective hole barrier height has been varied from 0.723 eV to 0.649 eV to fit with the experimental results. The hole injection current varies from 0.16 to 2.77 nAcm^{-2} . The bulk thermal generation current density is 0.75 pAcm^{-2} .

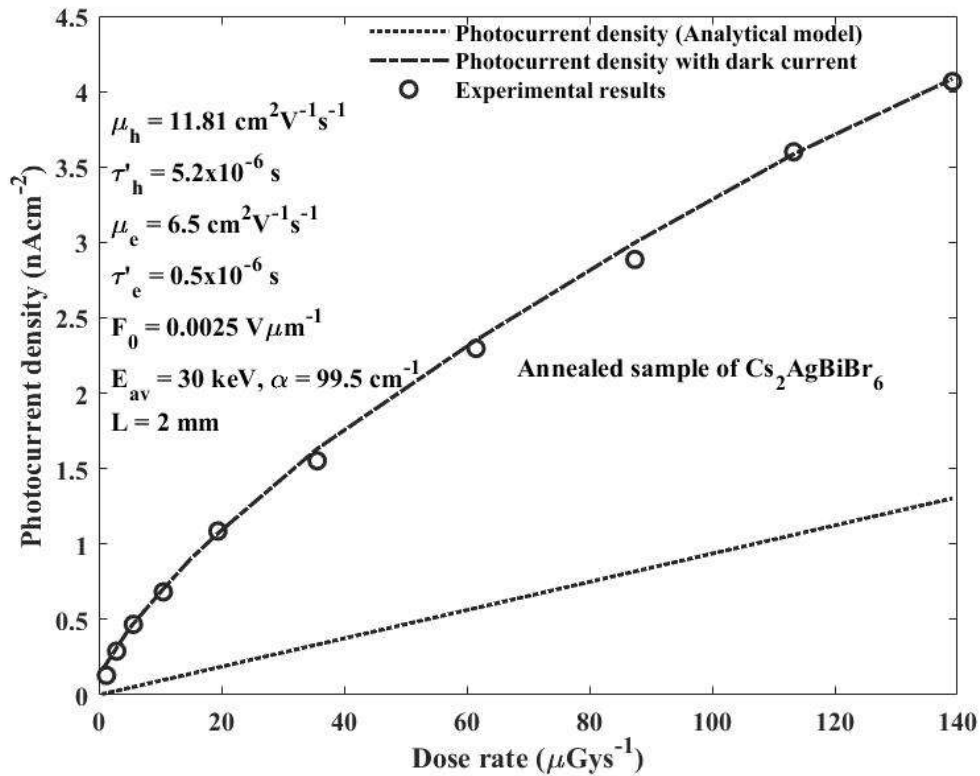


Figure 4.12: Photocurrent density as a function of dose rate for an annealed sample of $\text{Cs}_2\text{AgBiBr}_6$ based direct X-ray detector. Symbols and the dash-dotted line represent experimental results and photocurrent calculated from the analytical model added with the dark current, respectively. The dotted line represents the photocurrent obtained from the analytical model.

Figure 4.13 shows the dark current calculated for both pristine and annealed samples of $\text{Cs}_2\text{AgBiBr}_6$. The dark current reaches almost 2.78 nAcm^{-2} for annealed sample, which is greater than the desirable range ($\sim 1 \text{ nA/cm}^{-2}$) for medical diagnostics. The main source of the high dark current is carrier injection from metal/semiconductor junctions. Inset in Figure 4.13 shows different types of dark current present in the annealed device. It is apparent that the major contribution of dark current comes from the hole injection. The high electron barrier height limits electron injection. Because of the wide absorption edge of $\text{Cs}_2\text{AgBiBr}_6$, the thermal generation current is substantially smaller than the injection current. It is evident from Figure 4.13 that the dark current in the annealed sample is slightly higher than that of the pristine sample although the effective barrier height for hole injection is higher in the former sample. This phenomenon can be attributed to the higher mobility in the annealed sample than that in the pristine sample.

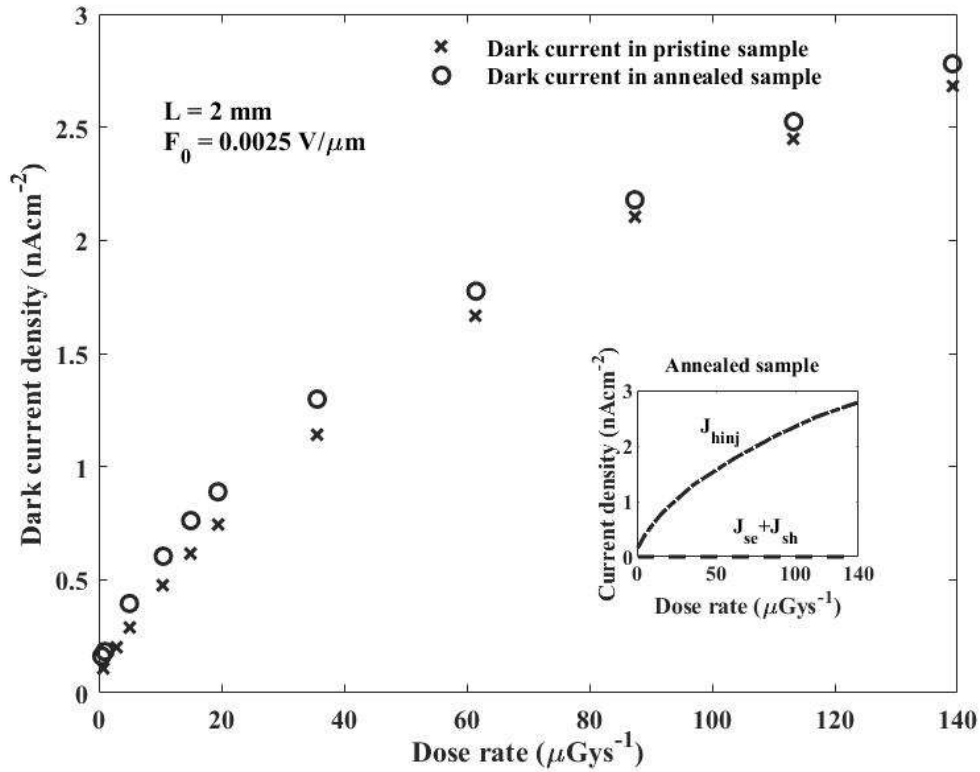


Figure 4.13: Dark current density as a function of dose rate for an annealed and pristine sample of $\text{Cs}_2\text{AgBiBr}_6$ based direct X-ray detector.

The relationship between photocurrent and the applied voltage is shown in Figure 4.14 for various dose rates. The X-ray detector is a 3 mm thick $\text{Cs}_2\text{AgBiBr}_6$ based detector with Ag as electrodes. The Ag/ $\text{Cs}_2\text{AgBiBr}_6$ creates Schottky contact. The applied voltage has been varied up to 18 V. The mobility of holes has been considered to be $6 \text{ cm}^2\text{V}^{-1}\text{s}^{-1}$ and lifetime $3 \mu\text{s}$ [125]. The mobility of electrons has been assumed to be $3 \text{ cm}^2\text{V}^{-1}\text{s}^{-1}$. The lifetime of electrons has been assumed to be $1 \mu\text{s}$. X-ray energy has been 39 keV and the linear attenuation coefficient at 39 keV X-ray is 68 cm^{-1} [118]. The initial trapped charge, accumulation layer thickness, and accumulated ion concentration are the same as in Figure 4.10. hence the initial field distribution is the same as in Figure 4.10. The hole barrier height is greater than 1 eV for Ag/ $\text{Cs}_2\text{AgBiBr}_6$, hence the hole injection is insignificant. The barrier height for injecting electrons from metal to photoconductor is varied from 0.61 eV to 0.584 eV for a dose rate up to $1471 \mu\text{Gys}^{-1}$ for fitting purposes with the experimental results [45]. The theoretical barrier height for electron injection is 0.62 eV. Hence, the fitted effective barrier height is within the expected range. For simplification, the barrier height has been considered to be dependent on dose, and independent of bias voltage. It is evident from Figure 4.14 that the model deviates slightly from the experimental data, specifically at higher voltages,

since the effective barrier height has been assumed to be independent of bias voltage.

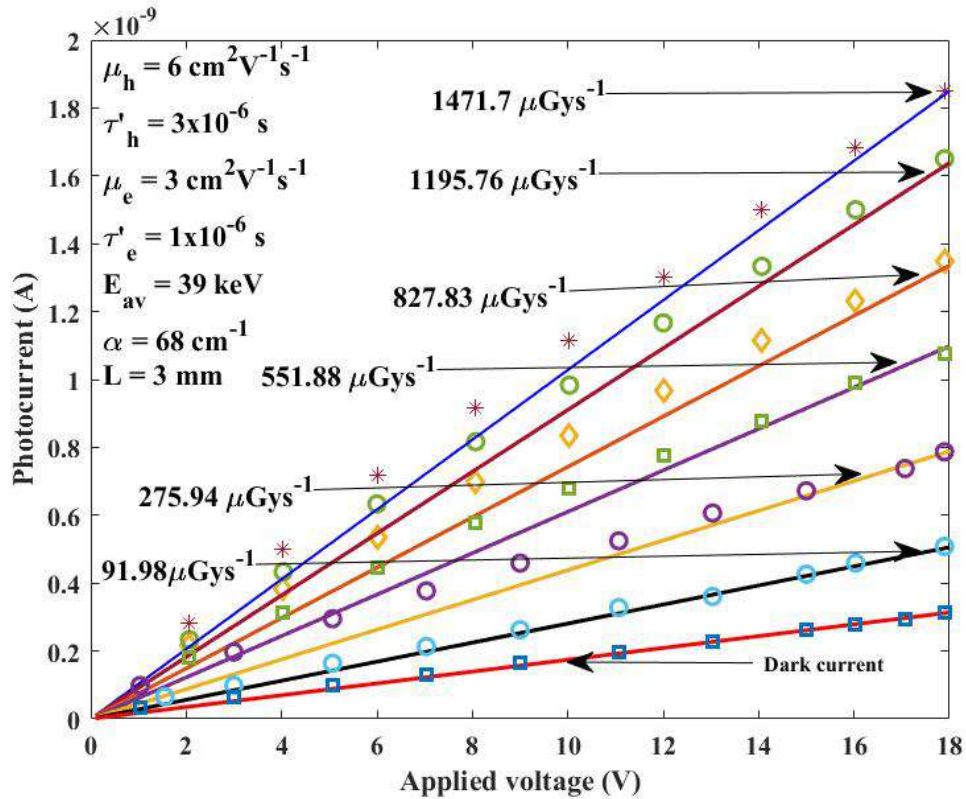


Figure 4.14: Photocurrent as a function of voltage for various dose rates for a $\text{Cs}_2\text{AgBiBr}_6$ based direct X-ray detector. The symbols and the solid line represent experimental results and theoretical model added with dark current, respectively.

4.7 Summary

We have found that the elevated electric field increases by almost an order of magnitude when the ion accumulation concentration is $1 \times 10^{19} \text{ m}^{-3}$. Photocurrent analysis on $\text{Cs}_2\text{AgBiBr}_6$ based X-ray detector reveals that there is a photocurrent gain which is mainly caused by the presence of dark current. The dark current calculated for $\text{Cs}_2\text{AgBiBr}_6$ is greater than the expected range in medical diagnostics [44]. The main contributor to dark current is charge injection from the contacts. Due to the wide band gap, the thermal generation current is significantly less than the injection current. Adding an injection-charge blocking layer might improve the dark current. The ion accumulation near the interfaces raises the junctions' electric field. The charge carrier blocking layers will trap charges. These trapped charges will reduce the elevated electric field at the metal/photoconductor junctions. Thus, the dark current will be reduced.

Chapter 5

Modeling of Sensitivity in X-ray Detector

5.1 Introduction

In a direct conversion X-ray imager, the photoconductor (i.e. $\text{Cs}_2\text{AgBiBr}_6$) is placed between two parallel plate electrodes. Figure 5.1 shows the simplified schematic diagram of a direct conversion X-ray image detector. The electrode is deposited on top and bottom of the photoconductor layer to apply a bias voltage, V to establish a uniform electric field, F_0 along the thickness, L of the photoconductor layer. The applied voltage can be positive or negative based on the $\mu\tau'$ of the slowest carrier [40]. When holes have a longer *schubweg* ($\mu\tau'F_0$) than electrons, the positive bias is recommended so that short-ranged electrons can quickly reach the positive electrode.

Once the top electrode is illuminated by X-rays, the incident X-rays get absorbed in the bulk, and the generation of charge carriers occurs in the photoconductor. The generated charge concentrations follow the exponential X-ray absorption profile. The number of absorbed X-rays and carrier generation depends on the electrical, optical, and geometric properties of the photoconductor materials. The generated charge carriers of opposite polarity drift towards the opposite electrodes due to the presence of the applied electric field and contribute to the induced photocurrent. The drifting charge either reach the electrodes or becomes trapped in the photoconductor. The integration of photocurrent over time gives the collected charge. A current integrator is added externally to integrate the induced photocurrent. The amount of charge collected at the electrodes per unit surface area per unit exposure indicates the sensitivity of the detectors.

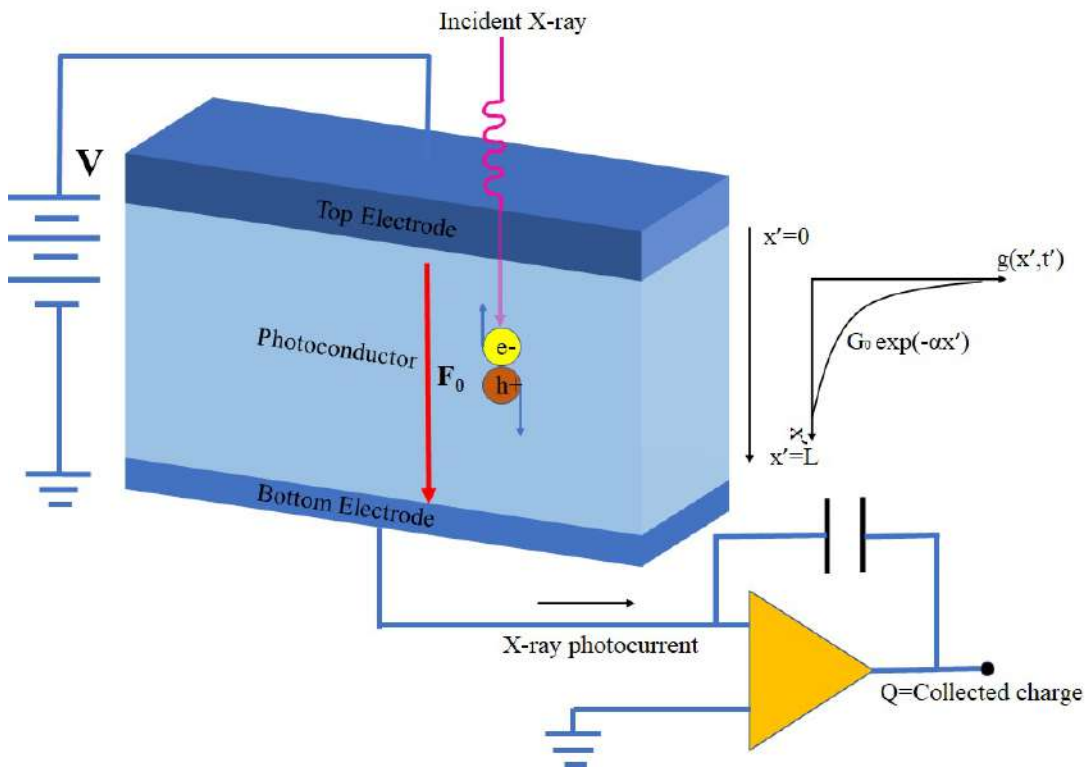


Figure 5.1: A simplified schematic diagram of the structure of an X-ray image detector.

5.2 Numerical Model of Sensitivity

The developed numerical model of sensitivity is based on the basic semiconductor equations: continuity equations for electrons and holes, trapping rate equations for electrons and holes, and Poisson's equation. These equations are solved numerically to obtain free and trapped charge concentrations and electric field distribution in the bulk. The solutions are used to obtain the sensitivity of the detector. The numerical model to determine the sensitivity has been based on the following assumptions:

- 1) Over the complete region of the photoconductor, the material shows uniform properties.
- 2) The thermal equilibrium carrier concentrations are negligibly small.
- 3) The incident X-rays are monoenergetic and are attenuated exponentially ($e^{-\alpha x'}$) along the photoconductor thickness. The generated EHPs concentration follows an exponential profile along the detector thickness from the radiation-receiving electrode.
- 4) Since the generated charge profile is not uniform across the device, the diffusion of carriers is present in the bulk at the low electric field.
- 5) The carrier transport is essentially one-dimensional.

We have denoted $\mu_{h(e)}$ = hole (electron) mobility, $p'(x', t')$ and $n'(x', t')$ are drifting hole and electron concentration in the bulk respectively at position x' , and time t' , $\tau'_{h(e)}$ is hole (electron) lifetime. Also $n'_t(x', t')$ and $p'_t(x', t')$ are trapped electron and hole concentration, respectively at position x' and time t' .

Throughout our work, we have considered the top electrode has been positively biased. The continuity equations for electrons and holes in the photoconductor are thus developed into

$$\begin{aligned} \frac{\delta n'(x', t')}{\delta t'} = \mu_e \frac{\delta(n'(x', t')F'(x', t'))}{\delta x'} + D_e \frac{\delta^2 n'(x', t')}{\delta x'^2} - \frac{n'(x', t')}{\tau'_e} - C_r n'(x', t') p'(x', t') \\ - C_e n'(x', t') p'_t(x', t') + g(x', t') e^{-\alpha x'} \end{aligned} \quad (5.1)$$

$$\begin{aligned} \frac{\delta p'(x', t')}{\delta t'} = -\mu_h \frac{\delta(p'(x', t')F'(x', t'))}{\delta x'} + D_h \frac{\delta^2 p'(x', t')}{\delta x'^2} - \frac{p'(x', t')}{\tau'_h} - C_r p'(x', t') n'(x', t') \\ - C_h p'(x', t') n'_t(x', t') + g(x', t') e^{-\alpha x'} \end{aligned} \quad (5.2)$$

Here, $F'(x', t')$ = electric field at time t' , and position x' considering the space charge in the bulk, α is the linear attenuation coefficient of the photoconductor for X-ray energy E . $g(x', t')$ is electron-hole pair (EHP) generation rate at position x' and time t' . EHP generation rate is assumed to be exponentially decaying towards the non-illuminated electrode since the rate of generation tracks the X-ray absorption profile across the photoconductor thickness. $C_{e(h)}$ is the capture coefficient between trapped electrons (holes) and free holes (electrons). Assuming Langevin recombination mechanism, $C_{e(h)} = \frac{e\mu_{e(h)}}{\epsilon}$ is considered, where e is the elementary charge and $\epsilon (= \epsilon_0 \epsilon_r)$ is the permittivity of the photoconductor. The bimolecular recombination coefficient in semiconductors can be determined using the Langevin model, $C_r = \frac{e(\mu_h + \mu_e)}{\epsilon}$ [129] [130]. The hole diffusion coefficient is $D_h = kT\mu_h/e$ and the electron diffusion coefficient is $D_e = kT\mu_e/e$, where, k is the Boltzmann constant and T is the absolute temperature.

The trapping rate equations for deep trapping are given by

$$\frac{\delta n'_t(x', t')}{\delta t'} = \frac{n'(x', t')}{\tau'_e} - C_h p'(x', t') n'_t(x', t') \quad (5.3)$$

$$\frac{\delta p'_t(x', t')}{\delta t'} = \frac{p'(x', t')}{\tau'_h} - C_e n'(x', t') p'_t(x', t') \quad (5.4)$$

Poisson's equation is used to determine the electric field distribution in the detector

considering the presence of drift charge and trapped charge,

$$\frac{\delta F'(x', t')}{\delta x'} = \frac{e}{\epsilon} [p'(x', t') + p'_t(x', t') - n'(x', t') - n'_t(x', t')] \quad (5.5)$$

The charge carriers are injected into the photoconductor layer. Hence, the initial drifting hole and electron concentrations near the interfaces are the injected charges from the electrodes. The initial trap charge concentrations are taken from equations (4.30) and (4.31). Therefore, the necessary initial and boundary conditions to solve equations (5.1) to (5.5) are

$$\begin{aligned} p'(x', 0) = 0, p'(0, t') = N_v e^{-\frac{\phi_h - \beta_s \sqrt{F_1}}{kT}}, n'(x', 0) = 0, n'(L, t') = N_c e^{-\frac{\phi_e - \beta_s \sqrt{F_2}}{kT}}, \\ p_t(x', 0) = \frac{N_t \theta}{L}, n_t(x', 0) = N_t \alpha e^{-\alpha x'}, \int_0^L F(x', t') dx' = V \end{aligned} \quad (5.6)$$

The semiconductor continuity equations, trapping rate equations, and Poisson's equation given from equations (5.1) to (5.5) are simultaneously solved numerically using the finite difference method. The values of $p'(x', t')$, $n'(x', t')$ and $F(x', t')$ obtained from solving equations are used to calculate photocurrent.

The drift hole photocurrent density is given by

$$j'_h(t') = \frac{(e\mu_h)}{L} \int_0^L F(x', t') p'(x', t') dx' \quad (5.7)$$

The drift electron photocurrent density is given by

$$j'_e(t) = \frac{(e\mu_e)}{L} \int_0^L F(x', t') n'(x', t') dx' \quad (5.8)$$

The diffusion hole photocurrent density is given by

$$j'_{dh} = -eD_h \frac{dp'(x', t')}{dx'} \quad (5.9)$$

The diffusion electron photocurrent density is given by

$$j'_{de} = eD_e \frac{dn'(x', t')}{dx'} \quad (5.10)$$

The total photocurrent density is as follows

$$j'_T(t') = j'_h + j'_e + j'_{dh} + j'_{de} \quad (5.11)$$

The integration of photocurrent over a time period of interest is the collected charge. The total collected charge at time t' is

$$Q = A \int_0^{t'} j_T dt' \quad (5.12)$$

The X-ray sensitivity can be calculated using the collected charge, Q in equation (5.12).

5.3 Expression of Sensitivity in Normalized Coordinates

We used the normalized coordinates for the space and time domain for simplification of the calculation. The space domain was normalized with respect to device thickness L . The normalized distance coordinate is x , where $x = \frac{x'}{L}$. The time coordinate is normalized with respect to the longest transit time. Since electron moves slower in $\text{Cs}_2\text{AgBiBr}_6$, the transit time of electrons $t_e (= \frac{L}{\mu_e F_0})$ is the longest transit time. Therefore, the normalized time t is $\frac{t'}{t_e}$, and normalized carrier lifetimes for electrons and holes are $\tau_e (= \frac{\mu_e \tau'_e F_0}{L})$ and $\tau_h (= \frac{\mu_h \tau'_h F_0}{L})$, respectively. The normalized electric field, $F(x, t)$ is $\frac{F'(x', t')}{F_0}$. The total collectible charge generated in the photoconductor layer per m^3 under a uniform electric field of F_0 with X-ray dose of X (X is in roentgen), is given by

$$p_0 = \frac{1}{L} \int_0^T \int_0^L g_0 e^{-\alpha x'} dx' dt' = \frac{g_0 T \eta}{\alpha L} = \frac{5.45 \times 10^{13} X \eta}{(\frac{\alpha_{air}}{\rho_{air}}) L W_{\pm}} \left(\frac{E_{ab}}{E} \right) \quad (5.13)$$

where, T is the exposure time, η is the quantum efficiency of the detector, E_{ab} is the average absorbed energy per X-ray photon of energy E , W_{\pm} is the EHP creation energy in eV of the photoconductor at an electric field of F_0 and for an incident photon energy of E , α_{air} and ρ_{air} are the energy absorption coefficient and the density of air respectively. p_0 is assumed to be distributed uniformly over the volume of the photoconductor.

Charge carrier concentrations, trapped charge concentrations, and deep trap center concentrations are normalized with respect to p_0 . Equations (5.1)–(5.5) are assumed in the normalized form in equations (5.14) to (5.18).

$$\frac{\delta n}{\delta t} = \frac{\delta(nF)}{\delta x} + r_{de} \frac{\delta^2 n}{\delta x^2} - \frac{n}{\tau_e} - C_R n p - C_0 n p_t + K e^{-\frac{x}{\lambda}} \quad (5.14)$$

$$\frac{\delta p}{\delta t} = -r_\mu \frac{\delta(pF)}{\delta x} + r_{dh} \frac{\delta^2 p}{\delta x^2} - r_\mu \frac{p}{\tau_h} - C_R p n - r_\mu C_0 p n_t + K e^{-\frac{x}{\Delta}} \quad (5.15)$$

$$\frac{\delta n_t}{\delta t} = \frac{n}{\tau_e} - r_\mu C_0 p n_t \quad (5.16)$$

$$\frac{\delta p_t}{\delta t} = r_\mu \frac{p}{\tau_h} - C_0 n p_t \quad (5.17)$$

$$\frac{\delta F}{\delta x} = C_0 (p + p_t - n - n_t) \quad (5.18)$$

Here, $r_\mu = \frac{\mu_h}{\mu_e}$, $r_{de} = \frac{D_e}{\mu_e L F_0}$, $r_{dh} = \frac{D_h}{\mu_e L F_0}$, $C_0 = eq_0 / \epsilon F_0$ ($q_0 = p_0 L$), $C_R = C_0 (1 + r_\mu)$, $n = n' / p_0$, $p = p' / p_0$, $n_t = n'_t / p_0$, $p_t = p'_t / p_0$, and $K = t_e / (T \eta \Delta)$.

The normalized partial differential equations (5.14) to (5.18) are simultaneously solved by the finite difference method (FDM) using MATLAB R2019b. The FDM solution technique is given in Appendix C. To solve the normalized equations, the necessary initial conditions before any exposure are

$$\begin{aligned} p(x, 0) &= 0, n(x, 0) = 0, \\ p_t(x, 0) &= \frac{N_t \theta}{p_0 L}, n_t(x, 0) = \frac{N_t}{p_0} \alpha e^{-\frac{x}{\Delta}} \end{aligned} \quad (5.19)$$

Initial normalized electric field distribution due to the presence of trapped charge and accumulated ions can be determined using Poisson's equation.

The boundary conditions are given by

$$p(0, t) = \frac{N_v}{p_0} e^{-\frac{\phi_h - \beta_s \sqrt{F_1}}{kT}}, n(1, t) = \frac{N_c}{p_0} e^{-\frac{\phi_e - \beta_s \sqrt{F_2}}{kT}}, \int_0^1 F(x, t) dx = 1 \quad (5.20)$$

The normalized drift electron photocurrent density is given by

$$j_e(t) = \int_0^1 F(x, t) n(x, t) dx \quad (5.21)$$

The normalized drift hole photocurrent density is given by

$$j_h(t) = \int_0^1 r_\mu F(x, t) p(x, t) dx \quad (5.22)$$

The normalized electron diffusion photocurrent density is given by

$$j_{de}(t) = \int_0^1 r_{de} \frac{\delta n}{\delta x} dx \quad (5.23)$$

The normalized hole diffusion photocurrent density is given by

$$j_{dh}(t) = - \int_0^1 r_{dh} \frac{\delta p}{\delta x} dx \quad (5.24)$$

The normalized total photocurrent density is given by

$$j_T(t) = j_h(t) + j_e(t) + j_{de}(t) + j_{dh}(t) \quad (5.25)$$

The integration of the total normalized photocurrent density over the normalized time is the normalized collected charge or charge collection efficiency. The product of the normalized collected charge and the quantum efficiency represent the normalized X-ray sensitivity.

$$S_{normalized} = \eta \int_0^1 j_T dt \quad (5.26)$$

The normalized sensitivity calculated from equation (5.26), is multiplied by maximum sensitivity (S_0) to obtain the actual sensitivity of the detector. Maximum sensitivity represents the total collected charge at the electrodes when the incidence radiation is completely absorbed in the material, then converted to EHPs which are all collected at the electrodes. Because it has no discernible impact on the normalized sensitivity, the secondary photon interaction is disregarded when calculating normalized sensitivity.

$$S_0 = \frac{ep_0L/\eta}{X} = \frac{eE\phi_0}{XW_{\pm}} \left(\frac{\alpha_{en}}{\alpha} \right) = \frac{5.45 \times 10^{13}e}{\left(\frac{\alpha_{air}}{\rho_{air}} \right) W_{\pm}} \left(\frac{\alpha_{en}}{\alpha} \right) \quad (5.27)$$

5.4 Summary

The numerical model presented here is applicable to a detector that is positively biased at the radiation-receiving electrode. The model determines sensitivity considering monoenergetic X-rays when the charge generation occurs throughout the detector in the presence of both electron and hole traps and carrier recombination. The sensitivity is a function of the range of charge carriers in the detector, ionization energy, energy of X-rays, and the applied electric field.

Chapter 6

Results and Discussions

6.1 Introduction

The proposed numerical model has been solved simultaneously by FDM using MATLAB R2019b for a $\text{Cs}_2\text{AgBiBr}_6$ based X-ray detector. The drift and trapped charge distribution, electric field distribution, and sensitivity of the photoconductor at the end of transit time have been determined by the proposed model. A MATLAB code in MATLAB R2019b version approximates the numerical solution using the finite difference method. The parameters of the material characteristics (i.e. mobility, the lifetime of carriers, capture coefficient, and trap concentrations) for $\text{Cs}_2\text{AgBiBr}_6$ used in the model are obtained from fitting the analytical model of photocurrent presented in Chapter 4 with the experimental results [37] [45].

We have considered an $\text{Au}/\text{Cs}_2\text{AgBiBr}_6/\text{Au}$ X-ray detector with a 2 mm thick annealed sample of $\text{Cs}_2\text{AgBiBr}_6$ photoconductor [37]. The average X-ray energy of 30 keV [37] has been considered, and at 30 keV, the linear attenuation coefficient of $\text{Cs}_2\text{AgBiBr}_6$ is 99.5 cm^{-1} [118]. The hole mobility of $11.81 \text{ cm}^2\text{V}^{-1}\text{s}^{-1}$ has been assumed for an annealed sample of $\text{Cs}_2\text{AgBiBr}_6$ [37] and hole lifetime of $5.2 \mu\text{s}$ has been considered [125]. The acceptor shallow defects contribute to the intrinsic p-type characteristics of CABB and hence, it is a weakly p-type device [108]. Therefore, the range ($\mu_e\tau_e'$) of the electron is much lower than hole's range ($\mu_h\tau_h'$). The electron mobility of $6.5 \text{ cm}^2\text{V}^{-1}\text{s}^{-1}$ has been assumed. The lifetime of $0.5 \mu\text{s}$ has been assumed for electrons. The X-ray dose of $0.2 \mu\text{Gy}$ has been applied. As the mobility-lifetime product of the hole in $\text{Cs}_2\text{AgBiBr}_6$ is higher than the electron, the top electrode has been considered positively biased in our calculation. The deep trapping capture coefficient, C_t of holes and electrons is $3.6 \times 10^{-12} \text{ m}^3\text{s}^{-1}$ calculated from the attempt to escape frequency dis-

cussed in Chapter 4. The integral concentration of deep hole traps ($N_{th}=1/C_t\tau'_h$) and electron traps ($N_{te}=1/C_t\tau'_e$) traps are $5.4\times 10^{16} \text{ m}^{-3}$ and $5.6\times 10^{17} \text{ m}^{-3}$ [37], respectively. The accumulated ion concentration has been considered 10^{18} m^{-3} with $5 \mu\text{m}$ accumulation layer thickness. The critical trapped charge is $1.38\times 10^{14} \text{ m}^{-2}$ with θ 0.01 and the initial trapped charge has been assumed 0.01% of the critical trapped charge. The bimolecular recombination coefficient has been assumed $C_r=4.5\times 10^{-17} \text{ m}^3\text{s}^{-1}$ [113]. The capture coefficient between free electrons and trapped holes (C_e) and the capture coefficient between free holes and trapped electrons (C_h) have been assumed $4.2\times 10^{-15} \text{ m}^3\text{s}^{-1}$ and $2.3\times 10^{-15} \text{ m}^3\text{s}^{-1}$, respectively, which is two order of magnitude less than the Langevin recombination mechanism [41]. The diffusion coefficients for electrons and holes are $1.67\times 10^{-5} \text{ m}^2\text{s}^{-1}$ and $3\times 10^{-5} \text{ m}^2\text{s}^{-1}$, respectively, calculated from Einstein's relationship. Unless otherwise stated, we have used these parameters throughout our analysis.

6.2 Charge Carrier Distribution and Electric Field Distribution

Figure 6.1 shows the steady-state drift charge (both hole and electron) distribution along the photoconductor thickness for different applied electric fields. The dotted and solid lines represent drift hole distribution for the applied electric field of $1 \text{ V}/\mu\text{m}$ and $0.1 \text{ V}/\mu\text{m}$, respectively. The dash-dotted and dashed lines represent drift electron distribution for the applied electric field of $1 \text{ V}/\mu\text{m}$ and $0.1 \text{ V}/\mu\text{m}$, respectively. The top electrode is positively biased, hence free electrons generated from the absorption of radiation, travel towards the top electrode, and generated holes drift towards the bottom electrode. Therefore, the steady-state drift electron concentration is highest at the photoconductor/top electrode interface and for the hole, the highest concentration is further from the top electrode. The transit time reduces with an increase in the electric field. Hence, at a lower electric field, drift charge concentration is lesser. The drift hole concentration reaches the maximum value of $3.8\times 10^{15} \text{ m}^{-3}$ and $3\times 10^{15} \text{ m}^{-3}$ at 0.4 mm and 0.2 mm , respectively from the radiation-receiving electrode, at electric field $1 \text{ V}/\mu\text{m}$ and $0.1 \text{ V}/\mu\text{m}$, respectively, whereas the drift electron concentration reaches the maximum value of $5.3\times 10^{15} \text{ m}^{-3}$ and $1.8\times 10^{15} \text{ m}^{-3}$, respectively near the top electrode, at electric field $1 \text{ V}/\mu\text{m}$ and $0.1 \text{ V}/\mu\text{m}$, respectively.

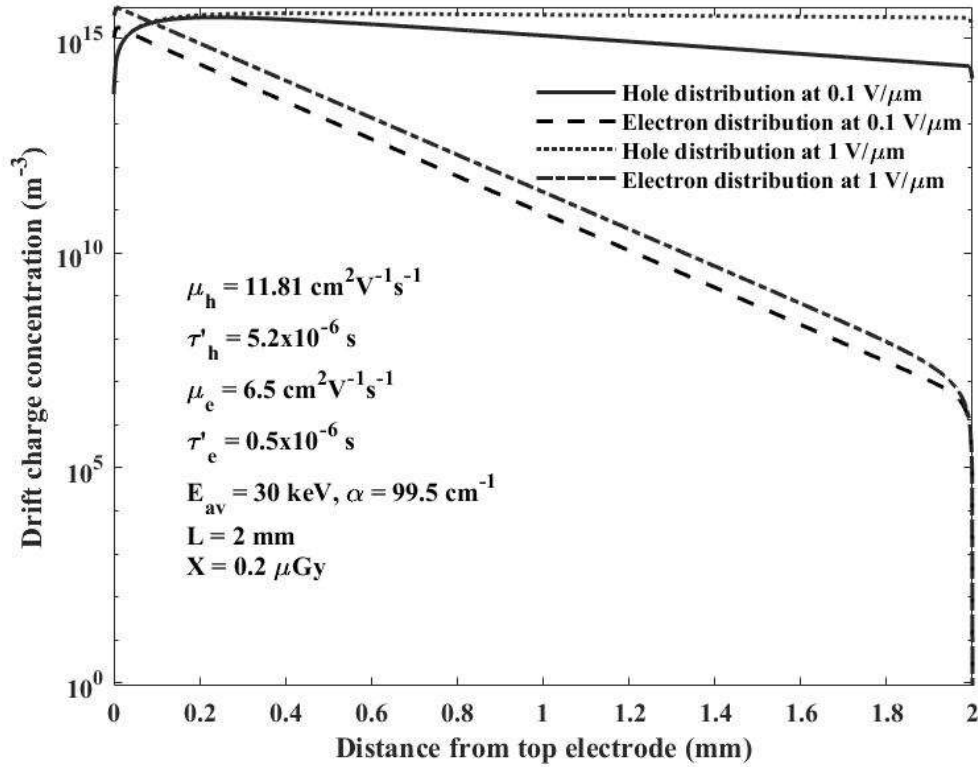


Figure 6.1: Steady-state drift charge distribution along the photoconductor thickness for different applied electric fields.

Figure 6.2 shows the steady-state trapped charge (both hole and electron) distribution along the photoconductor thickness for different applied electric fields. The dotted and solid lines represent trapped hole distribution for the applied electric field of 1 V/ μm and 0.1 V/ μm , respectively. The dash-dotted and dashed lines represent trapped electron distribution for the applied electric field of 1 V/ μm and 0.1 V/ μm , respectively. The carrier trapping increases with the decrease of the applied electric field since carrier transit time increases. A higher electric field lowers the probability of carrier trapping during the traveling of the free carriers. The trapped hole concentration increases from $\sim 2 \times 10^{15} \text{ m}^{-3}$ to $\sim 1.4 \times 10^{16} \text{ m}^{-3}$ for electric field decrease from 1 V/ μm to 0.1 V/ μm . The mobility of electrons in $\text{Cs}_2\text{AgBiBr}_6$ detector is lower than that of holes and trapping time is also lower than holes. Therefore, electrons move slowly resulting in more trapping. The trapped electron distribution follows the exponential interaction profile of the X-rays in $\text{Cs}_2\text{AgBiBr}_6$. The trapped electron concentration near the top electrode increases from $\sim 8 \times 10^{16} \text{ m}^{-3}$ to $\sim 1 \times 10^{17} \text{ m}^{-3}$ for electric field decrease from 1 V/ μm to 0.1 V/ μm .

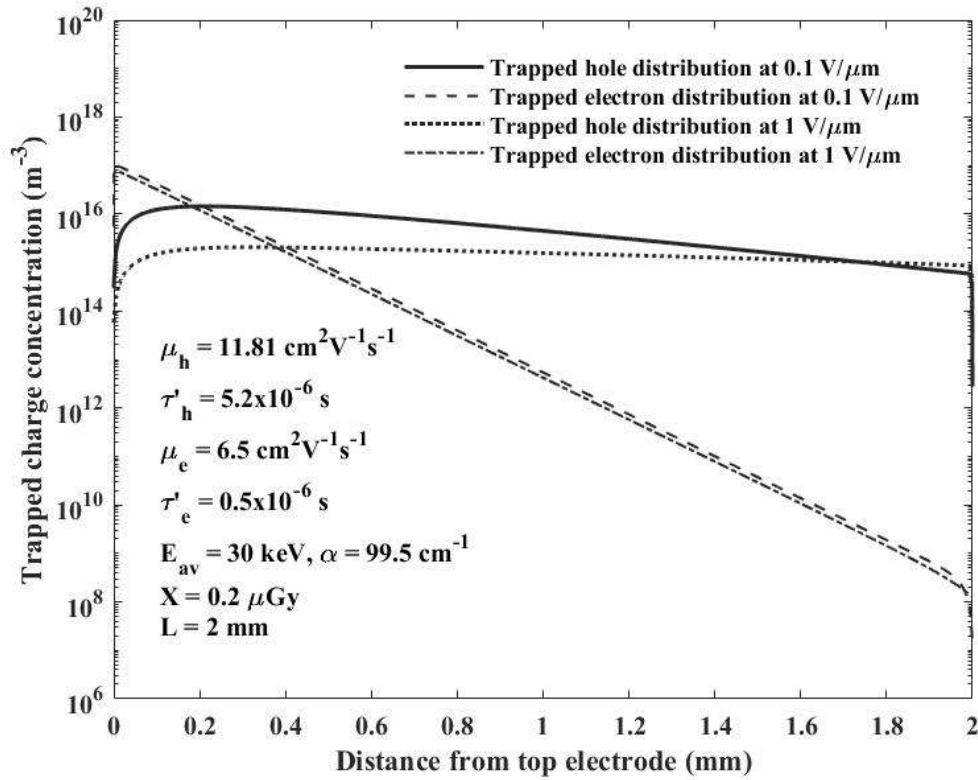


Figure 6.2: Steady-state trapped charge distribution along the photoconductor thickness for different applied electric fields.

Figure 6.3 illustrates the steady-state electric field distribution in the presence of space charge. The solid line represents uniform electric field distribution in the device in the absence of space charges. The dash-dotted and dotted lines represent the normalized electric field distribution for the applied electric field of $1 \text{ V}/\mu\text{m}$ and $0.1 \text{ V}/\mu\text{m}$, respectively. Near the electrodes, accumulated ions, trapped charges, and drift charges perturb the applied electric field, and the electric field is elevated to ~ 1.77 times the applied electric field. The electric field across the photoconductor is affected by the drift and trapped charges, and the electric field decreases below the applied electric field in the bulk of the photoconductor. The lowest point of the distributed field is 0.975 times the applied electric field for $0.1 \text{ V}/\mu\text{m}$, due to the presence of high trapped charge concentration. However, for $1 \text{ V}/\mu\text{m}$, transit time is reduced and the trapped charge concentration is much lower, yielding a nearly uniform electric field in the device.

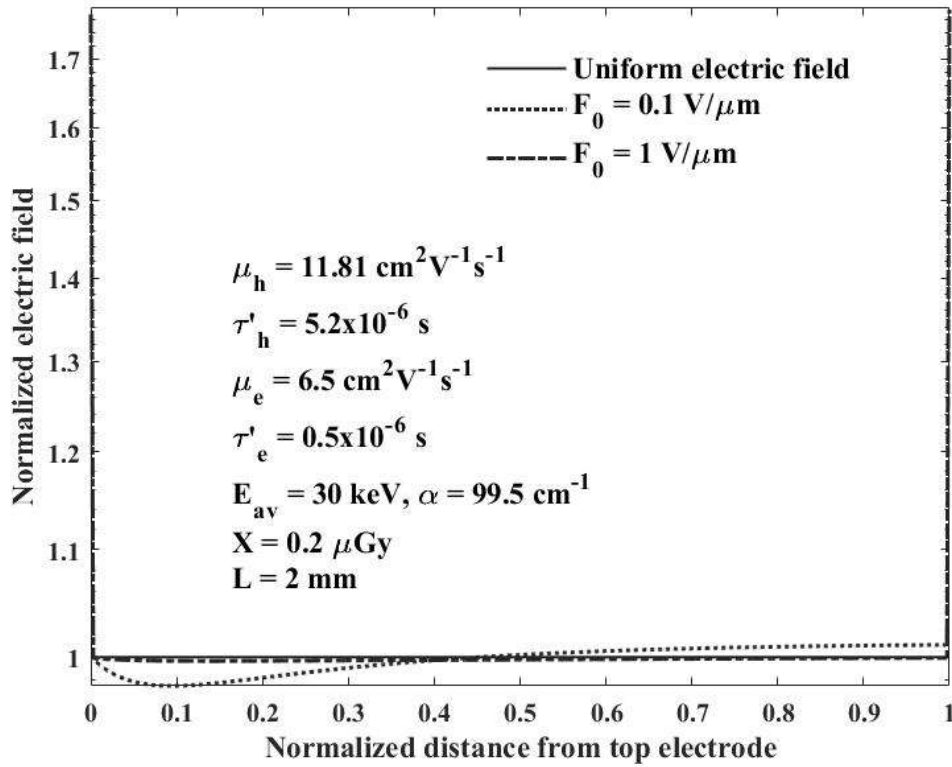


Figure 6.3: The steady-state normalized electric field distribution across the $\text{Cs}_2\text{AgBiBr}_6$ photoconductor in the presence of accumulated ions near the metal/semiconductor interfaces along with drift and trapped charges in the bulk for different applied electric fields.

6.3 Effect of Applied Electric Field on Sensitivity

Figure 6.4 shows the effect of charge diffusion and carrier recombination on sensitivity for small applied electric fields. The applied electric field has been varied up to $0.1 \text{ V}/\mu\text{m}^{-1}$. The dotted line represents sensitivity determined from the numerical model assuming the presence of carrier diffusion and recombination. The dashed line represents sensitivity determined from the numerical model ignoring carrier diffusion. For smaller applied electric fields, the effect of diffusion and recombination of charge carriers is visible, although not significant. Hence, for our device diffusion and recombination of charges can be ignored.

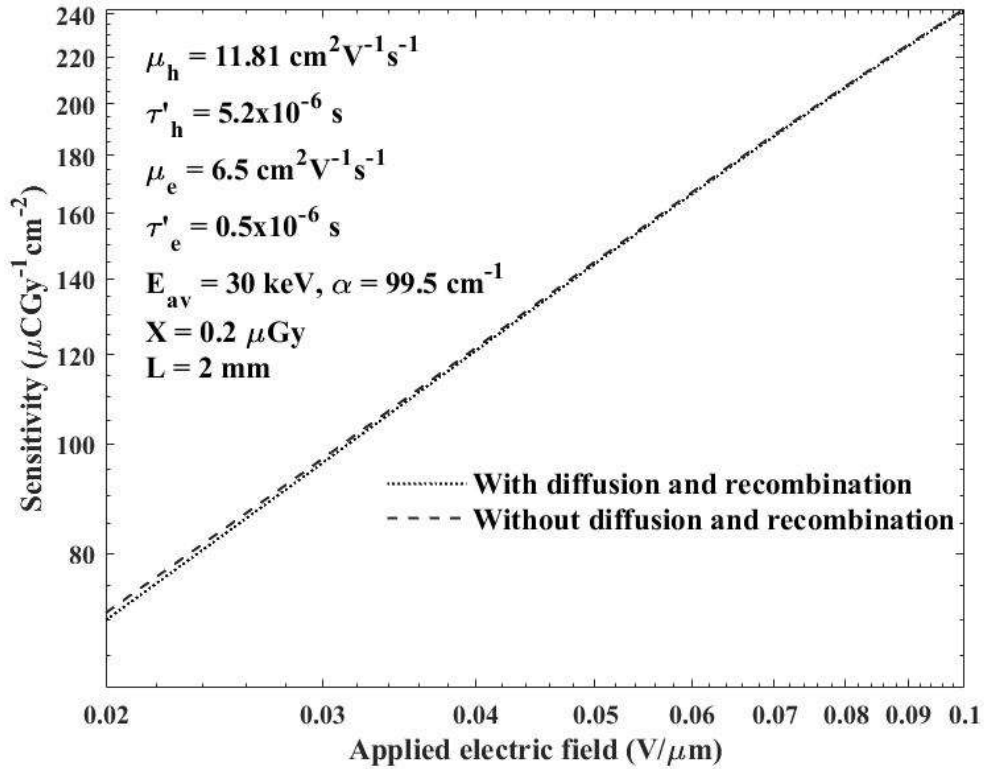


Figure 6.4: Sensitivity dependence on charge diffusion and recombination for different applied electric field for an annealed sample of $\text{Cs}_2\text{AgBiBr}_6$.

The sensitivity calculated from the numerical model for various applied electric fields is shown in Figure 6.5. The applied electric field is varied upto $5 \text{ V}\mu\text{m}^{-1}$. It is apparent that with the increase of the electric field, the sensitivity increases as the drift velocity for free carriers increases. At the low electric fields, sensitivity increases with the applied electric field, since the transit time decreases with field increment and the probability of charge trapping decreases. However, the increment rate decreases at a larger electric field. The collected charge saturates at a large electric field, hence sensitivity tends to saturate at a larger electric field. In Figure 6.5, the solid line represents the sensitivity calculated ignoring ion accumulation and charge injection from the electrodes. The dash-dotted line represents sensitivity obtained considering charge injection with ion accumulation. When charge injection is taken into account, the sensitivity at $5 \text{ V}\mu\text{m}^{-1}$ is $\sim 634 \mu\text{CGy}^{-1}\text{cm}^{-2}$, whereas when it is ignored, the value of sensitivity is $\sim 621 \mu\text{CGy}^{-1}\text{cm}^{-2}$, which is 2% lower. The sensitivity assuming carrier injection is higher than when it is ignored because the injected charges add to the total collected charges.

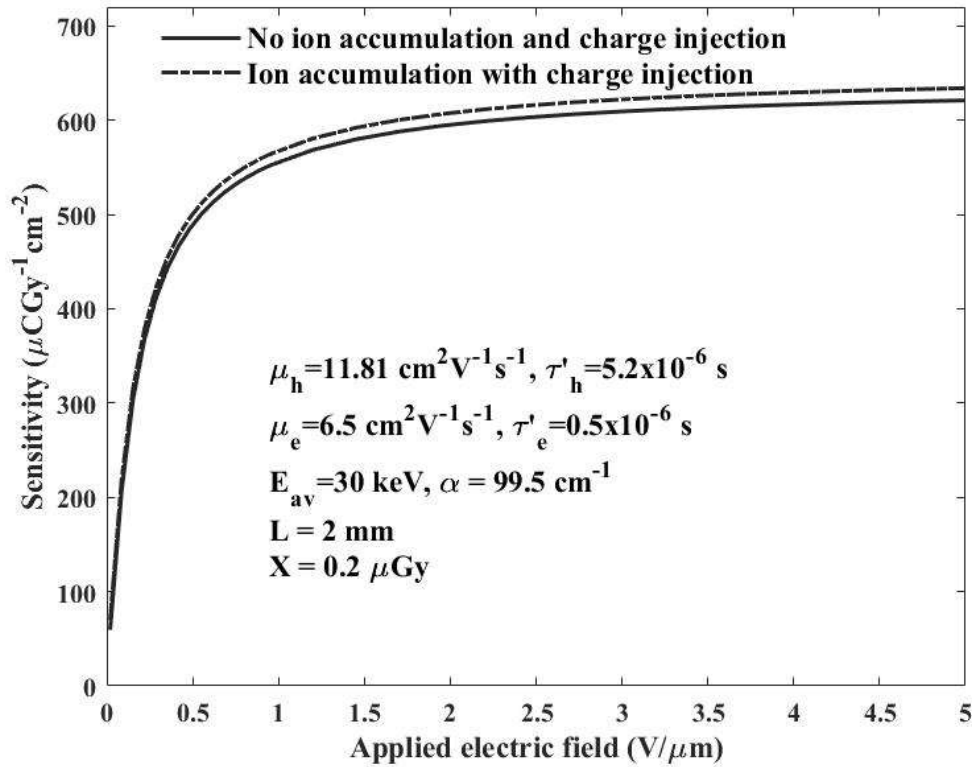


Figure 6.5: Sensitivity for $\text{Cs}_2\text{AgBiBr}_6$ detector for various applied electric fields considering charge injection from the electrodes ($X=0.2\mu\text{Gy}$).

In Figure 6.6, the effect of the applied electric field on sensitivity for a high dose of $5\mu\text{Gy}$ is displayed. The applied field is varied up to $0.1\text{ V}/\mu\text{m}$. The solid line represents the sensitivity calculated ignoring ion accumulation and charge injection from the electrodes. The dash-dotted line represents sensitivity obtained considering charge injection with ion accumulation. It is evident from Figure 6.6 that the difference is not significant when charge injection is considered and ignored for the high X-ray dose. Figures 6.6 (a) and 6.6 (b) show the sensitivity variation when the low electric field (0.03 to $0.04\text{ V}/\mu\text{m}$) is applied and the high electric field is applied (0.08 to $0.1\text{ V}/\mu\text{m}$), respectively. Sensitivity considering charge injection is lower compared to when ignored for the low electric field. The presence of accumulated ions near the electrodes lowers the bulk electric field and it is less than the applied electric field, carrier trapping increases, and overall lowers the charge collection. The elevated interface electric field causes more charge injection from the electrodes, however since the applied electric field is low, the charge injection is insignificant. Hence, overall the charge collection is low for the lower applied electric field. For a highly applied electric field, the charge injection is significant due to the electric field elevation at the interfaces from ion accumulation, and overall the charge collection increases.

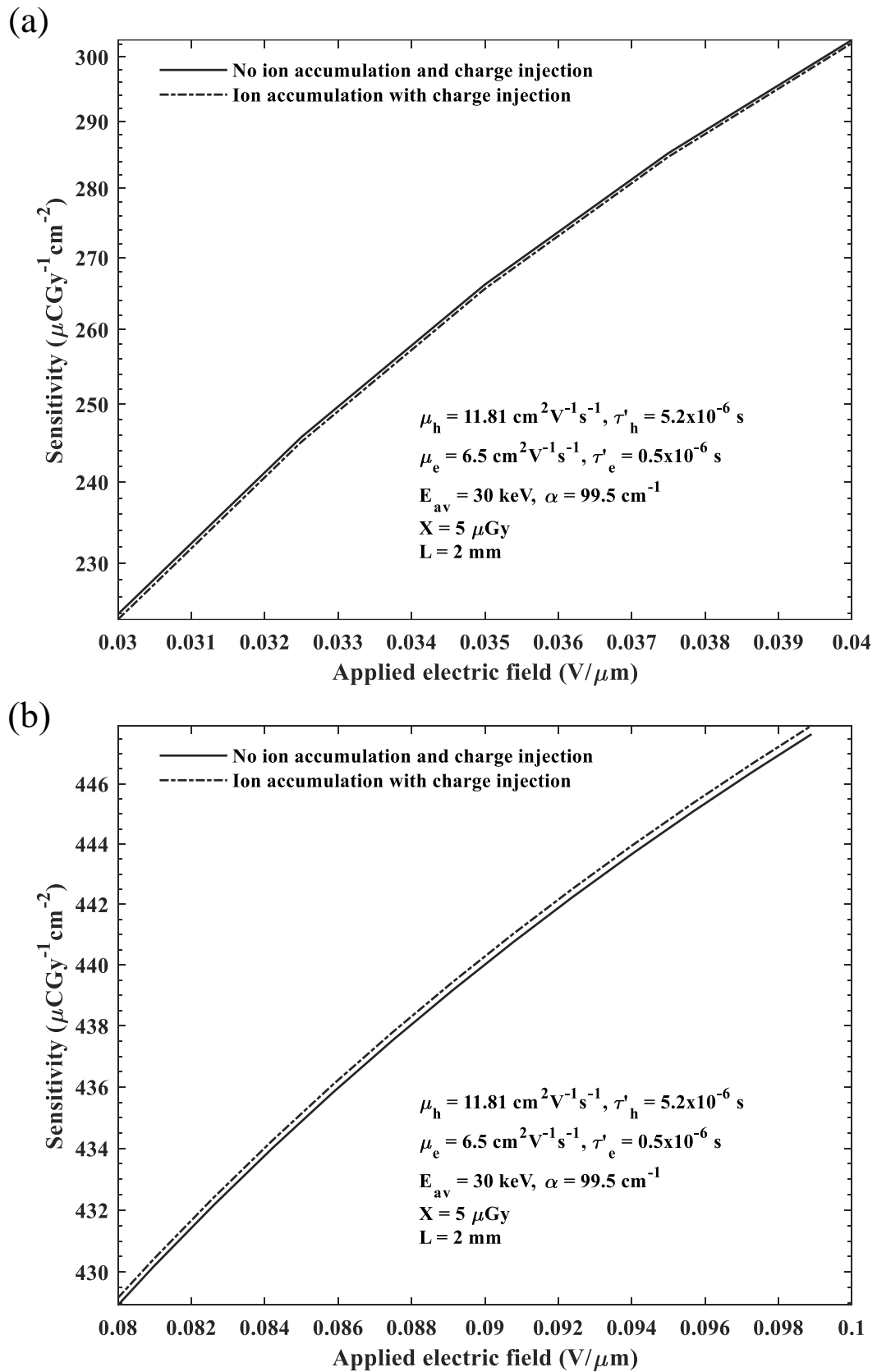


Figure 6.6: Sensitivity for $\text{Cs}_2\text{AgBiBr}_6$ detector for different applied electric fields considering and ignoring charge injection from the electrodes (a) Applied electric field variation 0.03 to 0.04 $\text{V}/\mu\text{m}$ with dose $5\mu\text{Gy}$ and (b) Applied electric field variation 0.08 to 0.1 $\text{V}/\mu\text{m}$ with dose $5\mu\text{Gy}$

6.4 Effect of Charge Carrier Lifetime on Sensitivity

The acceptor shallow defects contribute to the intrinsic p-type characteristics of CABB and hence, it is a weakly p-type device [108]. The hole is the major contributor to the photocurrent. The range ($\mu\tau'$) of holes is higher than electrons. The drift hole distributions across the thickness of the photoconductor for different levels of hole trapping are shown in Figure 6.7. The dashed, dash-dotted, and dotted lines represent the drift hole distribution for $\tau'_h = 1 \mu\text{s}$, $\tau'_h = 10 \mu\text{s}$, and $\tau'_h = 100 \mu\text{s}$, respectively. The electron lifetime has been assumed $0.5 \mu\text{s}$. The applied electric field is $0.1 \text{ V}/\mu\text{m}$. The drift hole concentration decreases with the decrease of τ'_h , since, hole trapping increases. The drift hole concentration does not change significantly for hole trapping time $\tau'_h > 10 \mu\text{s}$. The drift hole concentration reaches $\sim 4 \times 10^{15} \text{ m}^{-3}$ and remains uniform in the bulk for $\tau'_h = 100 \mu\text{s}$.

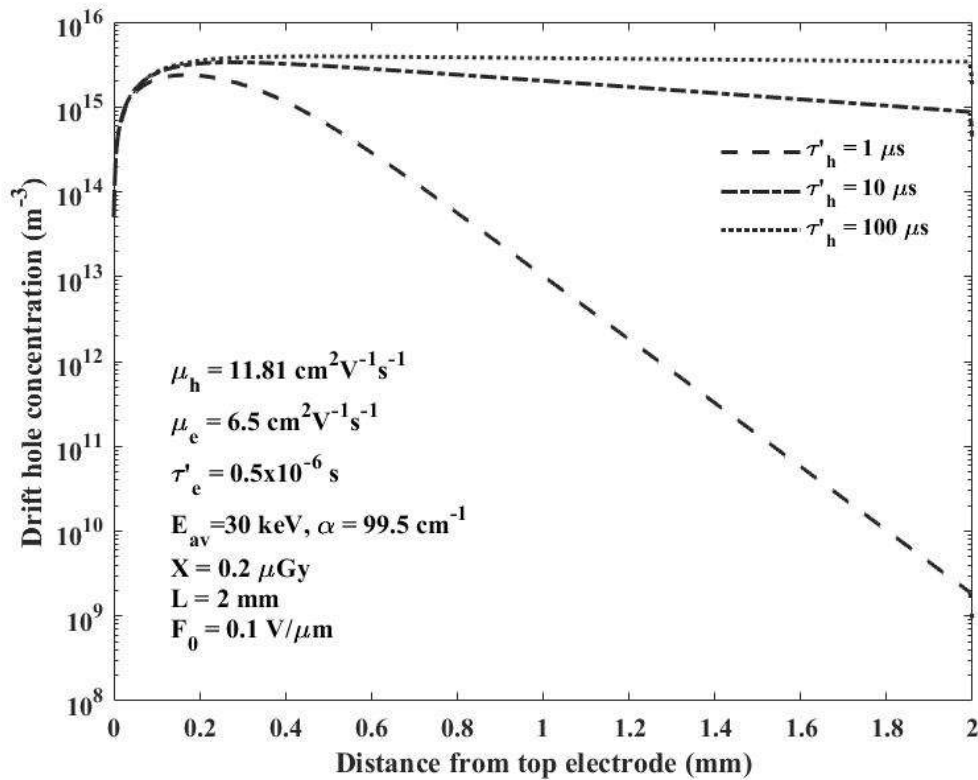


Figure 6.7: Steady-state drift hole distribution in the photoconductor for different hole lifetimes.

The trapped hole distributions across the thickness of the photoconductor for different hole lifetimes are shown in Figure 6.8. The dashed, dash-dotted, and dotted lines represent the trapped hole distribution for $\tau'_h = 1 \mu\text{s}$, $\tau'_h = 10 \mu\text{s}$, and $\tau'_h = \tau'_h = 100 \mu\text{s}$,

respectively in Figure 6.8. The device is the same as mentioned in Figure 6.7. It is evident that the concentration of trapped holes increases with the decrease in hole lifetimes. Since the mobility lifetime product of holes in $\text{Cs}_2\text{AgBiBr}_6$ is high, trapped hole distribution in the bulk is almost uniform, which is especially true for higher lifetimes. Since the hole transit time at $0.1 \text{ V}/\mu\text{m}$ is $\sim 17 \mu\text{s}$, for $\tau'_h = 1 \mu\text{s}$, the trapping mostly occurs near the radiation-receiving electrode, hence trapped hole concentration decreases near the bottom electrode.

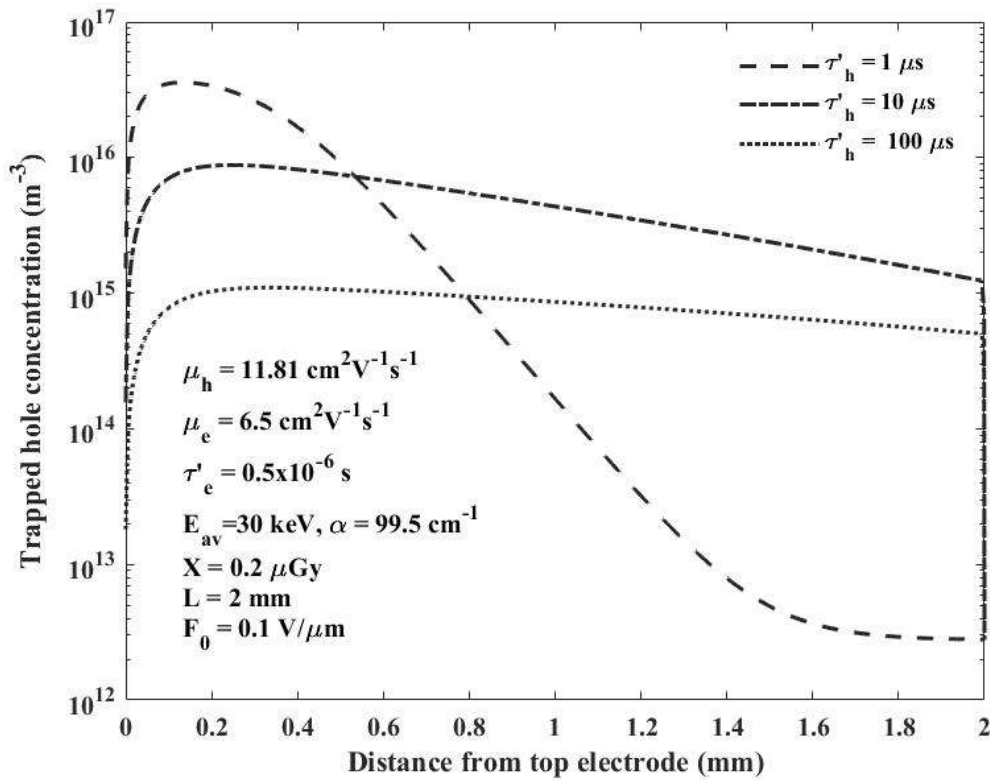


Figure 6.8: Steady-state trapped hole distribution in the photoconductor for different hole lifetimes.

The dependence of sensitivity on the applied electric field for various levels of hole trapping is shown in Figure 6.9. Dashed, dashed-dotted and dotted lines represent sensitivity for various hole lifetimes of $\tau'_h = 1 \mu\text{s}$, $\tau'_h = 10 \mu\text{s}$, and $\tau'_h = 100 \mu\text{s}$, respectively. The electric field has been varied up to $5 \text{ V}/\mu\text{m}^{-1}$ for a 2 mm thick $\text{Cs}_2\text{AgBiBr}_6$ device. The electron lifetime has been assumed $0.5 \mu\text{s}$. With the increase in hole lifetime, hole trapping reduces, and charge collection efficiency increases. Hence, the sensitivity calculated at a larger hole lifetime is higher. At high τ'_h , the probability of holes getting trapped before reaching electrodes diminishes, thus sensitivity reaches saturation at a lower electric field. The sensitivity values with $\tau'_h = 100 \mu\text{s}$ and $\tau'_h = 1 \mu\text{s}$ are 649.5 and $572.5 \mu\text{CGy}^{-1} \text{cm}^{-2}$ respectively for an applied electric field of $5 \text{ V}/\mu\text{m}$, which means

a reduction of the sensitivity by 13.4%. For $\tau'_h = 10\mu\text{s}$, at $5\text{ V}/\mu\text{m}$ sensitivity obtained is $642\ \mu\text{CGy}^{-1}\text{cm}^{-2}$, which is only 1% higher than $\tau'_h = 100\mu\text{s}$. It is apparent that for $\tau'_h \geq 10\ \mu\text{s}$, hole lifetime does not affect the sensitivity much for a high applied electric field.

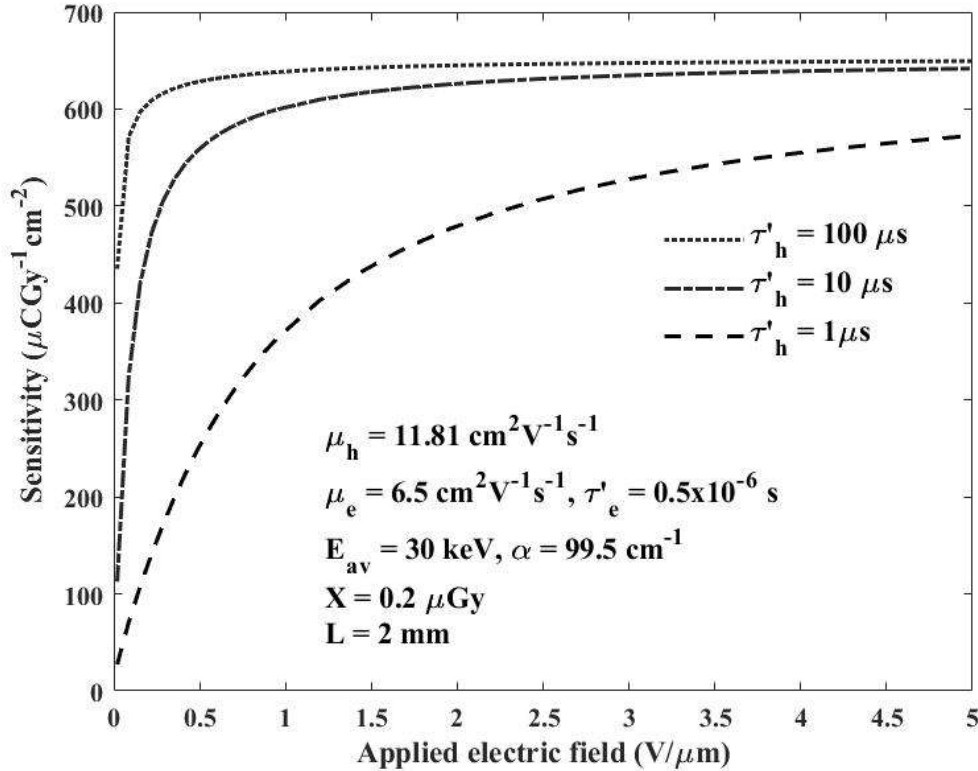


Figure 6.9: Sensitivity as a function of applied electric field for different hole lifetimes.

The drift electron distributions across the thickness of the photoconductor for various levels of electron trapping are shown in Figure 6.10. Dashed, dash-dotted, and dotted lines represent drift electron distribution for various electron lifetimes of $\tau'_e=0.1\ \mu\text{s}$, $\tau'_e=1\ \mu\text{s}$, and $\tau'_e=10\ \mu\text{s}$, respectively for the applied electric field of $0.1\text{ V}/\mu\text{m}$. The hole lifetime is assumed to be $10\ \mu\text{s}$. Since the electron is collected at the radiation-receiving electrode the change in drift electron concentration for different electron lifetimes is low. The trapped electron distributions across the thickness of the photoconductor for different electron lifetimes are shown in Figure 6.11. Dashed, dash-dotted, and dotted lines represent trapped electron distribution for various electron lifetimes of $\tau'_e=0.1\ \mu\text{s}$, $\tau'_e=1\ \mu\text{s}$, and $\tau'_e=10\ \mu\text{s}$, respectively. Electron trapping is much lower for $\tau'_e=10\ \mu\text{s}$ since during transit probability of trapping is reduced. However, the trapped electron concentration does not change much with the lifetime since electrons are collected at the top electrode. It is evident that trapped electron distribution in the bulk follows

exponential distribution following the carrier generation profile.

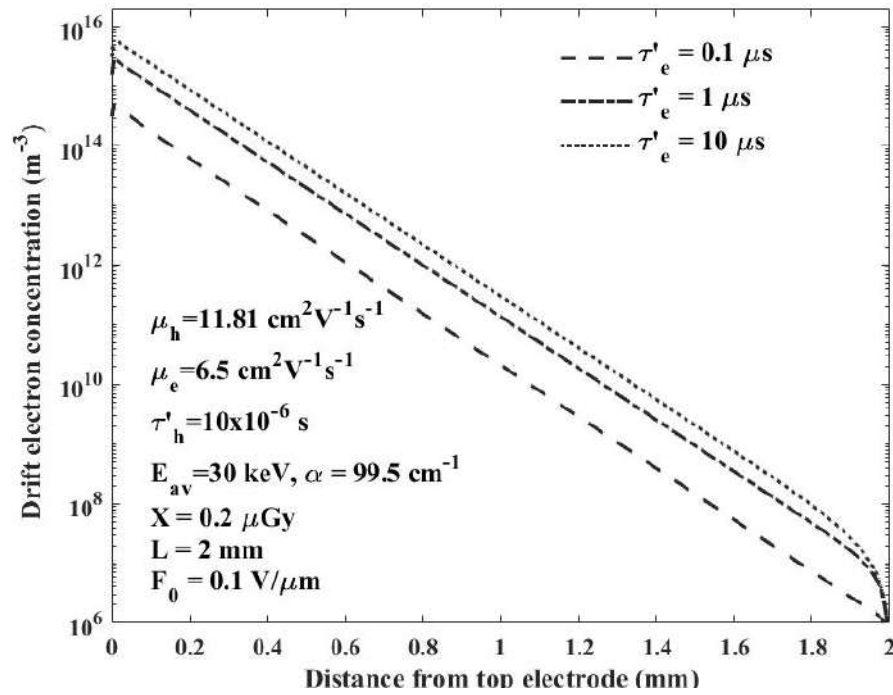


Figure 6.10: Steady-state drift electron distribution in the photoconductor for different electron lifetimes.

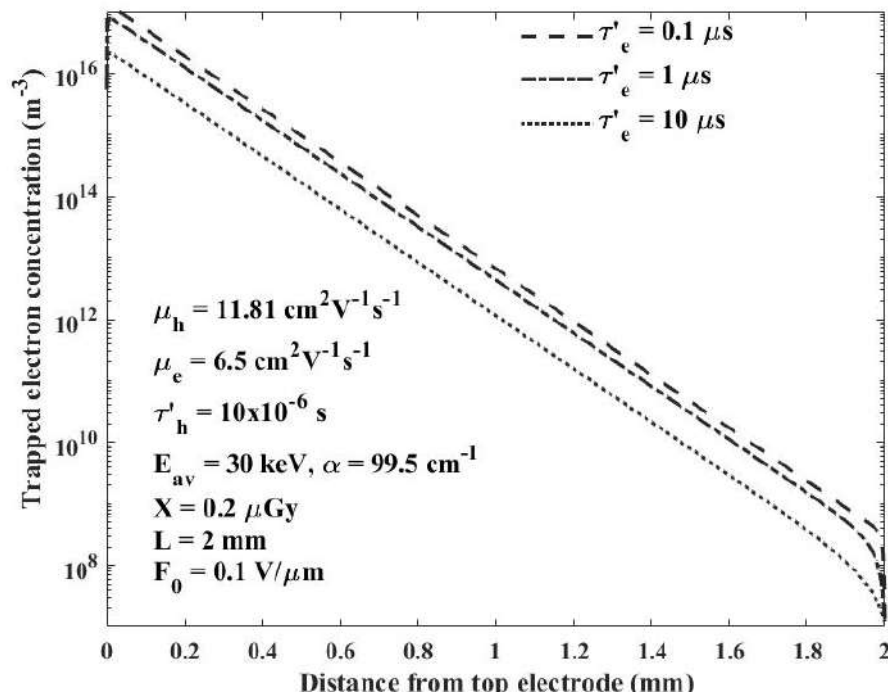


Figure 6.11: Steady-state trapped electron distribution in the photoconductor for different electron lifetimes.

The sensitivity of the photoconductor for different electron lifetimes is shown in Figure 6.12. Dashed, dashed-dotted and dotted lines represent sensitivity for various electron lifetimes of $\tau'_e=0.1 \mu\text{s}$, $\tau'_e=1 \mu\text{s}$, and $\tau'_e=10 \mu\text{s}$, respectively. The electric field has been varied to $5 \text{ V}\mu\text{m}^{-1}$ for a 2 mm thick $\text{Cs}_2\text{AgBiBr}_6$ device. The hole lifetime has been assumed $10\mu\text{s}$. Since, electron trapping increases with the reduction of electron lifetime, the sensitivity reduces as well. However, the effect of electron lifetime variation on sensitivity is not significant. The maximum value of sensitivity of 635, 642.6, and $643.6 \mu\text{CGy}^{-1}\text{cm}^{-2}$ for $\tau'_e = 0.1 \mu\text{s}$, and $\tau'_e = 1 \mu\text{s}$, $\tau'_e = 10 \mu\text{s}$, respectively have been obtained for an applied electric field of $5 \text{ V}/\mu\text{m}$. 1.2% and 0.2% increase in sensitivity for an order change in electron lifetime from $0.1 \mu\text{s}$ to $1 \mu\text{s}$ and from $1 \mu\text{s}$ to $10 \mu\text{s}$, respectively.

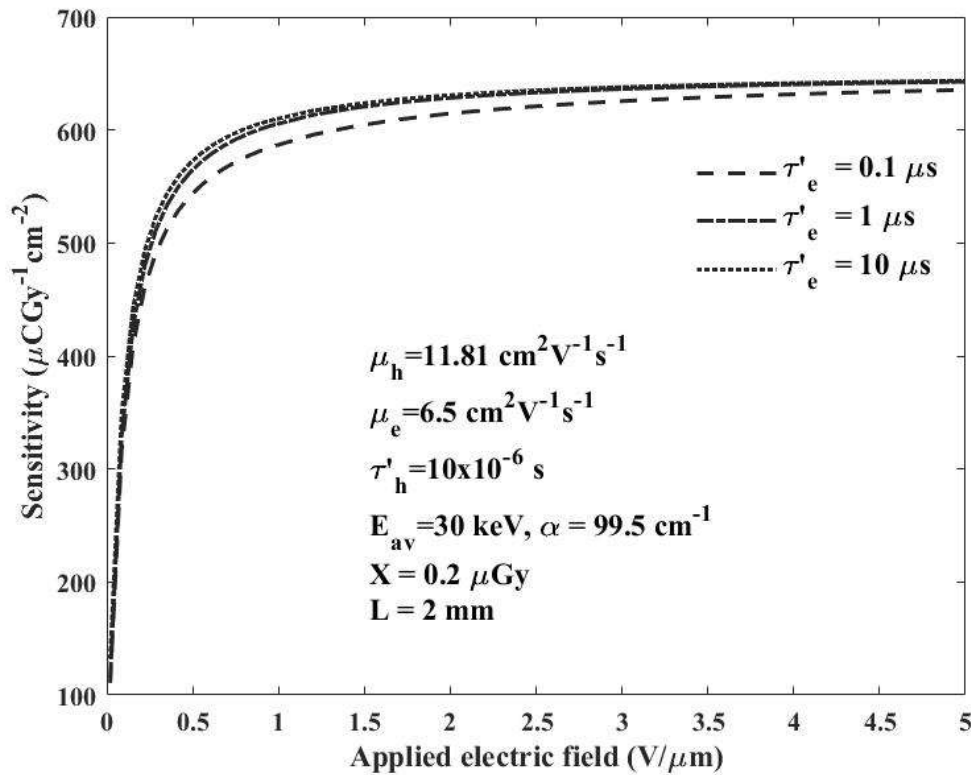


Figure 6.12: Sensitivity as a function of applied electric field for different electron lifetimes.

It is evident from Figure. 6.9 and Figure. 6.12 that the X-ray sensitivity has higher dependence on hole trapping compared to electron trapping. This can be attributable to the fact that the EHPs generation across the photoconductor follows an exponential profile, and the majority of the generation occurs near the radiation-receiving electrode which is positively biased for our photoconductor.

6.5 Effect of Device Thickness on Sensitivity

The device thickness has a significant effect on the sensitivity of the photoconductor. At a lower thickness, the absorption depth is greater than the device's thickness. Therefore, the carrier generation rate is lower, and hence the sensitivity is lower. As the thickness increases, the X-ray absorption increases and the sensitivity also increases. After a certain thickness, the sensitivity increment slows down and reaches the peak. At the maximum point, the device thickness exceeds the absorption depth and the carrier generation rate reaches a maximum level. As the device thickness increases further, the sensitivity starts to decrease. The carrier transit time increases with the device thickness for a certain electric field. If the transit time is comparable with the carrier's lifetime, more carriers will be trapped. Thus, the bulk trapping and recombination rate increases with the device thickness. Hence, the sensitivity decreases for higher device thickness. For a higher electric field, the transit time is lower. Thus the peak sensitivity occurs at a larger device thickness. Since a significant dark current is present for a highly applied field, it is required to optimize the detector thickness to achieve maximum sensitivity within the limit of the applied electric field.

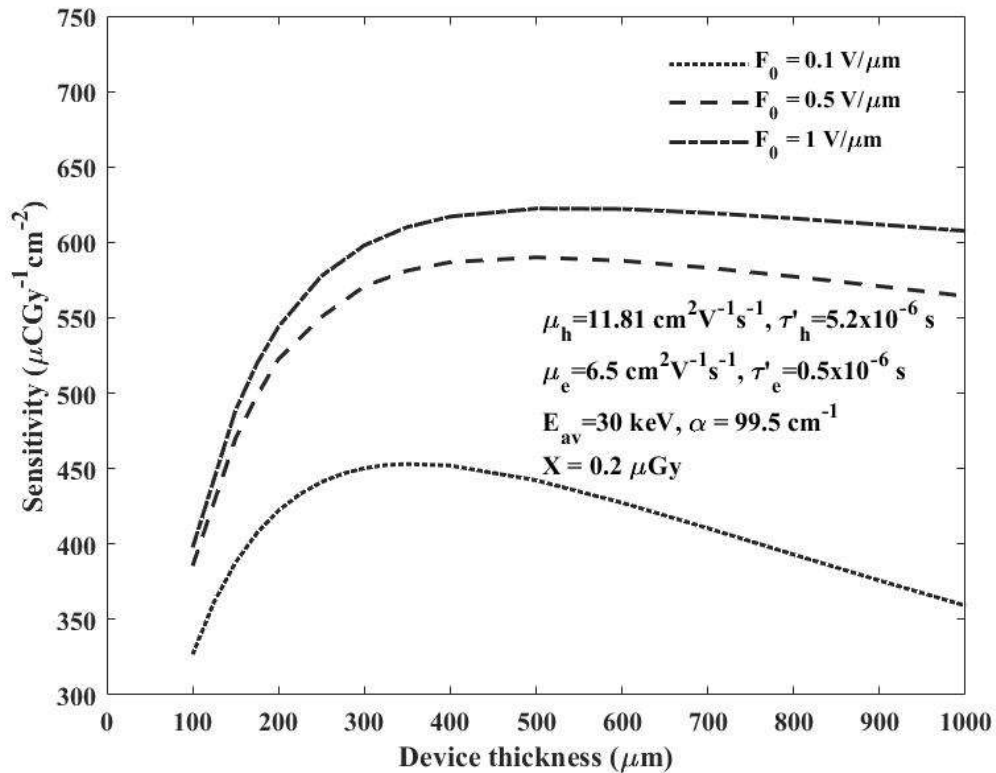


Figure 6.13: Sensitivity as a function of device thickness for different applied electric fields.

The dependence of the sensitivity on the photoconductor thickness for different applied electric fields is shown in Figure 6.13. The optimum photoconductor thickness is $350\mu\text{m}$ and maximum sensitivity is $453\mu\text{CGy}^{-1}\text{cm}^{-2}$ for an applied electric field of $0.1\text{V}\mu\text{m}^{-1}$. The optimum photoconductor thickness increases to $500\mu\text{m}$ and maximum sensitivity reaches to $590\mu\text{CGy}^{-1}\text{cm}^{-2}$ when at $0.5\text{V}\mu\text{m}^{-1}$. For $1\text{V}\mu\text{m}^{-1}$, the optimum photoconductor thickness is $550\mu\text{m}$ and maximum sensitivity is $622.7\mu\text{CGy}^{-1}\text{cm}^{-2}$. The maximum sensitivity increases 30 % and 5.5% for electric field change from 0.1 to 0.5 $\text{V}/\mu\text{m}$ and from 0.5 to 1 $\text{V}/\mu\text{m}$, respectively. For a high electric field, the charge trapping is low, hence sensitivity does not decrease much from the peak value with the increase of photoconductor thickness.

6.6 Effect of X-ray Dose on Sensitivity

We have examined the effects of different dosages of radiation on the distributions of charge carriers and sensitivity for a $\text{Cs}_2\text{AgBiBr}_6$ photoconductor.

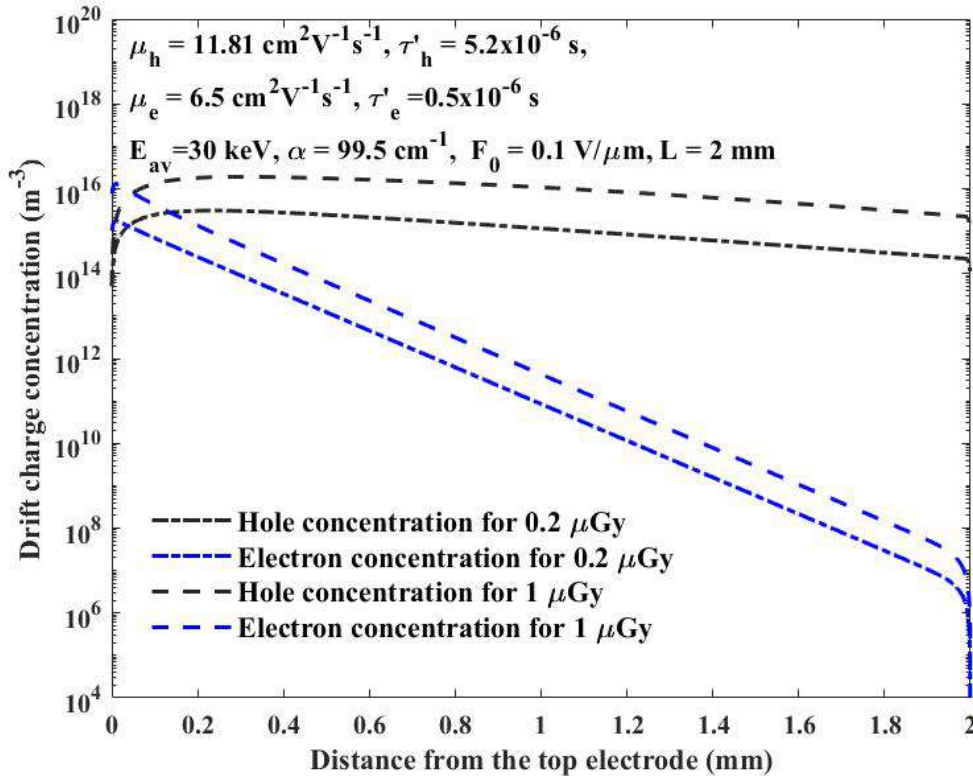


Figure 6.14: Drift charge distributions along the photoconductor thickness for various doses.

The drift charge distribution along the thickness of the photoconductor is illustrated in

Figure 6.14 for various radiation rates. The applied electric field is $0.1 \text{ V}/\mu\text{m}$. Black dashed and dash-dotted lines represent drift hole distributions for $1 \mu\text{Gy}$, and $0.2 \mu\text{Gy}$, respectively. Blue dashed, and dash-dotted lines represent drift electron distributions for $1 \mu\text{Gy}$, and $0.2 \mu\text{Gy}$, respectively. It is evident that the drift charges increase with higher exposure because the generation of free charge carriers increases with the exposure increase. The maximum drift hole concentration increases from 3×10^{15} to $1.9 \times 10^{16} \text{ m}^{-3}$ for dose of 0.2 to $1 \mu\text{Gy}$. The maximum drift electron concentration increases from 1.8×10^{15} to $1.4 \times 10^{16} \text{ m}^{-3}$ for dose of 0.2 to $1 \mu\text{Gy}$.

Figure 6.15 represents the steady-state trapped charge distribution along the photoconductor thickness for different doses. The applied electric field is $0.1 \text{ V}/\mu\text{m}$. Blue dashed, and dash-dotted lines represent trapped electron distributions for $1 \mu\text{Gy}$, and $0.2 \mu\text{Gy}$, respectively. Black dashed, and dash-dotted lines represent trapped hole distributions for $1 \mu\text{Gy}$, and $0.2 \mu\text{Gy}$, respectively. Trapped electron and hole concentration increase with dose. At a much higher dose, generated charge concentration increases, and charge trapping probability increases as a result. The maximum trapped hole concentration increases from 1.4×10^{16} to $4.4 \times 10^{16} \text{ m}^{-3}$ for dose of 0.2 to $1 \mu\text{Gy}$. The maximum trapped electron concentration increases from 1×10^{17} to $3.9 \times 10^{17} \text{ m}^{-3}$ for dose of 0.2 to $1 \mu\text{Gy}$.

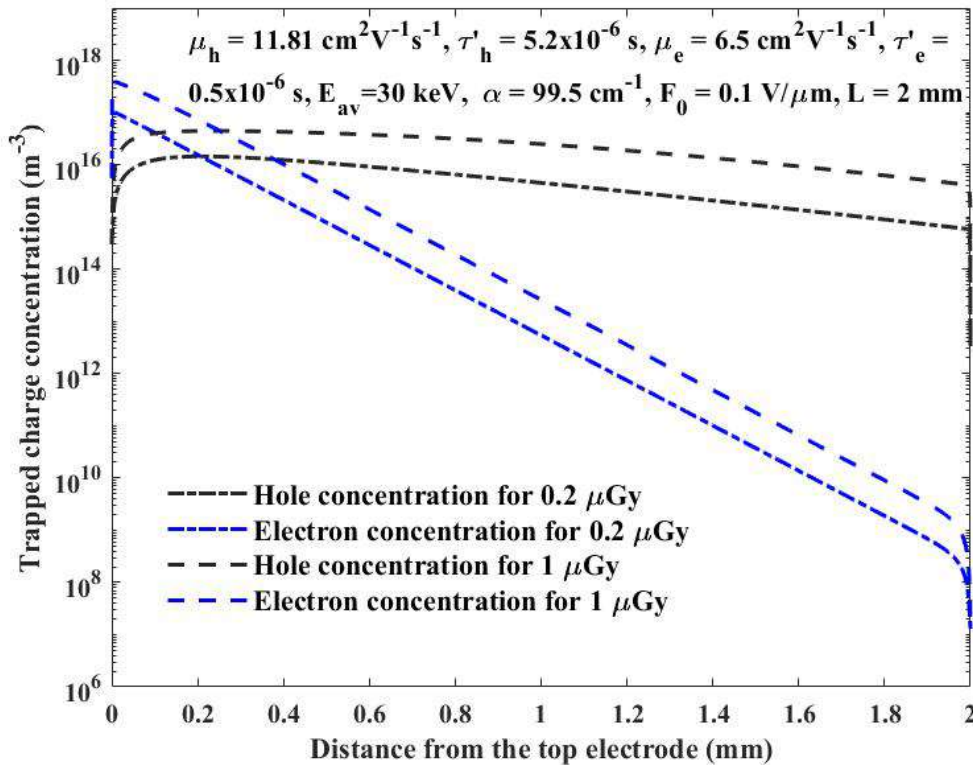


Figure 6.15: Trapped charge distributions along the photoconductor thickness for various doses.

Normalized electric field distribution across photoconductor thickness for various doses is shown in Figure 6.16. The solid line represents uniform electric field distribution in the absence of space charge. The dash-dotted and dashed lines represent electric field distribution for dose $0.2 \mu\text{Gy}$ and $1 \mu\text{Gy}$, respectively. The elevation near the top and bottom electrodes is 1.76 times the applied electric field for $0.2 \mu\text{Gy}$, which is mainly due to the ion accumulation, rather than the drift and trapped charges and the lowest point reaches 0.975 times of applied electric field in the bulk with almost uniform distribution. Since an increase in exposure increases the trapped and drift charges in the detector, the elevation near the top and bottom electrodes are ~ 1.77 and ~ 1.85 times the applied electric field, and the lowest point reaches 0.89 times of applied electric field for $1 \mu\text{Gy}$.

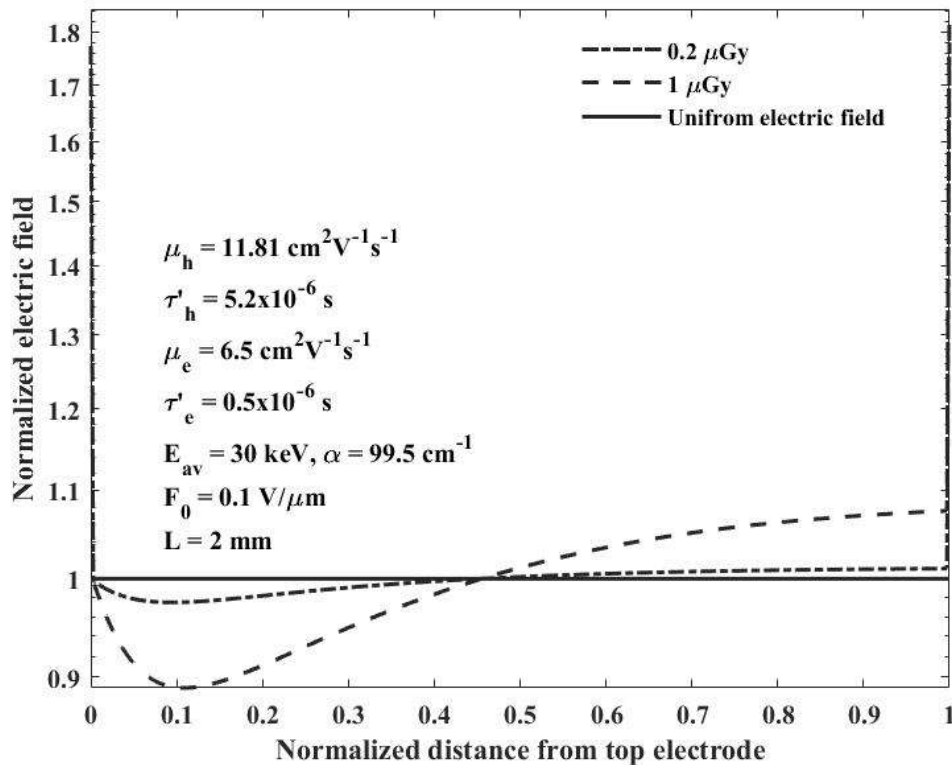


Figure 6.16: Normalized electric field distribution along the photoconductor thickness for various doses.

Figure 6.17 shows the dependence of sensitivity on X-ray dose. The dashed, dash-dotted, and dotted lines show sensitivity for applied electric fields of $1 \text{ V}/\mu\text{m}$, $0.1 \text{ V}/\mu\text{m}$, and $0.05 \text{ V}/\mu\text{m}$, respectively. The dose is varied up to $10 \mu\text{Gy}$. It is apparent that for low applied electric field sensitivity initially increases with the dose. This increase in sensitivity can be attributed to the increase in the generation of charges with dose. Sensitivity declines as the dose is increased further. This can be explained by the rise

in charge trapping and the decrease in charge collection. The maximum sensitivity obtained have been 463 and 359.5 $\mu\text{CGy}^{-1}\text{cm}^{-2}$ for 7 and 4.5 μGy for 0.1 and 0.05 $\text{V}/\mu\text{m}$, respectively. Since the transit time is greater in low electric fields, carrier trapping begins to predominate at a lower dose. Therefore, at a low dosage maximum achievable sensitivity is attained. Sensitivity does not change significantly at a very high electric field because carrier trapping is minimal and charge collection is close to saturation. The sensitivity obtained has been $\sim 580 \mu\text{CGy}^{-1}\text{cm}^{-2}$ for 7 μGy for 1 $\text{V}/\mu\text{m}$.

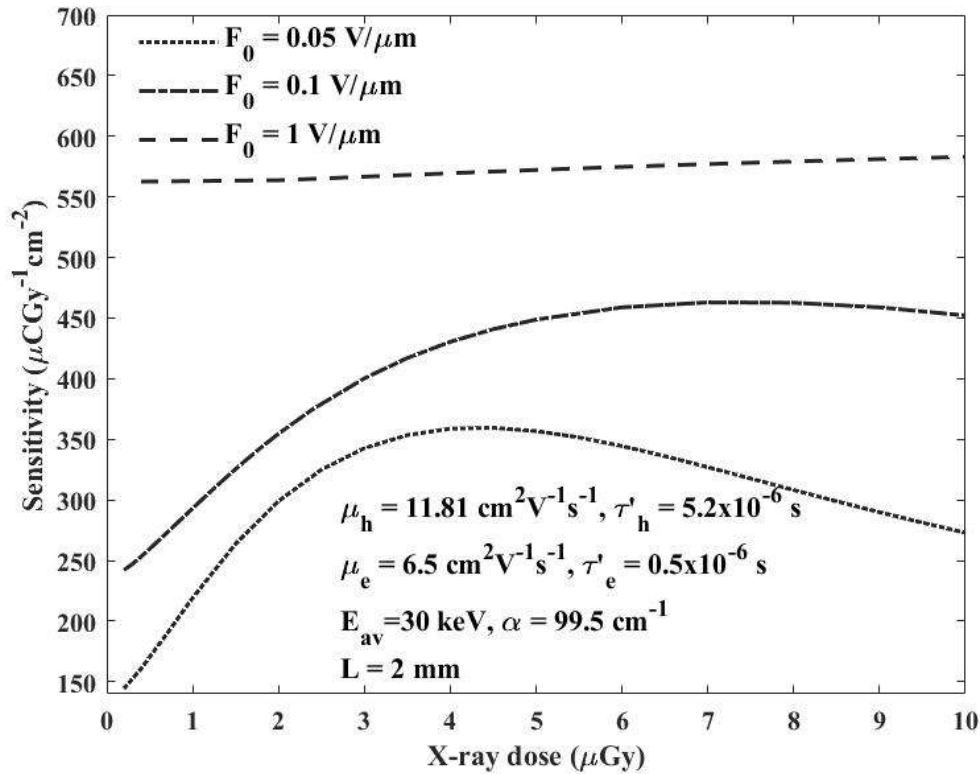


Figure 6.17: Sensitivity as a function of X-ray doses for different applied electric fields.

6.7 $\text{Cs}_2\text{AgBiBr}_6$ in Medical Diagnostics

The stabilized a-Se based X-ray detectors have been commercialized for mammography. Although they can provide excellent images, to obtain an image of a reasonably high quality from an a-Se based flat panel X-ray imager, a large applied electric field (5-10 $\text{V}/\mu\text{m}^{-1}$) must be used. However, this results in a high dark current. The sensitivity of $\text{Cs}_2\text{AgBiBr}_6$ has been compared with the commercialized a-Se detector for mammography (20 keV) and chest radiography (60 keV).

The X-ray sensitivities of an annealed sample of $\text{Cs}_2\text{AgBiBr}_6$ photoconductor and a-Se

as a function of applied electric field for chest radiographic application ($E=60$ keV) are presented in Figure 6.18. The X-ray dosage rate has been $300 \mu\text{R}$ [Table 1.1] for 1 ms for both detectors. The linear attenuation coefficient of 23.8 cm^{-1} and 11 cm^{-1} have been considered for $\text{Cs}_2\text{AgBiBr}_6$ and a-Se, respectively for average X-radiation energy of 60 keV [118]. The attenuation depth for a-Se is ~ 0.9 mm. A 1 mm thick detector is considered for both $\text{Cs}_2\text{AgBiBr}_6$ and a-Se [21]. The charge transport properties considered before for $\text{Cs}_2\text{AgBiBr}_6$ have been used. The mobility of holes and electrons for a-Se have been assumed $0.14 \text{ cm}^{-2}\text{V}^{-1}\text{s}^{-1}$ and $0.007 \text{ cm}^{-2}\text{V}^{-1}\text{s}^{-1}$, respectively [24]. The lifetimes of holes and electrons for a-Se have been adopted $50 \mu\text{s}$ and $200 \mu\text{s}$, respectively [22]. The sensitivity obtained for $\text{Cs}_2\text{AgBiBr}_6$ is much higher than a-Se due to its larger charge transport properties and greater absorption coefficient. Sensitivity reaches the value of $2677 \mu\text{CGy}^{-1}\text{cm}^{-2}$ for $\text{Cs}_2\text{AgBiBr}_6$ at electric field of $5 \text{ V}/\mu\text{m}$. The sensitivity reaches $2026 \mu\text{CGy}^{-1}\text{cm}^{-2}$ for applied electric field $5 \text{ V}/\mu\text{m}$ for a-Se. The increase in sensitivity is 32 % for $\text{Cs}_2\text{AgBiBr}_6$ compared to a-Se. This happens due to the lower mobility lifetime product of a-Se.

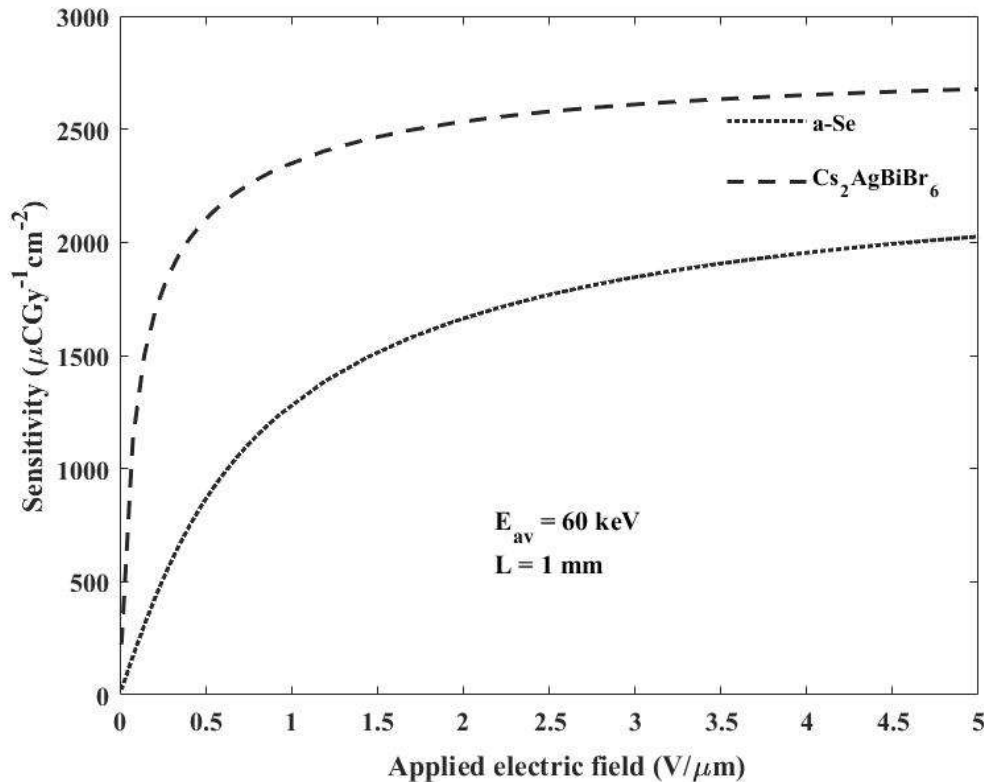


Figure 6.18: Sensitivity as a function of applied electric field for a-Se and $\text{Cs}_2\text{AgBiBr}_6$ detectors for chest radiographic applications ($E=60$ keV).

The X-ray sensitivities of an annealed sample of $\text{Cs}_2\text{AgBiBr}_6$ photoconductor and amorphous-Selenium (a-Se) as a function of applied electric field for mammographic application

($E=20$ keV) are presented in Figure 6.19. The X-ray dosage rate has been 12 mR [Table 1.1] for 1 ms for both detectors. The linear attenuation coefficient of 248 cm^{-1} and 230 cm^{-1} have been considered for $\text{Cs}_2\text{AgBiBr}_6$ and a-Se, respectively for average X-ray energy of 20 keV. Attenuation depth is $\sim 40\ \mu\text{m}$. The photoconductor thickness has been considered $200\ \mu\text{m}$ for mammography [131]. The charge transport properties considered before for $\text{Cs}_2\text{AgBiBr}_6$ and a-Se have been adopted here. The applied electric field has been varied up to $5\text{ V}/\mu\text{m}$. The sensitivity saturation of $189\ \mu\text{CGy}^{-1}\text{cm}^{-2}$ for $\text{Cs}_2\text{AgBiBr}_6$ has been achieved at $\sim 4\text{ V}/\mu\text{m}$ due to the high linear attenuation coefficient. The sensitivity for a-Se reaches $179\ \mu\text{CGy}^{-1}\text{cm}^{-2}$ at $\sim 5\text{ V}/\mu\text{m}$. The increase in sensitivity is 5.58% for $\text{Cs}_2\text{AgBiBr}_6$ from a-Se.

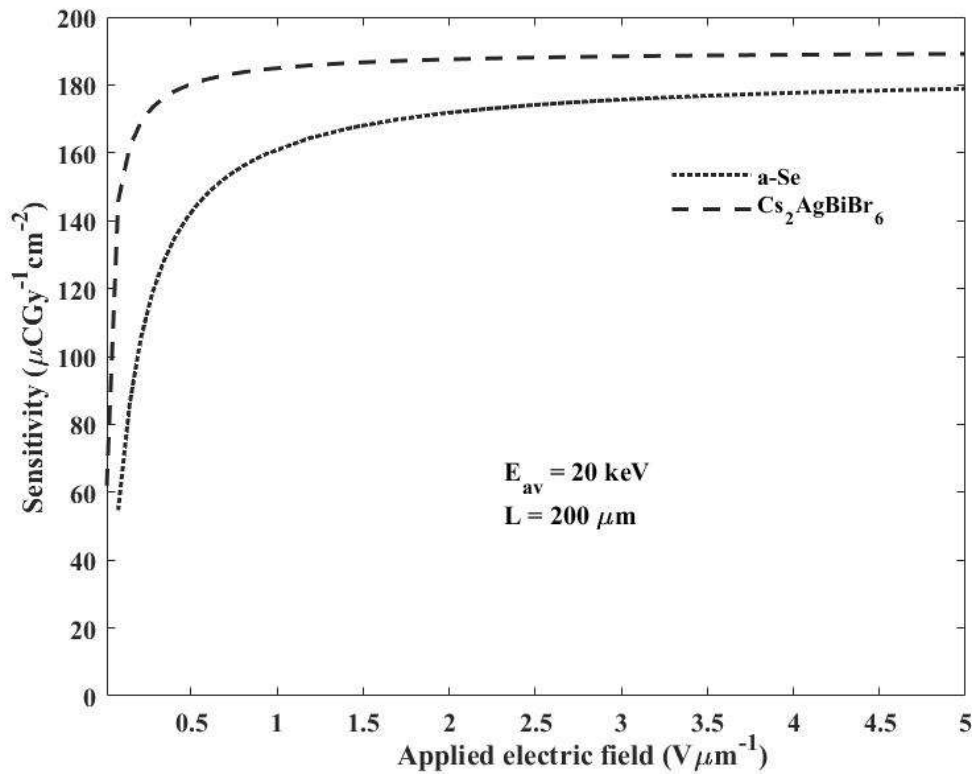


Figure 6.19: Sensitivity as a function of applied electric field for a-Se and $\text{Cs}_2\text{AgBiBr}_6$ detectors for mammographic applications($E=20$ keV).

6.8 Summary

In this chapter, the numerical model is used to evaluate the performance of a $\text{Cs}_2\text{AgBiBr}_6$ based detector. Charge diffusion and recombination effect are visible at the low applied electric field, which becomes insignificant at the higher applied electric field. The space

charge perturbs the electric field and hence affects sensitivity. Since $\text{Cs}_2\text{AgBiBr}_6$ is an inherently p-type photoconductor and radiation receiving electrode is positively biased, the hole lifetime mainly affects sensitivity compared to electron lifetime. The numerical model is used to determine the optimum thickness for a $\text{Cs}_2\text{AgBiBr}_6$ based X-ray detector for different applied electric fields. The detector thickness of $\sim 350\text{-}550 \mu\text{m}$ is suitable to achieve maximum sensitivity. We have discovered that sensitivity changes with X-ray doses, which is significant at a very low electric field. The performance of $\text{Cs}_2\text{AgBiBr}_6$ in chest radiography and mammography is investigated, which shows sensitivity for $\text{Cs}_2\text{AgBiBr}_6$ detectors is better than commercially available a-Se detectors. Moreover, the maximum sensitivity for the $\text{Cs}_2\text{AgBiBr}_6$ detector can be obtained at a lower electric field than the a-Se detector. The analysis outcomes utilizing the numerical model for $\text{Au/Cs}_2\text{AgBiBr}_6/\text{Au}$ are shown in Table 6.1.

Table 6.1: Optimized parameters for $\text{Au/Cs}_2\text{AgBiBr}_6/\text{Au}$ X-ray detector

X-ray energy E_{ph} (keV)	Thickness L (μm)	Dose X (μGy)	Applied electric field F_0 ($\text{V}/\mu\text{m}$)	Maximum sensitivity S_{max} ($\mu\text{C}/\text{Gycm}^2$)
30	350-550	0.2	0.1-1	453-622.7
30	2000	4.5-7	0.05-1	359.5-580
20	200	0.105	4	189
60	1000	0.0026	5	2677

Chapter 7

Conclusions and Future Works

7.1 Conclusion

A numerical model of the X-ray sensitivity based on the semiconductor continuity equations, trapping rate equations, and Poisson's equation has been developed and is applied to a $\text{Cs}_2\text{AgBiBr}_6$ double perovskite direct-conversion X-ray image detector. Different recombination process is included in the numerical model. The model considers the perturbation of the applied electric field due to the carrier trapping in the bulk and accumulation of ions near the metal/photoconductor interfaces under the influence of bias voltage. The analytical model for photocurrent is used to obtain charge transport properties of $\text{Cs}_2\text{AgBiBr}_6$ photoconductor. Sources of the dark current in the $\text{Cs}_2\text{AgBiBr}_6$ detector are analyzed. The sensitivity has been analyzed under different operating conditions (i.e applied electric field, X-ray dose, etc) of a $\text{Cs}_2\text{AgBiBr}_6$ based X-ray detector.

Our analysis indicates that there is a photocurrent gain for the $\text{Cs}_2\text{AgBiBr}_6$ detector due to the presence of dark currents originating mainly from hole injection. The electric field elevation at the metal/photoconductor interface caused by the presence of accumulated ions is responsible for enhanced carrier injection from the electrodes. The hole injection current is $\sim 2.7 \text{ nAcm}^{-2}$ at an applied field of $0.0025 \text{ V}/\mu\text{m}$ with dose rate $\sim 140 \mu\text{Gys}^{-1}$ which is larger than the preferable range of 1 nAcm^{-2} in medical diagnostics. We have also observed that the effective barrier height for charge injection decreases with the increase of exposure. The bulk thermal generation current is $\sim 4\text{-}5$ orders of magnitude less than the charge injection current. The charge distribution obtained from the numerical model shows the photoconductor/top electrode interface has the highest steady-state drift electron concentration, while the hole has the highest concentration further from the top electrode. Since holes are more mobile and have longer

lifetimes than electrons, they move more quickly and are less likely to get trapped. The distribution of trapped holes is essentially constant along the detector thickness. Electron mobility and trapping time are both lower than those of holes. As a result, slower electrons get trapped easily. Hence, the trapped electron distribution exhibits an exponential interaction profile. The trapped charge concentration decreases and the drift charge concentration increases with the increase of the applied electric field. According to our findings, because the injected charges increase the total collected charges, the sensitivity is 2% higher when charge carrier injection is considered. However, for high exposure and very low electric field, the sensitivity is slightly lower when the charge carrier injection is considered. We have also observed that the effect of charge carrier diffusion is negligible. We found that the recombination between free charge carriers and the recombination between free charge carriers and trapped charge carriers is insignificant. We understood from our analysis that the level of hole trapping has a substantial impact on sensitivity compared to electron trapping. This is due to the fact that the X-ray detector is positively biased and the hole drifts across the photoconductor thickness before collection at the bottom electrode. We have observed that the thickness of $\text{Cs}_2\text{AgBiBr}_6$ for which maximum sensitivity occurs increases with the applied electric field. The optimum photoconductor thickness is $\sim 350\text{-}550 \mu\text{m}$ for 30 keV X-ray energy. From the sensitivity vs detector thickness analysis, we found that at higher electric field sensitivity does not change significantly with the electric field which is due to the limited quantum efficiency of the detector. Since $\text{Cs}_2\text{AgBiBr}_6$ have better charge transport properties and attenuation coefficient compared to a-Se, the sensitivity for chest radiology is 32% and for mammography is 5.58 %, higher for CABB compared to a-Se at $5 \text{ V}/\mu\text{m}$ for similar device thickness. Similar sensitivity can be obtained by applying a lower field in $\text{Cs}_2\text{AgBiBr}_6$ compared to a-Se.

This work will help improve the current technical challenges of $\text{Cs}_2\text{AgBiBr}_6$ based X-ray detectors and evaluate their potential for future X-ray detection applications. The sensitivity analysis for $\text{Cs}_2\text{AgBiBr}_6$ using the numerical model shows that it has a lot of room for development. By controlling the fabrication process of the $\text{Cs}_2\text{AgBiBr}_6$ device, the defect concentration, resistivity, and mobility-lifetime product can be improved to achieve sensitivity comparable to its hybrid lead halide perovskite counterparts which will lead to stable, highly efficient, and nontoxic lead-free X-ray detector.

7.2 Suggestions for Future Works

In many areas, including astrophysics, medical imaging, industrial monitoring, and fundamental scientific research, high-performance radiation detectors are highly desired. The detecting material, which serves as the foundation of detection systems, is crucial in deciding how well the detector will perform. To further optimize the potential $\text{Cs}_2\text{AgBiBr}_6$ detectors and improve their performance following works can be done in the future:

- i) During fabrication, $\text{Cs}_2\text{AgBiBr}_6$ is susceptible to defect formation that causes field-driven ion migration in the detector. The accumulation of ions near the electrode interfaces and the existence of trapped charges at the beginning of the device operation, generate a non-uniform electric field with an elevation near the metal/photoconductor interfaces. The high electric field near the interfaces affects the contact carrier injection. The injection current can be reduced by implementing a blocking layer between the electrode and the photoconductor. The inclusion of the blocking layer in the numerical model will help investigate the future optimization of the device.
- ii) The subsequent exposures to the detector generate deep trap centers in the device. The inclusion of the X-ray-induced deep trap centers in the numerical model will help improve the performance of the $\text{Cs}_2\text{AgBiBr}_6$ based detectors in the future.
- iii) A thorough assessment of image quality may be accomplished by investigating the MTF (Modulation Transfer Function) and DQE (Detective Quantum Efficiency) along with the sensitivity of lead-free perovskite photoconductors.
- iv) The numerical model is based on a p-type photoconductor, it can be extended to analyze the properties and performance of an n-type photoconductor.

Appendix A

Terms Related to Radiation Detection

Exposure: Exposure signifies how much ionization is caused by radiation when passing through the air. The SI unit of exposure is coulomb/kilogram (C/kg). The most common exposure unit is roentgen (R), named after the inventor of X-rays. 1 R is the amount of radiation needed to produce a charge of 2.58×10^{-4} in 1 kg of dry air.

Dose: Dose refers to the amount of radiation absorbed by a material. The SI unit is gray (Gy) or J/kg. 1 Gy is the amount of radiation when 1 J of energy is absorbed per kg of the material. $1 \text{ Gy}_{air} = 114 \text{ R}$, where 1 Gy_{air} is the radiation required by per kg of dry air to absorb 1 J of energy.

Charge collection efficiency (CCE): Charge collection efficiency is the ratio of the electrical charge collected (Q) at the electrodes to the generated electrical charge (Q_0) in the detector due to the incidence of radiation.

Absorption depth (δ): The absorption depth signifies how deeply incident radiation penetrates into a semiconductor before being absorbed. The inverse of the absorption coefficient, α is the absorption depth.

Spatial resolution: Spatial resolution is an important performance parameter of an image detector. It can be defined as the ability of the detector to separate two points and is quantified as the smallest separation of two points that can be distinguished from each other.

Noise: noise is an error or undesired random disturbance of a useful information signal

Detection limit: The detection limit, which determines the lowest detectable dose, is a crucial X-ray detector parameter. The detection limit is defined by the International Union of Pure and Applied Chemistry (IUPAC) as the equivalent dosage rate to produce a signal bigger than three times the noise level.

Contrast: Radiographic contrast is the signal or intensity differential between the structure of interest and its surroundings. Contrast is produced by the varied ways that different tissues attenuate X-rays.

Dynamic range: The maximum signal variation across which the detector output accurately depicts the photon fluence, is referred to as the dynamic range of an imaging system. A wide dynamic range is required to obtain a high-quality image.

Appendix B

X-ray Photon Fluence

Assuming an X-ray beam of ψ energy fluence and X exposure incident on a photoconductive material unit area, then the energy absorbed by the material from the X-ray beam would be

$$\psi \left(\frac{\alpha_{air}}{\rho_{air}} \right) = 0.00876 \times 10^{-3} X J/g \quad (B.1)$$

$$\psi = \frac{0.00876 X 10^{-3} X}{(\alpha_{air}/\rho_{air})} J/gm = \frac{5.45 \times 10^{13} X}{(\alpha_{air}/\rho_{air})} eV/cm^2 \quad (B.2)$$

where α_{air}/ρ_{air} is in cm^2/gm . Therefore, the X-ray photon fluence ϕ_0 is given by

$$\phi_0 = \frac{5.45 \times 10^{13} X}{(\alpha_{air}/\rho_{air}) E} photons/cm^2 \quad (B.3)$$

The X-ray photon fluence per unit exposure versus X-ray photon energy is shown in Figure B.1. The X-ray fluence per unit exposure is energy dependent because the mass energy absorption coefficient (α_{air}/ρ_{air}) for air is energy dependent.

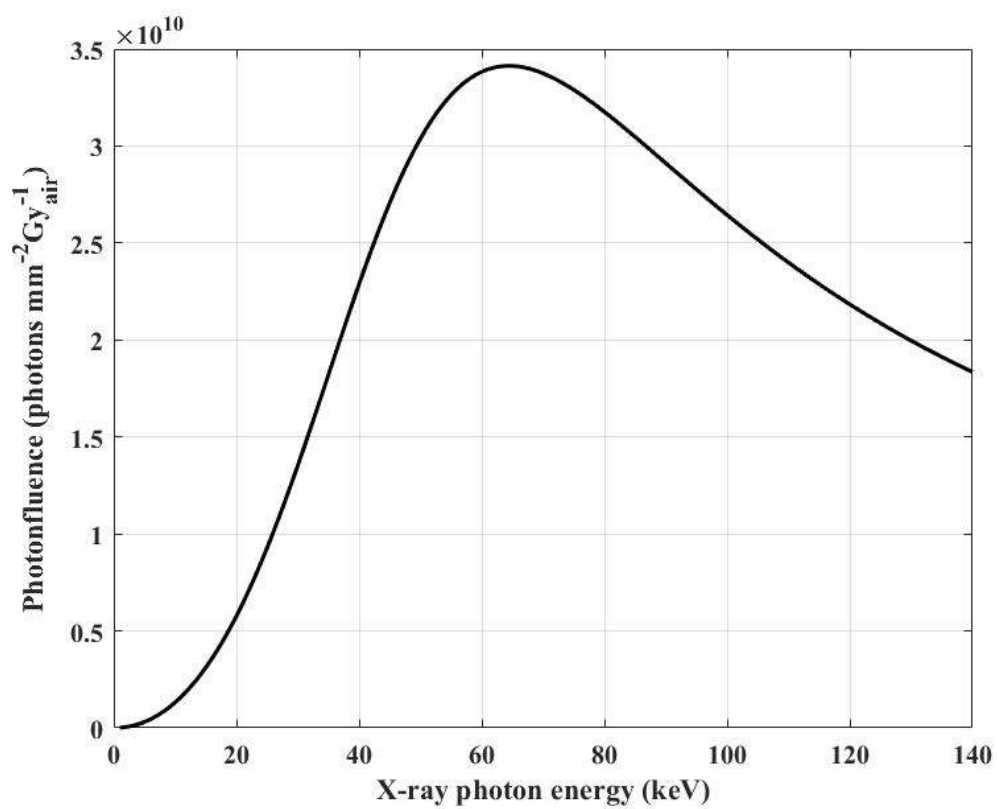


Figure B.1: The X-ray photon fluence (photons/ mm^2) per unit X-ray exposure (Gy_{air}) versus X-ray photon energy for diagnostic X-ray imaging.

Appendix C

Finite Difference Method

The Finite Difference Method (FDM) is one of the most popular numerical techniques to solve partial differential equations. In FDM, derivatives in differential equations are substituted by finite differences. These algebraic equations are then solved to find approximate solutions.

In this work, we need to solve equations (5.14) to (5.18) to obtain normalized space charge (i.e. $p(t, x)$, $n(t, x)$, $p_t(t, x)$, $n_t(t, x)$), normalized field distribution ($F(t, x)$) across photoconductor thickness, and the sensitivity of the X-ray image detector. The numerical solution is approximated by MATLAB code in MATLAB R2019b version. By approximating derivatives from equations (5.14) to (5.18) by uniformly discretizing the time domain into $m+1=10001$ steps with step size $\Delta t = 1 \times 10^{-4}$ and space domain into $n+1=2401$ steps with step size $\Delta x = 4.17 \times 10^{-4}$ the equations are solved. The Grid that was used to obtain the numerical solution to the equations (5.14)-(5.18) is shown in Figure C.1 [15]. The step sizes Δt and Δx are found from,

$$\Delta t = \frac{1}{m} \quad (\text{C.1})$$

$$\Delta x = \frac{1}{n} \quad (\text{C.2})$$

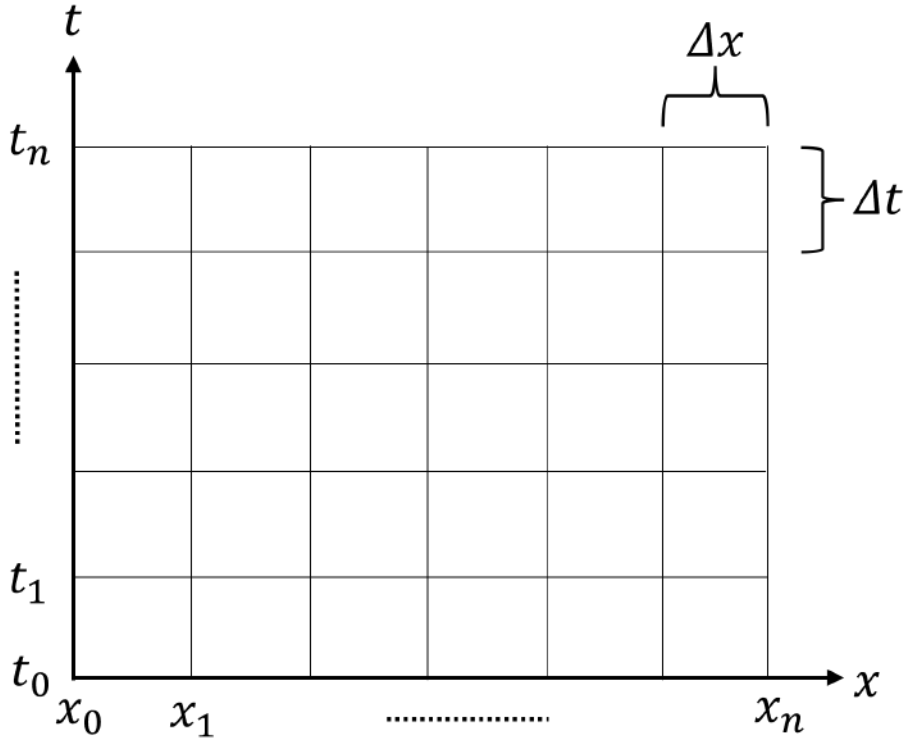


Figure C.1: Discretization of time and space domain to numerically solve normalized semiconductor equations.

Assuming t_k and x_j are the k th and j th points in the time and space domain, respectively. For simplification of the equations, t_k and x_j can be expressed as

$$t_k = k\Delta t, 0 \leq k \leq m \quad (\text{C.3})$$

$$x_j = j\Delta x, 0 \leq j \leq n \quad (\text{C.4})$$

Let's assume $p(t_k, x_j)$ i.e., normalized drift hole concentration at normalized time t_k and normalized position x_j is denoted as p_j^k . To obtain the unique solution of $p(t, x)$, the initial and boundary conditions are:

$$p(0, x) = 0, 0 < x < 1 \quad (\text{C.5})$$

$$p(t, 0) = \frac{N_v}{p_0} e^{-\frac{\phi_h - \beta_s \sqrt{F_1}}{kT}}, t > 0 \quad (\text{C.6})$$

In this thesis, solutions of partial differential equations (PDE) are obtained using the implicit backward Euler method since this method is absolutely stable [132] [133]. In the backward Euler method, the difference approximation substitution of derivatives is taken from its value from a previous time, i.e., the difference approximation is estimated

at t_{k+1} . Hence,

$$\frac{\delta p(t_{k+1}, x_j)}{\delta t} = \frac{p_j^{k+1} - p_j^k}{\Delta t} \quad (\text{C.7})$$

$$\frac{\delta p F(t_{k+1}, x_j)}{\delta x} = \frac{p_j^{k+1} F_j^{k+1} - p_{j-1}^{k+1} p_{j-1}^{k+1}}{\Delta x} \quad (\text{C.8})$$

Since t_{k+1} is used as the reference time instead of t_k , the approximation of the derivative is a backward difference. Using the backward difference of equation (C.7) and (C.8) in equation (5.15) we get,

$$\begin{aligned} \frac{p_j^{k+1} - p_j^k}{\Delta t} = & -r_\mu \frac{(p_j^{k+1} F_j^{k+1} - p_{j-1}^{k+1} F_{j-1}^{k+1})}{\Delta x} + r_{dh} \frac{p_{j+1}^k - 2p_j^k + p_{j-1}^k}{\Delta x^2} \\ & r_\mu \frac{p_j^{k+1}}{\tau_{hj}^{k+1}} - C_R p_j^{k+1} n_j^{k+1} - C_0 r_\mu p_j^{k+1} n_{tj}^{k+1} + K_j^k e^{-\frac{x_j}{\Delta}} \end{aligned} \quad (\text{C.9})$$

$$\text{Or, } A_h p_j^{k+1} = \frac{p_j^k}{\Delta t} + r_\mu \frac{p_{j-1}^{k+1} F_{j-1}^{k+1}}{\Delta x} + r_{dh} \frac{p_{j+1}^k - 2p_j^k + p_{j-1}^k}{\Delta x^2} + K_j^k e^{-\frac{x_j}{\Delta}} \quad (\text{C.10})$$

Here,

$$A_h = \frac{1}{\Delta t} + \frac{r_\mu F_j^{k+1}}{\Delta x} + \frac{r_\mu}{\tau_{hj}^{k+1}} + C_R n_j^{k+1} + r_\mu C_0 n_{tj}^{k+1} \quad (\text{C.11})$$

$$\text{Or, } A_h \approx \frac{1}{\Delta t} + \frac{r_\mu F_j^k}{\Delta x} + \frac{r_\mu}{\tau_{hj}^k} + C_R n_j^k + r_\mu C_0 n_{tj}^k \quad (\text{C.12})$$

To replace derivatives into finite differences the value of Δt has to be very small for satisfactory precision. Since, Δt is very small, $|F_j^{k+1} - F_j^k|$, $|n_j^{k+1} - n_j^k|$, $|n_{tj}^{k+1} - n_{tj}^k|$ or, $|\tau_{hj}^{k+1} - \tau_{hj}^k| \ll 1$. The value of $\Delta t = 1 \times 10^{-4}$ in all calculations in our work. Hence, the approximation in the equation (C.12) is acceptable. Using equations (C.10) and (C.12), p_j^{k+1} was calculated and the solution proceeded in space from left to right as in Figure 1.

To calculate the value of n_{n+1-j}^{k+1} , equation (5.14) is used and the necessary initial and boundary conditions are,

$$n(0, x) = 0, 0 < x < 1 \quad (\text{C.13})$$

$$n(t, 1) = \frac{N_c}{p_0} e^{-\frac{\phi_e - \beta_s \sqrt{F_2}}{kT}}, t > 0 \quad (\text{C.14})$$

n_{n+1-j}^{k+1} is calculated from the following two linear algebraic equations and the solution proceeded in space from right to left as in Figure C.1.

$$A_e n_{n+1-j}^{k+1} = \frac{n_{n+1-j}^k}{\Delta t} + \frac{n_{n+2-j}^{k+1} F_{n+2-j}^{k+1}}{\Delta x} + r_{de} \frac{n_{n-j}^k - 2n_{n+1-j}^k + n_{n+2-j}^k}{\Delta x^2} + K_j^k e^{-\frac{x_{n+1-j}}{\Delta}} \quad (\text{C.15})$$

And,

$$A_e \approx \frac{1}{\Delta t} + \frac{F_{n+1-j}^k}{\Delta x} + \frac{1}{\tau_{ej}^k} + C_R p_{n+1-j}^k + C_0 p_{t(n+1-j)}^k \quad (\text{C.16})$$

The values of p_j^{k+1} and n_j^{k+1} are used to determine p_{tj}^{k+1} and n_{tj}^{k+1} using the two equations given below and the initial conditions discussed before.

$$p_{tj}^{k+1} \left(\frac{1}{\Delta t} + C_0 n_j^{k+1} \right) = \frac{p_{tj}^k}{\Delta t} + r_\mu \frac{p_j^{k+1}}{\tau_{hj}^k} \quad (\text{C.17})$$

$$n_{tj}^{k+1} \left(\frac{1}{\Delta t} + C_0 r_\mu p_j^{k+1} \right) = \frac{n_{tj}^k}{\Delta t} + \frac{n_j^{k+1}}{\tau_{ej}^k} \quad (\text{C.18})$$

τ_{hj}^{k+1} and τ_{ej}^{k+1} are assumed time and space independent parameter.

The electric field distribution across space at different times was determined using the calculated values of p_j^{k+1} , n_j^{k+1} , p_{tj}^{k+1} and n_{tj}^{k+1} and using the equation (5.18) and the boundary condition described in equation (5.20). Thus,

$$F_0^{k+1} = 1 - \int_0^1 \left\{ \int_0^x (C_0(p - n + p_t - n_t)) dx \right\} dx \quad (\text{C.19})$$

$$F_j^{k+1} = F_0^{k+1} + \int_0^{x_j} C_0(p - n + p_t - n_t) dx, 1 \leq j \leq n \quad (\text{C.20})$$

The integral equations (C.19) and (C.20) for the electric field are numerically calculated by applying the discrete values of p_j^{k+1} , n_j^{k+1} , p_{tj}^{k+1} and n_{tj}^{k+1} . Consequently, the values of p_j^{k+1} , n_j^{k+1} , p_{tj}^{k+1} , n_{tj}^{k+1} , and F_j^{k+1} are obtained simultaneously at time t_{k+1} by numerically solving the equations (5.14) to (5.18). This same process is repeated for the next time step. The calculations are replicated for different step sizes to make sure it converges and is accurate. The space step size $\Delta x = 4.17 \times 10^{-4}$ and The time step size $\Delta t = 10^{-4}$ is sufficient for getting values with reasonable accuracy.

References

- [1] D. Attwood, *Soft X-Rays and Extreme Ultraviolet Radiation: Principles and Applications*. Cambridge University Press, 1999.
- [2] R. L. V. Metter, J. Beutel, and H. L. Kundel, Eds., *Handbook of Medical Imaging, Volume 1. Physics and Psychophysics*. SPIE Press, 2000.
- [3] C. Szeles, “CdZnTe and CdTe materials for X-ray and gamma ray radiation detector applications,” *physica status solidi (b)*, vol. 241, pp. 783 – 790, Mar 2004.
- [4] M. Kördel, A. Dehlinger, C. Seim, U. Vogt, E. Fogelqvist, J. A. Sellberg, H. Stiel, and H. M. Hertz, “Laboratory water-window X-ray microscopy,” *2009 IEEE LEOS Annual Meeting Conference Proceedings*, p. 48, 2009.
- [5] K. Iniewski, *Medical imaging: principles, detectors, and electronics*. John Wiley & Sons, 2009.
- [6] G. Zentai, “X-ray imaging for homeland security,” vol. 3, Sep 2008, pp. 1–6.
- [7] C. J. Karzmark and N. C. Pering, “Electron linear accelerators for radiation therapy: history, principles and contemporary developments,” *Physics in Medicine & Biology*, vol. 18, no. 3, p. 321, May 1973. [Online]. Available: <https://dx.doi.org/10.1088/0031-9155/18/3/001>
- [8] S. O. Kasap, M. Z. Kabir, and J. A. Rowlands, “Recent advances in X-ray photoconductors for direct conversion X-ray image detectors,” *Current Applied Physics*, vol. 6, no. 3, pp. 288–292, Jun 2006. [Online]. Available: <https://www.sciencedirect.com/science/article/pii/S1567173905002415>
- [9] M. Körner, C. H. Weber, S. Wirth, K.-J. Pfeifer, M. F. Reiser, and M. Treitl, “Advances in digital radiography: Physical principles and system overview,” *RadioGraphics*, vol. 27, no. 3, pp. 675–686, 2007. [Online]. Available: <https://doi.org/10.1148/rg.273065075>

- [10] M. J. Yaffe and J. A. Rowlands, “X-ray detectors for digital radiography,” *Physics in Medicine and Biology*, vol. 42, no. 1, pp. 1–39, Jan 1997. [Online]. Available: <https://doi.org/10.1088/0031-9155/42/1/001>
- [11] “What is digital radiography and how does it work?” <https://www.twi-global.com/technical-knowledge/faqs/digital-radiography>, accessed: 2022-04-04.
- [12] V. N. Cooper, T. Oshiro, C. H. Cagnon, L. W. Bassett, T. M. McLeod-Stockmann, and N. V. Bezrukiy, “Evaluation of detector dynamic range in the X-ray exposure domain in mammography: a comparison between film-screen and flat panel detector systems,” *Medical physics*, vol. 30, no. 10, p. 2614–2621, Oct 2003. [Online]. Available: <https://doi.org/10.1118/1.1606450>
- [13] D. C. Hunt, O. Tousignant, and J. A. Rowlands, “Evaluation of the imaging properties of an amorphous selenium-based flat panel detector for digital fluoroscopy,” *Medical physics*, vol. 31, no. 5, pp. 1166–75, 2004.
- [14] H. G. Chotas, J. T. Dobbins, and C. E. Ravin, “Principles of digital radiography with large-area, electronically readable detectors: A review of the basics,” *Radiology*, vol. 210, no. 3, pp. 595–599, 1999. [Online]. Available: <https://doi.org/10.1148/radiology.210.3.r99mr15595>
- [15] M. Z. Kabir, “Modeling of X-ray photoconductors for X-ray image detectors,” Ph.D. dissertation, Aug 2005.
- [16] L. E. Antonuk, J. M. Boudry, Y. El-Mohri, W. Huang, J. H. Siewerdsen, J. Yorkston, and R. A. Street, “Large-area flat-panel amorphous silicon imagers,” in *Proc. SPIE – Int. Soc. Opt. Eng.*, vol. 2432, 1995, pp. 216–227.
- [17] J. J. Chabbal, C. Chaussat, T. Ducourant, L. Fritsch, J. Michailos, V. Spinnler, G. Vieux, M. S. Arqués, G. Hahm, M. Hoheisel, H. Horbaschek, R. F. Schulz, and M. F. Spahn, “Amorphous silicon X-ray image sensor,” in *Proc. SPIE – Int. Soc. Opt. Eng.*, vol. 2708, 1996, pp. 499–510.
- [18] E. Samei and M. J. Flynn, “An experimental comparison of detector performance for direct and indirect digital radiography systems,” *Medical physics*, vol. 30 4, pp. 608–22, 2003.
- [19] R. S. Saunders, E. Samei, and C. Hoeschen, “Impact of resolution and noise characteristics of digital radiographic detectors on the detectability of lung nodules,” in *Med. Phys.*, vol. 31, 2004, pp. 1603–1613.

- [20] S. Abbaszadeh, C. Scott, O. Bubon, A. Reznik, and K. Karim, "Enhanced detection efficiency of direct conversion X-ray detector using polyimide as hole-blocking layer," *Scientific reports*, vol. 3, p. 3360, Nov 2013.
- [21] S. O. Kasap, J. Frey, G. Belev, O. Tousignant, H. Mani, J. Greenspan, L. Laperriere, O. Bubon, A. Reznik, G. Decrescenzo, K. Karim, and J. A. Rowlands, "Amorphous and polycrystalline photoconductors for direct conversion flat panel X-ray image sensors," *Sensors (Basel, Switzerland)*, vol. 11, pp. 5112–57, Dec 2011.
- [22] S. O. Kasap and J. A. Rowlands, "Direct-conversion flat-panel X-ray image sensors for digital radiography," *Proc. of the IEEE*, vol. 90, pp. 591 – 604, May 2002.
- [23] H. M. Thirimanne, K. D. G. I. Jayawardena, A. J. Parnell, R. M. I. Bandara, A. Karalasingam, S. Pani, J. E. Huerdler, D. G. Lidzey, S. F. Tedde, A. Nisbet, C. A. Mills, and S. R. P. Silva, "High sensitivity organic inorganic hybrid X-ray detectors with direct transduction and broadband response," *Nature Communications*, vol. 9, pp. 2926–2936, 2018.
- [24] H. Huang and S. Abbaszadeh, "Recent developments of amorphous selenium-based X-ray detectors: A review," *IEEE Sensors Journal*, vol. 20, pp. 1694–1704, 2020.
- [25] J. Park, P. Jeon, J. Kim, and S. Im, "Small-dose-sensitive X-ray image pixel with HgI₂ photoconductor and amorphous oxide thin-film transistor," *Advanced healthcare materials*, vol. 4, no. 1, pp. 51–57, Jan. 2015.
- [26] J. H. Won, K. H. Kim, J. H. Suh, S. H. Cho, P. K. Cho, J. K. Hong, and S. U. Kim, "The X-ray sensitivity of semi-insulating polycrystalline CdZnTe thick films," *Nuclear Instruments and Methods in Physics Research Section A: Accelerators, Spectrometers, Detectors and Associated Equipment*, vol. 591, no. 1, pp. 206–208, 2008. [Online]. Available: <https://www.sciencedirect.com/science/article/pii/S0168900208004385>
- [27] X. Zhu, H. Sun, D. Yang, P. Wangyang, and X. Gao, "Comparison of electrical properties of X-ray detector based on PbI₂ crystal with different bias electric field configuration," *Journal of Materials Science: Materials in Electronics*, vol. 27, no. 11, p. 11798–11803, Nov 2016.
- [28] M. Simon, R. Ford, A. Franklin, S. Grabowski, B. Menser, G. Much, A. Nascetti, M. Overdick, M. Powell, and D. Wiechert, "Analysis of lead oxide (PbO) layers

- for direct conversion X-ray detection,” *IEEE Transactions on Nuclear Science*, vol. 52, no. 5, pp. 2035–2040, 2005.
- [29] Y. Liu, H. Sun, D. Yang, P. Wangyang, X. Gao, Z. Gou, and X. Zhu, “Electrical properties of X-ray detector based on bismuth tri-iodide single crystal with electrode configuration considering,” *Materials Research Express*, vol. 6, no. 5, pp. 055 902–055 912, Feb 2019. [Online]. Available: <https://doi.org/10.1088/2053-1591/aaff87>
- [30] H. Wei and J. Huang, “Halide lead perovskites for ionizing radiation detection,” *Nature Communications*, vol. 10, pp. 1066–1078, 2019.
- [31] S. Yakunin, M. Sytnyk, D. Kriegner, S. Shrestha, M. Richter, G. J. Matt, H. Azimi, C. J. Brabec, J. Stangl, M. V. Kovalenko, and W. Heiss, “Detection of X-ray photons by solution-processed organic-inorganic perovskites.” *Nature photonics*, vol. 9, no. 7, pp. 444–449, 2015.
- [32] K. Oh, M. Yun, M. Kim, K. Jang, and S. Nam, “HgI₂ flat panel radiation detectors for medical imaging acquisition,” in *World Congress on Medical Physics and Biomedical Engineering, September 7 - 12, 2009, Munich, Germany*, O. Dössel and W. C. Schlegel, Eds., Sep 2009, pp. 590–593.
- [33] A. Jana, S. Cho, S. A. Patil, A. Meena, Y. Jo, V. G. Sree, Y. Park, H. Kim, H. Im, and R. A. Taylor, “Perovskite: Scintillators, direct detectors, and X-ray imagers,” *Materials Today*, vol. 55, pp. 110–136, 2022. [Online]. Available: <https://www.sciencedirect.com/science/article/pii/S1369702122000955>
- [34] K. Khalaph, Z. Shanan, A. Jafar, and F. Mustafa Al-attar, “Structural and optical properties of PbI₂ thin films to fabricate perovskite solar cells,” *Defect and Diffusion Forum*, vol. 398, pp. 140–146, Jan 2020.
- [35] H. Wei, Y. Fang, P. Mulligan, W. C. Chuirazzi, H. Fang, C. Wang, B. Ecker, Y. Gao, Y. Gao, M. A. Loi, L. Cao, and J. Huang, “Sensitive X-ray detectors made of methylammonium lead tribromide perovskite single crystals,” *Nature Photonics*, vol. 10, pp. 333–339, 2016.
- [36] F. Zhuge, P. Luo, and T. Zhai, “Lead-free perovskites for X-ray detecting,” *Chinese Science Bulletin*, vol. 62, pp. 1491–1493, 2017.
- [37] W. Pan, H. Wu, J. Luo, Z. Deng, C. Ge, C. Chen, X.-H. Jiang, W.-J. Yin, G. Niu, L. Zhu, L. Yin, Y. Zhou, Q. Xie, X. Ke, M. Sui, and J. Tang, “Cs₂AgBiBr₆ single-crystal X-ray detectors with a low detection limit,” *Nature Photonics*, vol. 11, pp. 726–732, 2017.

- [38] F. Heidari Gourji and D. Velauthapillai, "A review on Cs-based Pb-free double halide perovskites: From theoretical and experimental studies to doping and applications," *Molecules*, vol. 26, no. 7, 2021. [Online]. Available: <https://www.mdpi.com/1420-3049/26/7/2010>
- [39] S. M. S. Siddiquee and M. Z. Kabir, "Modeling of photocurrent and lag signals in amorphous selenium X-ray detectors," *Journal of Vacuum Science and Technology*, vol. 33, p. 041514, 2015.
- [40] S. O. Kasap, "X-ray sensitivity of photoconductors: application to stabilized a-Se," *Journal of Physics D: Applied Physics*, vol. 33, no. 21, p. 2853, Nov 2000. [Online]. Available: <https://dx.doi.org/10.1088/0022-3727/33/21/326>
- [41] A. Hoq, D. Mamsapuram Panneerselvam, and M. Kabir, "Sensitivity reduction mechanisms in organic perovskite X-ray detectors," *Journal of Materials Science: Materials in Electronics*, vol. 32, pp. 16 824–16 830, 2021.
- [42] B. Yang, W. Pan, H. Wu, G. Niu, J. Yuan, K. H. Xue, L. Yin, X. Du, X. shui Miao, X. Yang, Q. Xie, and J. Tang, "Heteroepitaxial passivation of Cs₂AgBiBr₆ wafers with suppressed ionic migration for X-ray imaging," *Nature Communications*, vol. 10, 2019.
- [43] D. Li, H. Wu, H.-C. Cheng, G. Wang, Y. Huang, and X. Duan, "Electronic and ionic transport dynamics in organolead halide perovskites," *ACS nano*, vol. 10, no. 7, pp. 6933–41, 2016.
- [44] S. A. Mahmood and M. Z. Kabir, "Dark current mechanisms in stabilized amorphous selenium based n-i detectors for X-ray imaging applications," *Journal of Vacuum Science and Technology*, vol. 29, p. 031603, 2011.
- [45] H. Zhang, Z. Gao, R. Liang, X. Zheng, X. Geng, Y. Zhao, D. Xie, J. Hong, H. Tian, Y. Yang, X. Wang, and T. ling Ren, "X-ray detector based on all-inorganic lead-free Cs₂AgBiBr₆ perovskite single crystal," *IEEE Transactions on Electron Devices*, vol. 66, pp. 2224–2229, 2019.
- [46] C. A. Kelsey, "The physics of radiology," *Medical Physics*, vol. 11, no. 5, pp. 731–732, 1984. [Online]. Available: <https://aapm.onlinelibrary.wiley.com/doi/abs/10.1118/1.595545>
- [47] C. A. Klein, "Bandgap dependence and related features of radiation ionization energies in semiconductors," *Journal of Applied Physics*, vol. 39, pp. 2029–2038, 1968.

- [48] W. Que and J. A. Rowlands, "X-ray photogeneration in amorphous selenium: Geminate versus columnar recombination," *Phys. Rev. B Condens. Matter*, vol. 51, no. 16, pp. 10 500–10 507, 1995.
- [49] M. Z. Kabir, S. M. Arnab, and N. Hijazi, "Electron–hole pair creation energy in amorphous selenium: Geminate versus columnar recombination," *Journal of Materials Science: Materials in Electronics*, vol. 30, Dec 2019.
- [50] W. Zhao and J. A. Rowlands, "Digital radiology using active matrix readout of amorphous selenium: theoretical analysis of detective quantum efficiency," *Medical physics*, vol. 24 12, pp. 1819–33, 1997.
- [51] N. Matsuura, W. Zhao, Z. Q. Huang, and J. A. Rowlands, "Digital radiology using active matrix readout: amplified pixel detector array for fluoroscopy," *Medical physics*, vol. 26, no. 5, pp. 672–81, 1999.
- [52] G. Pang, D. L. Lee, and J. A. Rowlands, "Investigation of a direct conversion flat panel imager for portal imaging," *Medical physics*, vol. 28, no. 10, pp. 2121–8, 2001.
- [53] G. Pang and J. A. Rowlands, "Development of high quantum efficiency flat panel detectors for portal imaging: intrinsic spatial resolution," *Medical physics*, vol. 29 10, pp. 2274–85, 2002.
- [54] W. Zhao, D. C. Hunt, K. Tanioka, and J. A. Rowlands, "Amorphous selenium flat panel detectors for medical applications," *Nuclear Instruments & Methods in Physics Research Section A-accelerators Spectrometers Detectors and Associated Equipment*, vol. 549, pp. 205–209, 2005.
- [55] S. O. Kasap, C. J. Haugen, M. T. A. Nesdoly, and J. A. Rowlands, "Properties of a-Se for use in flat panel X-ray image detectors," *Journal of Non-crystalline Solids*, vol. 266, pp. 1163–1167, 2000.
- [56] S. O. Kasap and J. A. Rowlands, "Review X-ray photoconductors and stabilized a-Se for direct conversion digital flat-panel X-ray image-detectors," *Journal of Materials Science: Materials in Electronics*, vol. 11, pp. 179–198, 2000.
- [57] S. O. Kasap and C. Juhasz, "Time-of-flight drift mobility measurements on chlorine-doped amorphous selenium films," *Journal of Physics D*, vol. 18, pp. 703–720, 1985.

- [58] H.-Z. Song, G. J. Adriaenssens, E. V. Emelianova, and V. I. Arkhipov, "Distribution of gap states in amorphous selenium thin films," *Physical Review B*, vol. 59, pp. 10 607–10 613, 1999.
- [59] K. Koughia, Z. A. Shakoor, S. O. Kasap, and J. M. Marshall, "Density of localized electronic states in a-Se from electron time-of-flight photocurrent measurements," *Journal of Applied Physics*, vol. 97, p. 033706, 2005.
- [60] S. O. Kasap, V. Aiyah, B. T. Polischuk, A. Bhattacharyya, and Z. Liang, "Deep-trapping kinematics of charge carriers in amorphous semiconductors: A theoretical and experimental study." *Physical review. B, Condensed matter*, vol. 43, no. 8, pp. 6691–6705, 1991.
- [61] S. O. Kasap, V. Aiyah, B. T. Polischuk, and M. A. Abkowitz, "Determination of the deep-hole capture cross-section in a-Se via xerographic and interrupted-field time-of-flight techniques," *Philosophical Magazine Letters*, vol. 62, pp. 377–382, 1990.
- [62] M. A. Abkowitz, "Density of states in a-Se from combined analysis of xerographic potentials and transient transport data," *Philosophical Magazine Letters*, vol. 58, pp. 53–57, 1988.
- [63] S. O. Kasap, J. B. Frey, G. Belev, O. Tousignant, H. Mani, L. Laperrière, A. Reznik, and J. A. Rowlands, "Amorphous selenium and its alloys from early xeroradiography to high resolution X-ray image detectors and ultrasensitive imaging tubes," *physica status solidi (b)*, vol. 246, 2009.
- [64] J. Stavro, A. H. Goldan, and W. Zhao, "Photon counting performance of amorphous selenium and its dependence on detector structure," *Journal of Medical Imaging*, vol. 5, pp. 043 502 – 043 502, 2018.
- [65] B. T. Polischuk, Z. A. Shukri, A. Legros, and H. M. Rougeot, "Selenium direct-converter structure for static and dynamic X-ray detection in medical imaging applications," in *Proc.SPIE*, vol. 3336, 1998, pp. 494–504.
- [66] K. min Oh, D. K. Kim, J. wook Shin, S. Heo, J.-S. Kim, J.-G. Park, and S. H. Nam, "Measurement of the electrical properties of a polycrystalline cadmium telluride for direct conversion flat panel X-ray detector," *Journal of Instrumentation*, vol. 9, p. 01010, 2014.
- [67] G. Zentai, L. Partain, R. Pavlyuchkova, C. Proano, G. Virshup, L. Melekhov, A. Zuck, B. Breen, O. Dagan, A. Vilensky, M. Schieber, and H. Gilboa, "Mercuric iodide and lead iodide X-ray detectors for radiographic and fluoroscopic

- medical imaging,” *Proc. of SPIE - The International Society for Optical Engineering*, vol. 5030, pp. 77–91, Jun 2003.
- [68] H. Du, L. Antonuk, Y. El-Mohri, Q. Zhao, Z. Su, J. Yamamoto, and Y. Wang, “Investigation of the signal behavior at diagnostic energies of prototype, direct detection, active matrix, flat-panel imagers incorporating polycrystalline HgI₂,” *Physics in medicine and biology*, vol. 53, pp. 1325–51, Apr 2008.
- [69] S. Kakkireni, S. Swain, K. Lynn, and J. McCloy, *Melt Growth of High-Resolution CdZnTe Detectors*, Jan 2022, pp. 265–284.
- [70] J. G. Mainprize, N. L. Ford, S. Yin, E. E. Gordon, W. J. Hamilton, T. O. Tümer, and M. J. Yaffe, “A CdZnTe slot-scanned detector for digital mammography,” *Medical Physics*, vol. 29, no. 12, pp. 2767–2781, 2002. [Online]. Available: <https://aapm.onlinelibrary.wiley.com/doi/abs/10.1118/1.1523932>
- [71] M. Z. Kabir and S. O. Kasap, “Modulation transfer function of photoconductive X-ray image detectors: effects of charge carrier trapping,” *Journal of Physics D*, vol. 36, pp. 2352–2358, 2003.
- [72] J. P. Moy, “Recent developments in X-ray imaging detectors,” *Nuclear Instruments & Methods in Physics Research Section A-accelerators Spectrometers Detectors and Associated Equipment*, vol. 442, pp. 26–37, 2000.
- [73] P. S. Whitfield, N. Herron, W. E. Guise, K. L. Page, Y. Q. Cheng, I. Milas, and M. K. Crawford, “Structures, phase transitions and tricritical behavior of the hybrid perovskite methyl ammonium lead iodide,” *Scientific Reports*, vol. 6, 2016.
- [74] T. Baikie, Y. Fang, J. M. Kadro, M. Schreyer, F. Wei, S. G. Mhaisalkar, M. Graetzel, and T. J. White, “Synthesis and crystal chemistry of the hybrid perovskite (CH₃NH₃)PbI₃ for solid-state sensitised solar cell applications,” *J. Mater. Chem. A*, vol. 1, no. 18, pp. 5628–5641, 2013. [Online]. Available: <http://dx.doi.org/10.1039/C3TA10518K>
- [75] G. Giorgi, J. ichi Fujisawa, H. Segawa, and K. Yamashita, “Small photocarrier effective masses featuring ambipolar transport in methylammonium lead iodide perovskite: A density functional analysis.” *The journal of physical chemistry letters*, vol. 4, no. 24, pp. 4213–6, 2013.
- [76] M. Hu, S. Jia, Y. Liu, J. Cui, Y. Zhang, H. Su, S. Cao, L. Mo, D. Chu, G. Zhao, K. Zhao, Z. Yang, and S. F. Liu, “Large and dense organic-inorganic hybrid

- perovskite $\text{CH}_3\text{NH}_3\text{PbI}_3$ wafer fabricated by one-step reactive direct wafer production with high X-ray sensitivity.” *ACS applied materials & interfaces*, vol. 12, no. 14, pp. 16 592–16 600, 2020.
- [77] Y. Song, L. Li, W. Bi, M. Hao, Y. Kang, A. Wang, Z. Wang, H. Li, X. Li, Y. Fang, D. Yang, and Q. Dong, “Atomistic surface passivation of $\text{CH}_3\text{NH}_3\text{PbI}_3$ perovskite single crystals for highly sensitive coplanar-structure X-ray detectors,” *Research (Wash. D.C.)*, vol. 2020, p. 5958243, Sep 2020.
- [78] E. Edri, S. Kirmayer, D. Cahen, and G. Hodes, “High open-circuit voltage solar cells based on organiceinorganic lead bromide perovskite,” *The Journal of Physical Chemistry Letters*, vol. 4, pp. 897–902, Feb 2013.
- [79] A. Poglitsch and D. Weber, “Dynamic disorder in methylammonium trihalogeno plumbates (ii) observed by millimeter-wave spectroscopy,” *Journal of Chemical Physics*, vol. 87, pp. 6373–6378, 1987.
- [80] K.-H. Wang, L.-C. Li, M. Shellaiah, and K. W. Sun, “Structural and photophysical properties of methylammonium lead tribromide (MAPbBr_3) single crystals,” *Scientific Reports*, vol. 7, no. 1, p. 13643, Oct 2017.
- [81] W. Wei, Y. Zhang, Q. Xu, H. Wei, Y. Fang, Q. Wang, Y. Deng, T. Li, A. Gruverman, L. R. Cao, and J. Huang, “Monolithic integration of hybrid perovskite single crystals with heterogeneous substrate for highly sensitive X-ray imaging,” *Nature Photonics*, vol. 11, pp. 315–321, 2017.
- [82] J. Song, F. Xiaopeng, H. Li, W. Li, T. Lu, C. Guo, H. Zhang, H. Wei, and B. Yang, “Facile strategy for facet competition management to improve performance of perovskite single crystal X-ray detectors,” *The Journal of Physical Chemistry Letters*, vol. 11, no. 9, pp. 3529–3535, Apr 2020.
- [83] G. Niu, X. Guo, and L. Wang, “Review of recent progress in chemical stability of perovskite solar cells,” *Journal of Materials Chemistry*, vol. 3, pp. 8970–8980, 2015.
- [84] B. Zhang, X. Liu, B. Xiao, A. B. Hafsia, K. Gao, Y. Xu, J. Zhou, and Y. Chen, “High performance x-ray detection based on one-dimensional inorganic halide perovskite CsPbI_3 .” *The journal of physical chemistry letters*, vol. 11, no. 2, pp. 432–437, 2020.
- [85] Y. Zhou and Y. Zhao, “Chemical stability and instability of inorganic halide perovskites,” *Energy & Environmental Science*, vol. 12, no. 5, pp. 1495–1511, 2019.

- [86] Y. Zhou, J. Chen, O. Bakr, and O. Mohammed, "Metal halide perovskites for X-ray imaging scintillators and detectors," *ACS Energy Letters*, vol. 6, pp. 739–768, Jan 2021.
- [87] M. Ezzeldien, S. Al-Qaisi, Z. A. Alrowaili, M. Alzaid, E. Maskar, A. Es-smairi, T. V. Vu, and D. P. Rai, "Electronic and optical properties of bulk and surface of CsPbBr₃ inorganic halide perovskite a first principles DFT 1/2 approach," *Scientific Reports*, vol. 11, p. 20622, 2021.
- [88] K. Persson, "Materials data on CsPbBr₃ (SG:221) by materials project," <https://materialsproject.org/docs/calculations>, Jul 2014.
- [89] R. Dos Reis, H. Yang, C. Ophus, P. Ercius, G. Bizarri, D. Perrodin, T. Shalapska, E. Bourret, J. Ciston, and U. Dahmen, "Determination of the structural phase and octahedral rotation angle in halide perovskites," *Applied Physics Letters*, vol. 112, p. 071901, Feb 2018.
- [90] Y. He, L. Matei, H. J. Jung, K. McCall, M. Chen, C. Stoumpos, Z. Liu, J. Peters, D.-Y. Chung, B. Wessels, M. Wasielewski, V. Dravid, A. Burger, and M. Kanatzidis, "High spectral resolution of gamma-rays at room temperature by perovskite CsPbBr₃ single crystals," *Nature Communications*, vol. 9, p. 1609, Apr 2018.
- [91] U.-G. Jong, C.-J. Yu, Y.-H. Kye, Y.-S. Kim, C.-H. Kim, and S.-G. Ri, "A first-principles study on the chemical stability of inorganic perovskite solid solutions Cs_{1-x}Rb_xPbI₃ at finite temperature and pressure," *Journal of Materials Chemistry*, vol. 6, pp. 17 994–18 002, 2018.
- [92] M. Ahmad, G. Rehman, L. Ali, M. Shafiq, R. Iqbal, R. Ahmad, T. Khan, S. Jalali-Asadabadi, M. Maqbool, and I. Ahmad, "Structural, electronic and optical properties of CsPbX₃ (X=Cl, Br, I) for energy storage and hybrid solar cell applications," *Journal of Alloys and Compounds*, vol. 705, pp. 828–839, 2017.
- [93] X. Zhang, Z. Jin, J. Zhang, D. Bai, H. Bian, K. Wang, J. Sun, Q. Wang, and S. F. Liu, "All-ambient processed binary CsPbBr₃-CsPb₂Br₅ perovskites with synergistic enhancement for high-efficiency Cs-Pb-Br-based solar cells." *ACS applied materials & interfaces*, vol. 10, no. 8, pp. 7145–7154, 2018.
- [94] G. Nedelcu, L. Protesescu, S. Yakunin, M. I. Bodnarchuk, M. J. Grotevent, and M. V. Kovalenko, "Fast anion-exchange in highly luminescent nanocrystals of cesium lead halide perovskites (CsPbX₃, X = Cl, Br, I)," *Nano Letters*, vol. 15, pp. 5635–5640, 2015.

- [95] W. Pan, B. Yang, G. Niu, K. H. Xue, X. Du, L. Yin, M. Zhang, H. Wu, X. shui Miao, and J. Tang, "Hot-pressed CsPbBr₃ quasi-monocrystalline film for sensitive direct X-ray detection," *Advanced Materials*, vol. 31, no. 44, p. 1904405, 2019.
- [96] G. J. Matt, I. Levchuk, J. Knüttel, J. Dallmann, A. Osvet, M. Sytnyk, X. Tang, J. Elia, R. Hock, W. Heiss, and C. J. Brabec, "Sensitive direct converting X-ray detectors utilizing crystalline CsPbBr₃ perovskite films fabricated via scalable melt processing," *Advanced Materials Interfaces*, vol. 7, no. 4, p. 1901575, 2020.
- [97] L. Duan, H. Zhang, M. Liu, M. Grätzel, and J. Luo, "Phase-pure γ -CsPbI₃ for efficient inorganic perovskite solar cells," *ACS Energy Letters*, vol. 7, no. 9, p. 2911–2918, 2022.
- [98] G. Murtaza and I. Ahmad, "First principle study of the structural and optoelectronic properties of cubic perovskites CsPbM₃ (m = Cl, Br, I)," *Physica B, Condensed Matter*, vol. 406, pp. 3222–3229, 2011.
- [99] B. Zhang, X. Liu, B. Xiao, A. Hafsia, K. Gao, Y. Xu, J. Zhou, and Y. Chen, "High performance X-ray detection based on one-dimensional inorganic halide perovskite CsPbI₃," *The Journal of Physical Chemistry Letters*, vol. 11, no. 2, pp. 432–437, Dec 2019.
- [100] G. Yuan, S. Qin, X. Wu, H. Ding, and A. Lu, "Pressure-induced phase transformation of CsPbI₃ by X-ray diffraction and raman spectroscopy," *Phase Transitions*, vol. 91, pp. 1–10, Aug 2017.
- [101] "European union. directive 2011/65/eu of the european parliament and of the council on the restriction of the use of certain hazardous substances in electrical and electronic equipment," *Off. J. Eur. Union*, vol. 54, p. 88–110, 2002.
- [102] Q. Sun and W.-J. Yin, "Thermodynamic stability trend of cubic perovskites." *Journal of the American Chemical Society*, vol. 139, no. 42, pp. 14 905–14 908, 2017.
- [103] M. Shi, G. Li, W. Tian, S. Jin, X. Tao, Y. Jiang, E. A. Pidko, R. Li, and C. Li, "Understanding the effect of crystalline structural transformation for lead-free inorganic halide perovskites," *Advanced Materials*, vol. 32, p. 2002137, 2020.
- [104] L. Yin, H. Wu, W. Pan, B. Yang, P. Li, J. Luo, G. Niu, and J. Tang, "Controlled cooling for synthesis of Cs₂AgBiBr₆ single crystals and its application for x-ray detection," *Advanced Optical Materials*, vol. 7, p. 1900491, 2019.

- [105] E. T. McClure, M. R. Ball, W. Windl, and P. M. Woodward, "Cs₂AgBiX₆ (X=Br, Cl): New visible light absorbing, lead-free halide perovskite semiconductors," *Chemistry of Materials*, vol. 28, p. 1354, 2016.
- [106] S. Vasala and M. Karppinen, "A₂B'B''O₆ perovskites: A review," *Progress in Solid State Chemistry*, vol. 43, pp. 1–36, 2015.
- [107] A. H. Slavney, T. Hu, A. M. Lindenberg, and H. I. Karunadasa, "A bismuth-halide double perovskite with long carrier recombination lifetime for photovoltaic applications," *Journal of the American Chemical Society*, vol. 138, no. 7, pp. 2138–41, 2016.
- [108] V. Murgulov, C. Schweinle, M. Daub, H. Hillebrecht, M. Fiederle, V. Dedic, and J. Franc, "Double perovskite Cs₂AgBiBr₆ radiation sensor: synthesis and characterization of single crystals," *Journal of Materials Science*, vol. 57, pp. 2758 – 2774, 2022.
- [109] Z. Xiao, W. Meng, J. Wang, D. B. Mitzi, and Y. Yan, "Searching for promising new perovskite-based photovoltaic absorbers: the importance of electronic dimensionality," *Materials horizons*, vol. 4, pp. 206–216, 2017.
- [110] E. M. Hutter, M. C. Gélvez-Rueda, D. Bartesaghi, F. C. Grozema, and T. J. Savenije, "Band-like charge transport in Cs₂AgBiBr₆ and mixed antimony–bismuth Cs₂AgBi_{1-x}Sb_xBr₆ halide double perovskites," *ACS Omega*, vol. 3, pp. 11 655 – 11 662, 2018.
- [111] L. R. V. Buizza and L. M. Herz, "Polarons and charge localization in metal-halide semiconductors for photovoltaic and light-emitting devices," *Advanced Materials*, vol. 33, p. 2007057, 2021.
- [112] A. D. Wright, L. R. V. Buizza, K. J. Savill, G. Longo, H. J. Snaith, M. B. Johnston, and L. M. Herz, "Ultrafast excited-state localization in Cs₂AgBiBr₆ double perovskite," *The Journal of Physical Chemistry Letters*, vol. 12, pp. 3352 – 3360, 2021.
- [113] H. Lei, D. Hardy, and F. Gao, "Lead-free double perovskite Cs₂AgBiBr₆: Fundamentals, applications, and perspectives," *Advanced Functional Materials*, vol. 31, 2021.
- [114] T. Bellakhdar, Z. Nabi, B. Bouabdallah, B. Boucif, and H. Saci, "Ab initio study of structural, electronic, mechanical and optical properties of the tetragonal Cs₂AgBiBr₆ halide double perovskite," *Applied Physics A*, vol. 128, 01 2022.

- [115] Z. Xiao, W. Meng, J. Wang, and Y. Yan, “Thermodynamic stability and defect chemistry of bismuth-based lead-free double perovskites,” *ChemSusChem*, vol. 9, p. 2628–2633, 08 2016.
- [116] M. Abdi-Jalebi, Z. Andaji-Garmaroudi, S. Cacovich, C. Stavrakas, B. Philippe, J. M. Richter, M. Alsari, E. P. Booker, E. M. Hutter, A. J. Pearson, S. Lilliu, T. J. Savenije, H. Rensmo, G. Divitini, C. Ducati, R. H. Friend, and S. D. Stranks, “Maximizing and stabilizing luminescence from halide perovskites with potassium passivation,” *Nature*, vol. 555, pp. 497–501, 2018.
- [117] S. Meloni, T. Moehl, W. R. Tress, M. Franckevius, M. Saliba, Y. H. Lee, P. Gao, M. K. Nazeeruddin, S. M. Zakeeruddin, U. Rothlisberger, and M. Graetzel, “Ionic polarization-induced current–voltage hysteresis in $\text{CH}_3\text{NH}_3\text{PbX}_3$ perovskite solar cells,” *Nature Communications*, vol. 7, p. 10334, 2016.
- [118] “X-ray mass attenuation coefficients,” <https://www.nist.gov/pml/x-ray-mass-attenuation-coefficients>, accessed: 04-02-2022.
- [119] S. Tokuda, H. Kishihara, S. Adachi, and T. Sato, “Preparation and characterization of polycrystalline CdZnTe films for large-area, high-sensitivity X-ray detectors,” *Journal of Materials Science Materials in Electronics*, vol. 15, pp. 1–8, Jan 2004.
- [120] P. De Antonis, E. Morton, and T. Menezes, “Measuring the bulk resistivity of CdZnTe single crystal detectors using a contactless alternating electric field method,” *Nuclear Instruments and Methods in Physics Research Section A: Accelerators, Spectrometers, Detectors and Associated Equipment*, vol. 380, no. 1, pp. 157–159, 1996, proceedings of the 9th International Workshop on Room Temperature Semiconductor X- and gamma-Ray Detectors, Associated Electronics and Applications. [Online]. Available: <https://www.sciencedirect.com/science/article/pii/S016890029600335X>
- [121] D. Mamsapuram Panneerselvam and M. Kabir, “Evaluation of organic perovskite photoconductors for direct conversion X-ray imaging detectors,” *Journal of Materials Science: Materials in Electronics*, vol. 28, p. 7083, May 2017.
- [122] M. S. Ghasemi, L. Zhang, J. Yun, M. Hao, D. He, P. Chen, Y. Bai, T. Lin, M. Xiao, A. Du, M. Lyu, and L. Wang, “Dual-ion-diffusion induced degradation in lead-free $\text{Cs}_2\text{AgBiBr}_6$ double perovskite solar cells,” *Advanced Functional Materials*, vol. 30, no. 42, p. 2002342, Oct 2020.

- [123] H. Zhang, X. Fu, Y. Tang, H. Wang, C. Zhang, W. Yu, X. Wang, Y. Zhang, and M. Xiao, "Phase segregation due to ion migration in all-inorganic mixed-halide perovskite nanocrystals," *Nature Communications*, vol. 10, p. 1088, Mar 2019.
- [124] Y. Dang, G. Tong, W. Song, Z. Liu, L. Qiu, L. Ono, and Y. Qi, "Interface engineering strategies towards $\text{Cs}_2\text{AgBiBr}_6$ single-crystalline photodetectors with good ohmic contact behaviors," *Journal of Materials Chemistry C*, vol. 8, pp. 276–284, 2020.
- [125] Z. Zhang, G. Yang, C. Zhou, C.-C. Chung, and I. Hany, "Optical and electrical properties of all-inorganic $\text{Cs}_2\text{AgBiBr}_6$ double perovskite single crystals," *RSC Adv.*, vol. 9, pp. 23 459–23 464, 2019. [Online]. Available: <http://dx.doi.org/10.1039/C9RA04045E>
- [126] S. A. Mahmood, "Sensitivity of X-ray image detectors: Space charge effects," *Journal of Applied Physics*, vol. 125, no. 21, p. 214505, Jun 2019.
- [127] J. Kress, C. Quarti, Q. An, S. Bitton, N. Tessler, D. Beljonne, and Y. Vaynzof, "Persistent ion accumulation at interfaces improves the performance of perovskite solar cells," *ACS Energy Letters*, vol. 7, pp. 3302–3310, Sep 2022.
- [128] J. Carr and M. Elshobaki, "Deep defects and the attempt to escape frequency in organic photovoltaic materials," *Applied Physics Letters*, vol. 107, no. 20, p. 203302, Nov 2015.
- [129] S. O. Kasap and C. Haugen, "Langevin recombination of drifting electrons and holes in stabilized a-Se (Cl-doped a-Se: 0.3% As)," *Philosophical Magazine B*, vol. 71, no. 1, pp. 91–96, 1995.
- [130] S. O. Kasap, B. Fogal, M. Kabir, R. Johanson, and S. O'Leary, "Recombination of drifting holes with trapped electrons in stabilized a-Se photoconductors: Langevin recombination," *Applied Physics Letters*, vol. 84, pp. 1991–1993, 03 2004.
- [131] Y.-H. Hu and W. Zhao, "The effect of amorphous selenium detector thickness on dual-energy digital breast imaging," *Medical Physics*, vol. 41, no. 11, p. 111904, 2014. [Online]. Available: <https://aapm.onlinelibrary.wiley.com/doi/abs/10.1118/1.4897244>
- [132] H. A. Schilling and S. L. Harris, *Applied numerical methods for engineers using MATLAB*. Brooks/Cole Publishing Co., 2000, ch.9.

- [133] G. Strang and H. Saunders, *Introduction to applied mathematics*. Wellesley-Cambridge Press, 1986, ch.6.